2012

Microstructual and Thermal Analysis of Aluminum-Silicon and Magnesium-Aluminum Alloys Subjected to High Cooling Rates

Paul Marchwica
University of Windsor

Microstructual and Thermal Analysis of AlSi and MgAl Alloys Subjected to High Cooling Rates

By
Paul C. Marchwica

A Thesis
Submitted to the Faculty of Graduate Studies
through the Department of Mechanical, Automotive and
Materials Engineering in Partial Fulfillment of the
Requirements for the Degree of Master of Applied Science at the
University of Windsor

Windsor, Ontario, Canada
2012

Microstructual and Thermal Analysis of AlSi and MgAl Alloys
Subjected to High Cooling Rates

By

Paul C. Marchwica

APPROVED BY:

Dr. R. J. Urbanic, Outside Program Reader
Industrial and Manufacturing Systems

Dr. W. Altenhof, Program Reader
Mechanical, Automotive and Materials Engineering

Dr. A. Sobiesiak, Co-Advisor
Mechanical, Automotive and Materials Engineering

Dr. J. H. Sokolowski, Co-Advisor
Mechanical, Automotive and Materials Engineering

Dr. B. Zhou, Chair of Defence
Mechanical, Automotive and Materials Engineering

11 May 2012

Declaration of Co-Authorship / Previous Publications

I. Co-Authorship Declaration

I hereby declare that this thesis incorporates material that is a result of joint research as follows: This thesis also incorporates outcomes of research performed in the field of fraction solid modeling under the supervision of Dr. J.H. Sokolowski with the co-authorship of several other parties. Contribution of the co-authors is primarily through the provision of calculations for enthalpy-based baselines.

I am aware of the University of Windsor Senate Policy on Authorship and I certify that I have properly acknowledged the contribution of other researchers to my thesis, and have obtained written permission from each of the co-author(s) to include the above material(s) in my thesis.

I certify that, with the above qualification, this thesis, and the research to which it refers, is the product of my own work.

II. Declaration of Previous Publications

This thesis includes three original papers that have been or are soon expected to be published in peer reviewed journals, as follows:

Thesis Chapter	**Publication title/full citation**	**Publication Status**
2.4	Marchwica, P., J. H. Sokolowski, et al. (2011). "**Fraction solid evolution characteristics of AlSiCu alloys - dynamic baseline approach.**" Journal of Achievements in Materials and Manufacturing Engineering 47(2): 22.	Published
2.3.1 4.7 4.9	Marchwica, P., Sokolowski, J. H., Gesing, A. J., Jekl, J., Blawert, C., Berkmortel, R. (2012) "**Combination of Cooling Curve and Micro-Chemical Phase Analysis of Rapidly Quenched Magnesium AM60 Alloys.**" TMS 2012, Orlando, Florida, March 11-15, 2012, "Magnesium Technology 2012", pp.519-524	Published
2.3.2 4.8 4.9	Marchwica, P., Sokolowski, J. H., Gesing, A. J., Jekl, J., Blawert, C., Berkmortel, R. (2012) "**Thermal and Microchemical Phase Analysis of the Rapidly Quenched Magnesium AE44 Alloy.**"	Ready for submission

I certify that the above material describes work completed during my registration as a graduate student at the University of Windsor.

I declare that, to the best of my knowledge, my thesis does not infringe upon anyone's copyright nor violate any proprietary rights and that any ideas, techniques, quotations, or any other material from the work of other people included in my thesis, published or otherwise, are fully acknowledged in accordance with the standard referencing practices. Furthermore, to the extent that I have included copyrighted material that surpasses the bounds of fair dealing within the meaning of the Canada Copyright Act, I certify that I have obtained a written permission from the copyright owner(s) to include such material(s) in my thesis.

I declare that this is a true copy of my thesis, including any final revisions, as approved by my thesis committee and the Graduate Studies office, and that this thesis has not been submitted for a higher degree to any other University or Institution.

Abstract

This thesis is an examination of the effects of varying cooling rate on the solidification properties of AlSi and MgAl alloys. Rapid cooling accessories for the Universal Metallurgical Simulator and Analyzer Technology Platform (UMSA) were developed that enabled quenching up to peak rates of 520°C/s. Samples from four automotive production alloys (aluminum A356 and a Sr-modified Al-20wt.%-Si alloy as well as magnesium AM60B and AE44) were resolidified under a range of cooling rates. Resultant micrographs revealed improvements to the microstructure, especially for the modified hypereutectic alloy. The AM60B microstructure also indicated invariance to cooling rate. Thermal data from the magnesium alloys was used in the development of baseline and fraction solid calculations that are extensible to higher cooling rates. Though these techniques cannot yet be applied to the highest cooling rates, excellent phase composition data for the AM60B alloy was generated for cooling rates of approximately 20°C/s (peak).

Acknowledgements

No man is an island and although it's my name on the front of this thesis it still very much a collaborative effort. I would be remiss if I didn't thank some of the many people that helped make it possible, in no particular order.

Thanks to John Jekl and Richard Berkmortel of Meridian Lightweight Technologies Inc. for providing materials and advice for magnesium experimentation.

Many thanks to Sharon Lackie of the Great Lakes Institute for Environmental Research for her expert knowledge in SEM operation and her willingness to try new things with expensive machinery when trace elements needed to be quantified.

Schönen dank to Dr. Carsten Blawert of GKSS Helmholtz-Zentrum Geesthacht GmbH who furnished us with fantastic quality micrographs of magnesium samples.

Great thanks to Dr. Adam Gesing of Gesing Consultants Inc. An unparalled expert in the field of magnesium research, Dr. Gesing was integral to much of the magnesium investigations and without his insight and careful calculations, progress on new baselines would not have been achieved.

Wielkie dzięki to Dr. Marcin Kasprzak of the Silesian University of Technology. It is his technical prowess that made the UMSA and this research possible, and his thorough knowledge of the platform has helped me out of interesting problems a number of times.

A grateful tip of the hat to the University of Windsor's Technical Support Centre and in particular, Andy Jenner, for supporting our lab and its operations. Their machining skill gave physical form to our ideas, and without the samples they manufactured progress would have been very hard to achieve.

Thanks as well to Ellen Moosberger, for her tireless scouring of this hefty document and for having the sharp eye to spot the mistakes that I, a former newspaper proofreader, didn't even catch. Beyond just this document, she has been indispensable in keeping the lab running smoothly and handling the mountain of behind-the-scenes paperwork which sometimes goes underappreciated.

Much appreciation must also go out to my MASc colleagues and lab-mates; Nathan Reade, Roja Moradipour, Joe Giovanatto, Victoria Townsend, Mohammed Alam, Albion Demiri and Tanzim Nasir. Whenever I was stuck on a problem, they were always the first

people I could turn to. They imparted the wisdom of the lab unto me so that I may in turn hand it to the next generation, and they were enormously pleasant people to work with.

Though no longer a MASc student, I must also issue hearty thanks to Dr. Al Conle, a key member of the lab whose expertise has been instrumental in developing certain projects. Although the projects I have had the pleasure of working on with him did not ultimately make it into this thesis, he was nevertheless a great and generous person to work with and an even better person to talk to about any topic under the sun.

Thanks to my beautiful wife, who was a source of inspiration (even though I may not have met her yet). One day in the future, I may have need of a line like this to refer to.

Thanks go out to AUTO21 Networks of Centres of Excellence, an automotive research and development program focusing on issues relating to the automobile in the 21st century. Special thanks also to the Natural Sciences and Engineering Research Council of Canada (NSERC) Discovery Grant Program for providing funding to undertake the research presented in this body of work. Even more thanks go to the Foundry Educational Foundation, FEF, who has not only been a supporter of projects in our lab but also a personal supporter of mine in the form of generous scholarships.

Thanks must also be given to my committee members, Drs. Altenhof, Sobiesiak and Urbanic. Though I didn't have the opportunity to work with them too closely on my thesis project, their help and feedback was much appreciated in creating the final product. I am also extremely grateful for their confidence in my research during the proposal stage. I must, however, give special thanks to Dr. Urbanic, who truly went above and beyond in providing me with advice and support on matters both academic and otherwise.

An enormous debt of gratitude is owed to Dr. Sokolowski, who took me in as his student. He is a remarkable professor and shows a rare enthusiasm for developing new ideas into tangible products. Throughout my time here he has been truly generous in providing me with both funding and also ample opportunity to get involved in complex industry projects.

Finally, the utmost thanks must go to my loving and supportive parents who were with me every step of the way during my masters. Though they may never read this thesis, it is only because of them that I am here to write it.

Table of Contents

List of Figures

List of Tables

List of Abbreviations, Symbols and Nomenclature

Al20SiSr	Aluminum, 20 wt%. silicon alloy with strontium modification. An alloy produced for this research. A full chemical composition is found in the text.
AlTAP	Aluminum Thermal Analysis Platform (UMSA prototype)
BL	Baseline
CA-CCA	Computer Aided Cooling Curve Analysis
CR	Cooling Rate (°C/s) - Average rate of temperature change between two points during the cooling cycle (normally above liquidus and below solidus)
DBL	Dynamic Baseline (specific form of baseline developed at the University of Windsor)
DSC	Differential Scanning Calorimetry
DTA	Differential Thermal Analysis
dT/dt/t	Derivative versus time of a thermal curve plotted against time
dT/dt/T	Derivative vs. time of a thermal curve plotted against temperature
ED	Equivalent Diameter
f_s	Fraction Solid (%, or [0, 1])
LH	Latent Heat
LOM	Light Optical Microscopy
MCPT	Metal Casting and Post-Processing Technology (name of laboratory)
NHB	Newtonian Heat Balance
RE	Rare Earth elements (e.g. Ce, La)
SDAS	Secondary Dendrite Arm Spacing
SEM	Scanning Electron Microscopy
Si_{EQ}	Silicon Equivalency
SR	Solidification Rate (°C/s) - Average rate of temperate change in the semi-solid region
TA	Thermal Analysis
TTP	Time Temperature Property
TTT	Time Temperature Transformation
UMSA	Universal Metallurgical Simulator and Analyzer Technology Platform
UTS	Ultimate Tensile Strength
YS	Yield Strength

Internal codes for identifying samples (e.g. AL2, MG5) and regions for metallography (LTL, RML) are used within the results and are outlined in Sections 3.3 and 4.1 respectively.

Chapter 1 Introduction

1.1 Background

Light metal casting is an integral component of today's modern economy with applications found in virtually any technological sector, though in particular automotive and aerospace. Metallurgists are constantly working to develop improved alloys through combinations of chemistry and processing. Thermal Analysis (TA) is an indispensable technique to aid in this development. Each alloy and process has a unique thermal signature which can be identified with highly-sensitive instruments detecting temperature changes during heating and cooling processes. These signatures can be analyzed to reveal a wealth of information about the alloy, including fraction solid information which can lead to an improved understanding of microstructural development. Unlike many other analysis techniques, TA can be used 'on-line' and is able to efficiently aid in prediction of alloy properties in a production environment.

Significant work in the area of thermal analysis has been done on identifying the effects that chemical changes, such as the composition of Si and Cu, have on the resultant thermal curves and microstructural/mechanical properties. This sort of work has led to accurate baselines and fraction solid information for alloys solidified at quasi-equilibrium rates. An area that requires further study, however, is the evolution of fraction solid information as cooling rates increase. Rapid cooling, in the presence of adequate feeding conditions, is generally desirable in industry because it generates highly-refined grain structures and allows alloying elements to remain dissolved in the matrix as opposed to intermetallic precipitation. However, in order for thermal analysis to aid alloy development at increased rates, new hardware and mathematical models need to be created. This thesis is focused on the experimentation and subsequent analysis of samples and thermal data generated using new hardware accessories developed for the Universal Metallurgical Simulator and Analyzer Technology Platform (UMSA).

1.2 Objectives

The primary goal for this research was to develop accessories for the UMSA Technology Platform to allow for investigations into high[1] cooling rates (100+ °C/s). Once these accessories became available it was necessary to evaluate them using a range of test parameters and alloys. There were two main branches of investigation; one on aluminum alloys and the other on magnesium alloys.

a.) Aluminum tests were done on two alloys, A356 and a modified Al20%Si alloy. The former is a highly popular hypoeutectic alloy and was chosen due to concurrent investigations into the effects of high pressure. The Al20%Si alloy is a continuation of earlier work done by the MCPT group and focuses on the effects of silicon modifiers during rapid solidification.

Deliverables: Thermal and microstructural data for these two alloys under a range of processing conditions.

b.) Magnesium tests were done on two alloys, AE44 and AM60B, which are both used in the automotive industry. The goal of these tests was to develop improved fraction solid and baseline models which are applicable at higher solidification rates.

Deliverables: Thermal and microstructural data for these two alloys under a wide range of processing conditions, as well as an improved methodology for baseline calculation.

1.3 Notes on the Text

This thesis favours the use of the term ‘Cooling Rate’ instead of the similar ‘Solidification Rate’. The distinction between the two is that ‘Solidification Rate’ focuses on a narrow range of temperatures, those between liquidus and solidus, while ‘Cooling Rate’ can apply to the entire cooling cycle. While increasing the SR is technically the desired goal since it refers to the region that is most metallurgically interesting, the term

[1] Because casting is used for many different applications, part geometries and alloys, there is no clear consensus for what ‘high’ is. The use of the word ‘high cooling rate’ is relative to existing literature for similar experiments, which is often below 5°C/s.

‘Cooling Rate’ is preferred since most processing conditions and analysis will also apply to temperatures outside of the semi-solid region. The literature contains many conventions for reporting the cooling rate, such as individual averages for liquid, solid and semi-solid regions. This thesis follows an existing convention that is outlined in Section 4.1.

By an internal convention and unless otherwise noted, the cooling rates for thermal curves presented in the results refer to the peak instantaneous cooling rate present in the first derivative vs. temperature graph. This peak temperature is affected by several factors, notably the holding temperature of the sample, and may not reflect the true average solidification rate in the semi-solid region however the curves are more easily identified when using peak values.

While first derivative data for cooling curves shows a negative value for the rate of temperature change, values for the cooling rate, both peak and average, are reported as positive numbers. This makes sense intuitively (more cooling, higher number) and because heating rates are not investigated in the text, there should not be any confusion.

Chapter 2 Literature Review

2.1 Cast Aluminum and Alloy Designation

Aluminum alloys are most commonly classified according to a system established by The Aluminum Association. The nomenclature used divides alloys according to a number of criteria, including chemistry and processing (i.e. cast vs. wrought alloys). In the case of cast aluminum alloys (a similar system exists for wrought alloys), the families are shown in Table 1.

Table 1 - Aluminum alloy families for casting compositions [1].

Code	Description
1xx.x	Unalloyed (pure) compositions
2xx.x	Copper as principal alloying element, other elements may be included
3xx.x	Silicon as principal alloying element, other elements (e.g. Cu or Mg) included
4xx.x	Silicon as principal alloying element
5xx.x	Magnesium as principal alloying element
6xx.x	Unused
7xx.x	Zinc as principal alloying element, other elements (e.g. Cu or Mg) included
8xx.x	Tin as principal alloying element
9xx.x	Unused

In this nomenclature, 'xx' is a unique code that identifies a specific alloy composition within the family of alloys. The 'x' following the decimal point refers to alloy composition limits and indicates either cast composition limits (.0) or ingot composition limits (.1 or .2) [1]. A letter added as a prefix to a code indicates a specific restriction to the alloy such as a limitation on impurity elements (e.g. between primary and secondary alloys). As an example of differences between designations and the alloys they refer to, Table 2 compares two alloys, 356.0 and A356.0.

Table 2 - Comparison of two alloy designations and their chemistries [1].

Code	Composition (Trace elements excluded)	Properties and Application
356.0	6.5-7.5 Si, 0.25 Cu, 0.20-0.45 Mg Max: 0.35 Mn, 0.60 Fe, 0.35 Zn, 0.25 Ti	Excellent castability, good weldability and resistance to corrosion. Good for automotive transmission cases.
A356.0	6.5-7.5 Si, 0.20 Cu, 0.25-0.45 Mg Max: 0.10 Mn, 0.20 Fe, 0.10 Zn, 0.20 Ti	High-strength. Good for nuclear energy installations and permanent molds.

AlSi alloys are broadly divided into three categories based on the amount of silicon present, relative to the AlSi eutectic point, approximately 12.6 wt.% Si. These categories are: hypoeutectic (below the eutectic point), eutectic (at or near the eutectic point) and hypereutectic (above the eutectic point). The binary phase diagram for AlSi is shown in Figure 1.

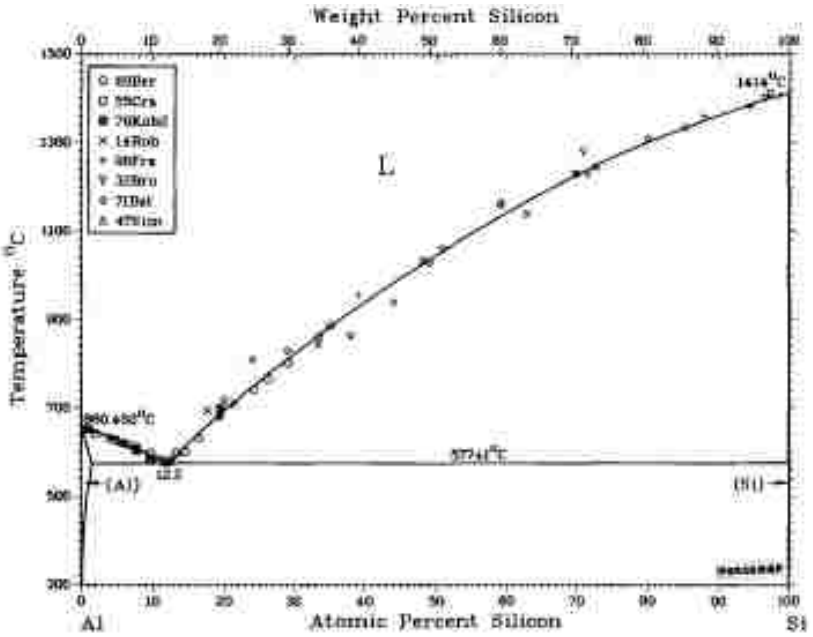

Figure 1 - AlSi binary phase diagram [2].

2.1.1 Hypoeutectic Aluminum-Silicon Alloys

Hypoeutectic AlSi alloys contain < 12.6% silicon. Selected hypoeutectic alloys with approximate Si (and Cu) composition are shown in Figure 2.

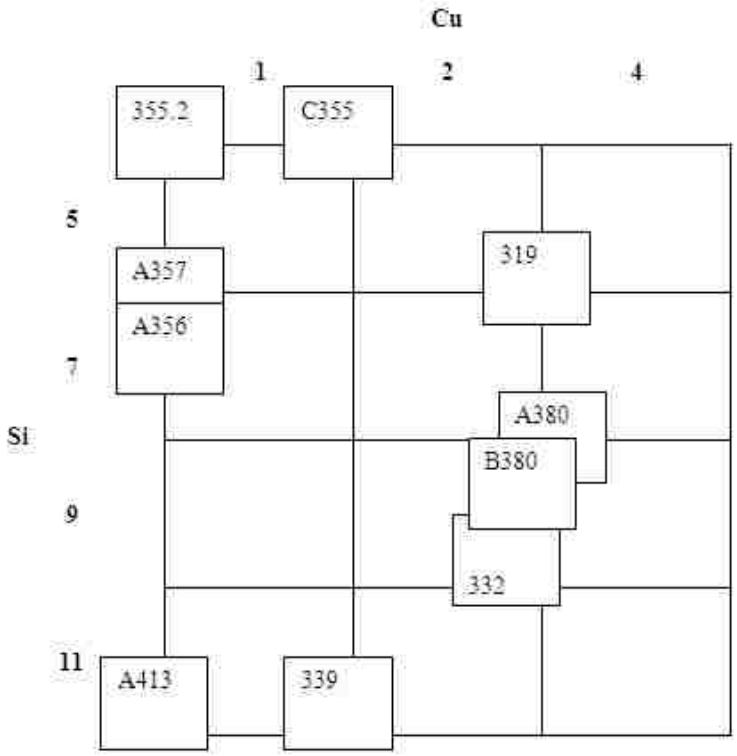

Figure 2 - Matrix of [Si/Cu] nominal compositions with overlaid compositions of selected members of the 3XX alloy family [3].

Aluminum alloy 356, described briefly in Section 2.1 is the principal hypoeutectic alloy investigated in this study. The common solidification reactions for 356 are shown in Table 3 below, which are reproduced from analyses by Bäckerud et al. [4].

Table 3 - Reactions during solidification of aluminum alloy 356.

Reaction No.	**Reaction**	**Suggested Temperature (°C)**
1	Development of dendritic network	614
2a	Liq. → Al + $Al_{15}(Mn,Fe)_3Si_2$	594
2b	Liq. → Al + Al_5FeSi + $Al_{15}(Mn,Fe)_3Si_2$	594
3	Liq. → Al + Si + Al_5FeSi	575
4	Liq. → Al + Si + Mg_2Si	555
5*	Liq. → Al + Si + Mg_2Si + $Al_8Mg_3FeSi_6$	554

* Detected only at higher cooling rates (5°C/s in this example)

The reason for the 'suggested' temperature is that solidification events will shift considerably in response to changes in the solidification rate. Some phases, such as $Al_8Mg_3FeSi_6$ in this example will not even be visible at low rates. Table 4 below shows a comparison of selected properties of 356 and how they differ at two different cooling rates [4].

Table 4 - Comparison of selected properties of 356 in relation to cooling rate [4].

Property	**0.2°C/s Cooling Rate**	**5°C/s Cooling Rate**
Temp. of Reaction 1 (°C)	612-610	614-611
Temp. of Reaction 2 (°C)	594-571	590-574
Temp. of Reaction 3 (°C)	569-568	565-562
Temp. of Reaction 4 (°C)	553-559	548-541
Temp. of Reaction 5 (°C)	N/A	541-505
f_s of Reaction 1 (%)	12	32
f_s of Reaction 2 (%)	19	11
f_s of Reaction 3 (%)	25	22
f_s of Reaction 4 (%)	3	7
f_s of Reaction 5 (%)	N/A	9
Dendrite Arm Spacing (μm)	95	33
Solidification Temp. Range (°C)	73	109

Figure 3 shows microstructures for 356. Certain phases are visible in the microstructure shown in Figure 3a) which was taken from a sample cooled at 0.2°C/s. These are the well-developed $Al_{15}(Mn,Fe)_3Si_2$ phase (1, brown Chinese script), the large Al_5FeSi needle (2, dark brown) and the smaller Mg_2Si precipitates (3, dark grey). Figure 3b) shows the eutectic areas of a sample cooled at 0.6°C/s.

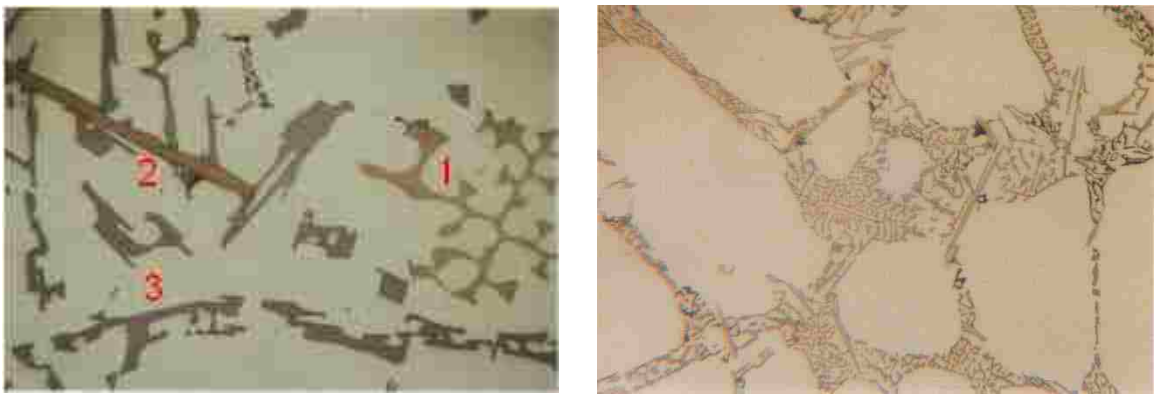

a) 0.2°C/s b) 0.6°C/s

Figure 3 - Microstructure of a sample of 356 (560x Magnification) [4].

2.1.2 Hypereutectic Aluminum-Silicon Alloys

Hypereutectic AlSi alloys contain > 12.6% Si. A common example of this alloy used in industry is A390 (17% Si). Though not as often used as hypoeutectic alloys, they have a number of properties that make them well-suited to specific applications. They are usually characterized as having excellent wear resistance, thermal conductivity and weight reduction in comparison with hypoeutectic alloys. The higher levels of silicon also minimize thermal expansion and increase thermal conductivity [5].

2.2 Key Aluminum Alloying and Impurity Elements

2.2.1 Silicon - Alloying Element

Additions of silicon to aluminum are very common in casting products and silicon is the main alloying element in both the 3XX and 4XX series of alloys. Silicon is added in order to improve fluidity, decrease shrinkage as well as improve wear resistance [6]. The increase in fluidity comes from the large amount of latent heat that is released during the crystallization of silicon [7].

Silicon has limited solid solubility in the aluminum matrix and at the eutectic point the aluminum matrix only contains 1.65% Si [6]. The bulk of the silicon is in the form of crystals, the morphology of which impacts the overall mechanical properties. Certain elements such as Na or Sr can be added to an alloy to modify the morphology of silicon particles.

2.2.2 Copper - Alloying Element

Additions of copper in aluminum alloys grant improvements to hardness (concentration dependent) as well as strength (distribution dependent) [8]. Ductility, also distribution-dependent, is normally worsened with the addition of copper [8, 9]. Additions of copper will also increase the level of porosity. The maximum equilibrium solubility of copper is 5.65%, with commercial AlSiCu alloys containing around 1%. The weight ratio of Cu:Mg in the alloy will determine certain properties and increasing the ratio (usually ≥ 1.5 in commercial applications) will improve hardness. Low ratios (< 1) can lead to helical dislocations and Cu-Mg clustering. Additions of copper in concentration from 1% to 4% cause a reduction in the SDAS as well as an increase in grain size. Copper will also increase precipitation kinetics and refine certain precipitates during artificial aging [10].

2.2.3 Strontium - Silicon Modifier

Strontium is widely used for modifying the eutectic silicon in AlSi casting alloys. Unfortunately, strontium also has the effect of increasing the hydrogen and inclusion content of AlSi alloys, requiring a degassing step after modification is performed. Increasing concentrations of hydrogen within an aluminum melt will tend to increase the presence of porosity [11]. As well as an increase in porosity, due to increased nucleation sites and reduced surface tension, the morphology of the porosity is also changed, resulting in smoother, rounder and regular pores [12]. Other literature sources have noted, however, that Sr has less of an effect on porosity than other factors, such as local solidification time or dissolved hydrogen [13]. A wide range of strontium concentrations is used in the industry. A range of 0.015 to 0.050% is standard industry practice and good modification is normally achievable in the range of 0.008 to 0.015% Sr [14]. Previous studies of AlSiCuMg alloys have shown negative effects when using strontium for silicon modification. A series of experiments done on aluminum alloy 320 with 0.005 – 0.007 wt.% Sr additions have shown drastic increases in pore size (5.6x higher) as well as percentage porosity (4x higher) with subsequent decreases in ultimate tensile strength (UTS) (12% lower), yield strength (YS) (3% lower) and % elongation (0.2%, down from 0.4%). Ultimately the study concludes that in order to take advantage of Sr modification, one must employ higher cooling rates [15].

2.2.4 Iron - Impurity

Iron is the most common impurity found in aluminum alloys. The solid solubility of iron in aluminum is relatively low (0.05%) with excesses appearing as intermetallics at the grain boundaries. Common iron phases in AlSi alloys include Al_3Fe, Al_6Fe, $Al_{12}Fe_3Si$ and $Al_9Fe_2Si_2$. The presence of Fe intermetallics has the effect of increasing yield strength (~7 MPa / vol.%). However, depending on the size, chemistry and distribution, Fe constituents can cause cracking and notches which have a negative impact on fatigue resistance [9].

2.2.5 Manganese - Alloying Element

Manganese may be added to alloys to increase strength. Manganese precipitates increase the quench sensitivity of heat-treatable alloys. Manganese is also used to control the shape of acicular or platelike iron constituents and decrease the embrittling effects. It is a common addition to 3xxx alloys up to 1.25 wt.%, often in conjunction with magnesium. The addition of manganese will, however, decrease the resistivity of the alloy [1]. Manganese has quite limited solid solubility in aluminum (1.8 wt.% as a principal alloying element) and will form intermetallics that decrease ductility [6].

2.2.6 Magnesium - Alloying Element

Like copper, the addition of magnesium to AlSi alloys will increase strength and reduce ductility. Magnesium will also reduce the modification level of Sr-modified alloys [8]. Adding magnesium to Al-Cu alloys will also increase the magnitude and rate of natural and artificial aging. The preferential precipitation of magnesium at grain boundaries produces susceptibility to intergranular cracking and stress corrosion [1].

2.2.7 Tin - Impurity

Tin is most often an impurity element in aluminum alloys. It may, however, be added for a specific purpose at levels as low as 0.03 wt.% in wrought to 25 wt.% in some casting alloys. Small amounts of tin will increase the response of AlCu alloys to solution treatment, resulting in increased strength and corrosion resistance; higher concentrations

may lead to hot cracking. AlSn alloys can be made to withstand high speeds, loads and temperatures and can gain improved wear resistance with additions of copper, nickel and silicon. Tin may also cause surface darkening during annealing, leading to decreased corrosion resistance, unless additions of copper are made [1]. Tests on aluminum 319 revealed that tin reduces hardness only in the heat treated condition. Yield strength is reduced at tin levels above 0.035% (UTS not affected) and elongation is increased from 0.7% to 1.1% as tin concentrations approach 0.1% (heat treated permanent mould and zircon sand). If magnesium is present in sufficient quantity (0.35% - 0.4%), free tin and Mg_2Sn are found in the as-cast structure (Mg_2Sn only after heat treatment). At low levels of magnesium (0.01%), Mg_2Sn cannot form and the free tin causes a deterioration of properties [16].

2.2.8 Phosphorous - Impurity

Phosphorous is a contaminant that interferes with modification agents, such as Sr and Na. Primary producers may try to limit phosphorous concentrations in alloys to less than 5 ppm, a level at which modifiers are still effective. If phosphorous levels are elevated, they will bond to modifiers and produce phosphides which no longer have a modifying effect. Phosphorous may enter the melt via a number of vectors, such as phosphate-bonded refractories, and if high concentrations are present it may be necessary to increase the amount of modifying agent to negate phosphide losses [14].

2.3 Cast Magnesium Alloys[2]

With low density and good mechanical properties, magnesium alloys are increasingly being adopted for use in the automotive industry. As a lightweight structural material they feature excellent ductility, castability and strength and are currently being used for such components as instrument panels, seat frames and steering wheels [17-19]. Many magnesium alloys, such as AM60B, have been developed in order to obtain specific ranges of properties. AM60B, with additions of aluminum and manganese, has good

[2] This section incorporates material that is the result of joint research.

energy-absorption characteristics and ductility [20]. Die casting is the predominant forming method for Mg-based alloys. Large markets for such die-cast alloys include portable consumer electronic housings and automotive/aerospace components. These applications involve use at ambient temperature. Other uses such as engine components expose the alloy to elevated temperature and thus require higher temperature strength and creep resistance.

2.3.1 AM60B

AM60B is a general purpose die-casting alloy containing ~6% Al and >0.3% Mn (wt.%). Intended for ambient temperature applications, AM60B is designed for low cost, low density, good castability, and room temperature strength and improved ductility over the industry workhorse AZ91D alloy. In AM60B, the addition of Al improves the castability by providing the $Mg_{17}Al_{12}$ intermetallic phase, which preserves fluidity during casting until a low temperature (~400°C) eutectic reaction with Mg. Mn has a high affinity for impurities such as Fe and Ni (which lead to electrochemical corrosion) and traps them in Al_8Mn_5 intermetallic precipitates. Under thermodynamic equilibrium, these precipitates form in liquid Mg just above its melting point of 650°C and can be removed with additional melt treatment. Without melt treatment, these precipitates can provide nucleation sites for the solidification of primary αMg grains. Such nucleation promotes reduction of grain size and thus contributes to the improvement in strength and ductility.

2.3.2 AE44

AE44 is an alloy being considered for elevated temperature engine component applications. It contains ~4% Al and ~4% rare earth (RE) element mischmetal containing Ce, La, Nd and smaller amounts of other RE elements. It sacrifices solidification range in exchange for high temperature phase and microstructural stability, which translates to retention of strength and high creep resistance over extended use times.

RE metals have similar valence electron shells and thus similar chemical behavior. They are often found together and upon reduction and refining form mischmetal. In spite of being called ‘rare,’ their abundance is similar to Ni and Co and RE metals are suitable as alloying element additions for alloys used in large-scale markets such as automotive

and aerospace where improved high-temperature mechanical performance is required [21].

RE metals form similar intermetallic crystal structures when bonded with Al as $Al_{11}RE_3$ or Al_3RE. Ce, La, Nd, Pr and Gd substitute freely on the RE sites in the intermetallic crystal. The result is that a Mg-Al-RE mischmetal system behaves similarly to a ternary alloy system forming few intermetallic phases. Furthermore, there is very high chemical affinity between Al and the RE elements. This reduces Al activity in the liquid alloy and suppresses formation of intermetallic phases typically found in the Al-Mg-X systems. Al-RE intermetallics form at temperatures very close to the liquidus temperature of αMg and by consuming the Al from the liquid they drastically reduce the solidification range compared to what would be expected for a Mg alloy containing 4% Al alone.

2.4 Thermal Analysis[3]

2.4.1 Cooling Curve Analysis (CCA)

Foundries are under constant pressure from customers to maintain consistent quality in their cast components. The measure of a component's quality can refer to a variety of attributes, such as chemistry, mechanical properties or dimensions, and there are a number of techniques which can be employed for assessment. Reduced pressure testing is often used for the determination of hydrogen content and its relationship with porosity. Light Optical Microscopy (LOM) is often used for microstructure measurements. Unfortunately, techniques such as these are very costly in terms of time and with the ever-increasing demands of industry, it becomes impractical to rely on them for on-line quality assessment. By comparison, thermal analysis is a relatively quick and inexpensive process which can be used on the foundry floor.

There are several variations of thermal analysis that exist. These include Differential Scanning Calorimetry (DSC), Differential Thermal Analysis (DTA) and Cooling Curve Analysis (CCA). However, all of these operate similarly in principle. They measure the

[3] This section incorporates material that is the result of joint research.

changes in temperature in a sample that occurs as it is heated or cooled through phase transformation intervals. The record of these temperatures is a unique profile which can be analyzed in order to derive metallurgical characteristics of the sample.

CCA, as used in this study, deals with temperature measurements gathered using one or more thermocouple(s) inserted within the bulk of a sample during a heating/cooling cycle. During the cooling process, latent heat releases get interpreted as a change in the slope on the cooling curve. These changes are proportional to the volume fraction of the phases undergoing transformation. Phases appearing in small amounts are harder to detect on a cooling curve, which is why the first derivative of the curve is commonly used for analyzing data. These thermal curves and their derivatives can be used to identify key metallurgical characteristic points. These points can, for example, be used to identify alloy composition with the aid of phase diagrams. The Silicon Modification Level (SiML) and the degree of grain refinement can also be quantified using CCA techniques [22]. The precision, accuracy and repeatability of the changes in the cooling curve are identical to those in the heating curve. Though research on cooling rates looks primarily at cooling curve data, the heating curve and its derivatives are utilized for heat treatment and semi-solid processing.

Although the thermal analysis techniques listed have their own advantages and disadvantages, CCA is particularly attractive because it is the easiest to implement on the foundry floor. The other two techniques rely on complicated and expensive instrumentation and strict sampling procedures, neither of which is attractive or efficient [23]. Another key feature of CCA, compared to DSC, is the ability to use macro-sized samples which can be later analyzed and compared to the thermal information.

2.4.2 Solidification Sequences

The effects of latent heat releases visible on thermal curves obtained using CCA methodologies correspond to metallurgical phases within the alloy. The types of phases present and their morphology are largely dependent on chemical composition. The proportions of phases may vary between alloys of similar chemical composition however they will still generally exist in some quantifiable amount. Other process factors such as cooling rate have an effect on the morphology and distribution of phases within an alloy's

microstructure. As an example, a summary of metallurgical events corresponding to major observable phases in the solidification sequence of AlSiCu alloys is shown in Table 5. Undercooling, #4 and #8 in Table 5, is the event when the temperature of a melt reaches a point below the transformation temperature and is followed by recalescence, a increase in temperature to return to the transformation temperature. The numerical value for undercooling is the lowest temperature during undercooling subtracted from the highest value during recalescence.

Table 5 - Selected metallurgical events during solidification of AlSiCu alloys [22].

#	**Temp. Symbol**	**f_s Symbol**	**Meaning**
1	T_{liq} / $T^{\alpha,DEN}_{NUC}$	0%	The temperature of α Al dendrite nucleation. Identical to liquidus temperature since it is the first solidification transformation.
2	$T^{\alpha,DEN}_{MIN}$	$f_s^{\alpha,DEN}{}_{MIN}$	α Al undercooling temperature (minimum temperature reached below transformation temperature).
3	$T^{\alpha,DEN}_{G}$	$f_s^{\alpha,DEN}{}_{G}$	α Al growth temperature (maximum reached above transformation temperature).
4	$\Delta T^{\alpha,DEN}_{UNDER}$	$\Delta f_s^{\alpha,DEN}{}_{UNDER}$	Undercooling (Equal to #3 - #2).
5	$T^{AlSi}_{E\ NUC}$	$f_s^{AlSi}{}_{E\ NUC}$	AlSi eutectic nucleation temperature.
6	$T^{AlSi}_{E\ MIN}$	$f_s^{AlSi}{}_{E\ MIN}$	AlSi eutectic undercooling temperature.
7	$T^{AlSi}_{E\ G}$	$f_s^{AlSi}{}_{E\ G}$	AlSi eutectic minimum temperature.
8	ΔT^{AlSi}_{UNDER}	$\Delta f_s^{AlSi}{}_{UNDER}$	Undercooling (Equal to #7 - #6).
9	T^{MgSi}_{NUC}	$f_s^{MgSi}{}_{NUC}$	Magnesium silicides (not investigated in this paper).
10	$T^{AlSiCuMg}$	$f_s^{AlSiCuMg}$	Copper/Magnesium rich phase nucleation.
11	T_{sol}	100%	Solidus temperature.

For a specific alloy composition, repeated tests (with the same process parameters) will show that the metallurgical events shown in Table 5 tend to occur at the same temperatures and fraction solid percentages. This repeatable curve serves a unique thermal signature for an alloy. Figure 4 shows the cooling curve for a nominal AlSiCu alloy (nominal 5 wt.% Si and 1 wt.% Cu) with numbers corresponding to the metallurgical events in Table 5.

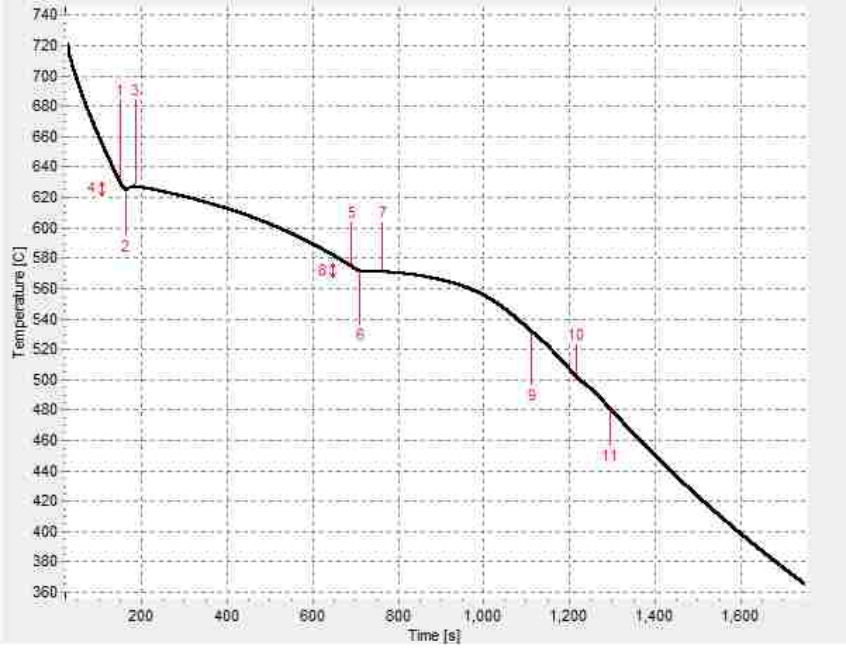

Figure 4 - Temperature vs. time cooling curve of a nominal 5 wt.% Si and 1 wt.% Cu aluminum alloy.

Figure 5 shows the first derivative (versus time) of the same cooling curve versus temperature (abbreviated dT/dt/T) and demonstrates that metallurgical events are more clearly identifiable in this form. The red line overlaid on the first derivative curve is an example of a baseline curve, specifically a dynamic baseline (DBL). The baseline can be defined as a hypothetical path which the first derivative curve would follow if there were no latent heat releases. This baseline concept is further explained in Section 2.4.4. Though it may appear unusual to see spikes of positive heating rates during a cooling cycle, this is only due to temporary recalescence and is not representative of the cooling as a whole. **Note:** The derivative for the entire heating/cooling cycle would form a clockwise closed loop from left to right to left. Since only the derivative for the cooling curve is shown, the metallurgical events are shown from right to left, which is a standard convention.

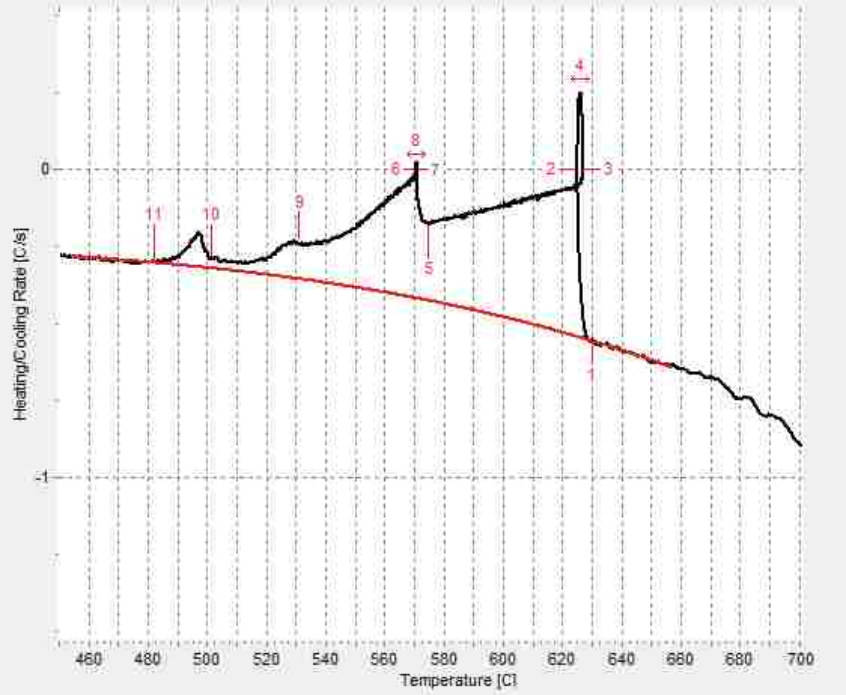

Figure 5 - dT/dt/T of a nominal 5 wt.% Si and 1 wt.% Cu aluminum alloy with overlaid Dynamic Baseline.

Because CCA can be used under a wide range of experimental configurations, thermal curves obtained will reflect the testing parameters. However, all test samples of the same chemistry will share similar or identical characteristics in their thermal curves. Ideally, repeated trials of the same alloy subjected to the same quasi-equilibrium solidification will produce identical thermal curves. However, once cooling rates increase it becomes more difficult to identify metallurgical characteristics and temperature/fraction solid values may drift to some degree. Applying pressure to a solidifying melt will also have an effect on the thermal curve however even in high pressure die casting operations the metallurgical characteristics remain well-defined.

2.4.3 Fraction Solid

The fraction solid of a solidifying melt is a percentage of the solid phase(s) that have precipitated at a point in time between the liquidus and solidus points (the so-called ‘mushy zone’ or ‘semi-solid region’). An accurate fraction solid model is essential in order to produce computer simulations of solidification processes. There are several

different methods in the literature that can be used to determine the fraction solid. One method is performed with quantitative metallography using image analysis. A set of samples are rapidly solidified at various temperatures within the mushy zone. If the solidification is sufficiently rapid, it will preserve the microstructure present at that particular temperature. These samples can then be analyzed using image analysis and the volume fraction of individual phases observed can be used to build a fraction solid model. Another method measures the mechanical response (e.g. indentation) of solidifying metals and estimates the fraction solid. However, such empirical methods are time consuming and not suited to a demanding commercial foundry environment.

The literature also presents several mathematical models that can be used to determine the fraction solid which are shown in Table 6.

Table 6 - Selected fraction solid models present in the literature.

#	f_s MODELS	COMMENTS
1	**LINEAR** $f_s = \frac{T_{liq} - T}{T_{liq} - T_{sol}}$ T_{liq}- Liquidus temperature T_{sol}- Solidus temperature T – Instantaneous temperature	Latent heat of fusion is assumed to vary linearly between T_{liq} & T_{sol} temperatures. This model has no theoretical basis, but is frequently used due to its simplicity.
2	**LEVER RULE** $k = \frac{T_m - T_{liq}}{T_m - T_{sol}}$ $\quad f_s = \frac{1}{1-k} \cdot \frac{T_{liq} - T}{T_m - T}$ k - Distribution coefficient of binary alloy T_m - Melting temperature of pure metal	Equilibrium solidification is assumed to progress very slowly and the solid and liquid phases coexist in thermodynamic equilibrium in the mushy zone. f_s is determined by the lever rule.
3	**SCHEIL** $f_s = 1 - \left(\frac{T_m - T}{T_m - T_{liq}} \right)^{\frac{1}{k-1}}$	It is assumed that no solute diffusion occurs in the solid phase (which results in segregation) and also that the liquid is perfectly homogeneous (assumed complete diffusion).
4	**GRAIN NUCLEATION** $f_s = 1 - \exp\left(-\frac{4}{3} \cdot \pi \cdot R^3 \cdot N \right)$ R-Average grain radius N-Average grain density	The calculation of f_s is based on the grain nucleation law and on the assumption that the shape of the grains is spherical.
5	**DSC METHOD OF PARTIAL AREAS** $f_s(T) = 1 - (1/m\Delta H)Q(T)$ $Q(T)$ - Heat absorbed from melting to T m - Mass of the sample ΔH - Heat of melting	f_S equation is an approximation by assuming that, the heat of melting is independent of the temperature and thus the composition of the solid phase is linearly proportional to the amount of the melted alloy.
6	**FOURIER METHOD** $f_S(t) = \frac{1}{L} \int_{t_S}^{t} \left(\frac{\partial Q}{\partial t} \right)_t (t)\, dt$ L – Latent heat Q – Latent heat of solidification	Fourier's model considers the effect of thermal gradient (at least two thermocouples are needed) during solidification and assumes that the heat transfer takes place by conduction only. Cylindrical or spherical samples are used.
7	**SEGMENTATION MODEL - 319 alloy** $f_S^{\ I} = (T_{liq} - T)/(T_{liq} - T^{AlSi}_{E,G})^{n1}\, f_S^{\ AlSi}$ $f_S^{\ II} = f_S^{\ AlSi} + (T^{AlSi}_{E,G} - T)/(T^{AlSi}_{E,G} - T^{AlCu}_{E,G})^{n2}\, (f_S^{\ AlCu} - f_S^{\ AlSi})$ $f_S^{\ III} = f_S^{\ AlCu} + (T^{AlCu}_{E,G} - T)/(T^{AlCu}_{E,G} - T_{sol})^{n3}\, (100 - f_S^{\ AlCu})$	f_s vs. temperature curve is modeled based on three segmented experimental cooling curve thermal events for the whole solidification range and varying SR. Agreement of modeled and experimental data R^2=0.99.
8	**NEWTONIAN HEAT BALANCE (NHB)** $f_S(T_C) = \frac{\int_{T_{Liq}}^{t} \left(\frac{dT_C}{dt} - \frac{dT_{CBL}}{dt} \right) dt}{\int_{T_{Liq}}^{T_{Sol}} \left(\frac{dT_C}{dt} - \frac{dT_{CBL}}{dt} \right) dt}$	f_s is calculated by determining the cumulative area between the dT_c/dt of the cooling curve, and the dT_{BL}/dt (BL). This methodology is utilized for ALTAP and UMSA measurements and post-processing f_s analysis.

The final model presented in Table 6, NHB, relies on information concerning the baseline, an example of which was shown in Figure 5 and which will be further explained in Section 2.4.4. Using these fraction solid models, a graph of the change in fraction solid versus temperature can be generated, such as the one in Figure 6 below.

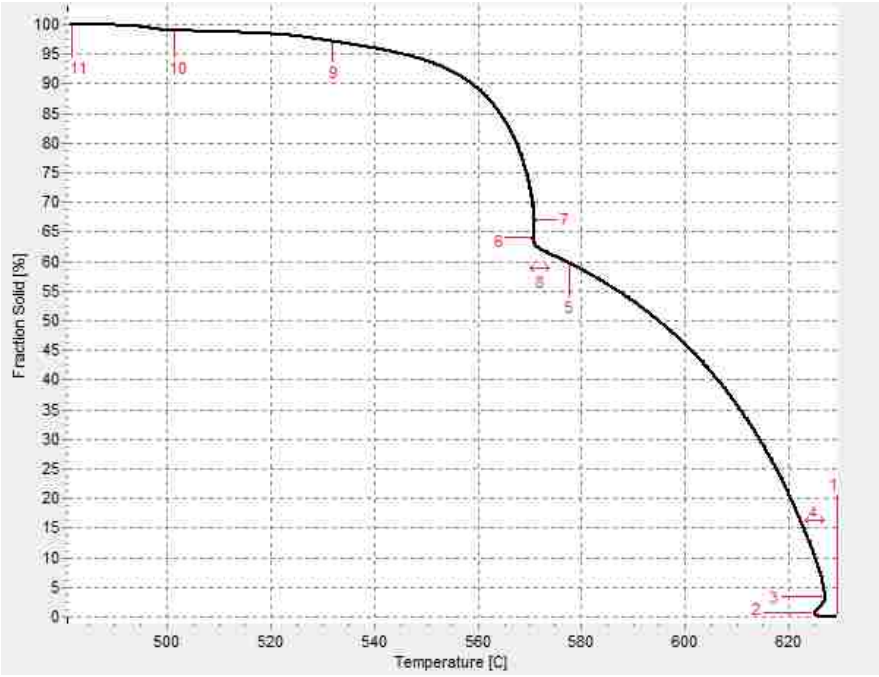

Figure 6 - Fraction solid curve of a nominal 5 wt.% Si and 1 wt.% Cu aluminum alloy.

The curve shown in Figure 6 was generated using the NHB model and the baseline information from Figure 5. Most major metallurgical events are still locatable in this curve.

Many effects of CR/SR on the solidification process parameters, including the potential effect of f_s at the Dendrite Coherency Point (DCP), are presented in the literature [23-31]. At the DCP, porosity, shrinkage and hot tearing start to develop. Earlier work at the University of Windsor proved that the f_s at the DCP is higher with an increased SR and thus prolongs mass feeding to a later point during the solidification process. This work showed that the thermal modification can be quantified using f_s curve parameters [32]. The in-situ thermal analysis of the complex cast component used to

assess riser feeding efficiency is compelling evidence about the comprehensive capabilities of this technique to assist in metal casting technology optimization [33].

Some direct and in-direct methodologies used for determination of the f_s evolution during solidification processes are summarized and evaluated in terms of the advantages and limitations specific to certain applications [23, 34-46]. The following most often utilized methods can be categorized as follows:

1 Thermal analysis techniques:
1.1 Differential Scanning Calorimetry (DSC) and Differential Thermal Analysis (DTA).
1.2 Computer Aided Cooling Curve Analysis (CA-CCA).
1.2.1 AlTAP Technology Platforms (i.e. environmental, in-situ, etc.).
1.2.2 UMSA Technology Platforms (i.e. vacuum, pressure, etc.).
2 Computational thermodynamic software packages for equilibrium and non-equilibrium solidification processes.
3 Quantitative metallography on microstructures quenched from the semi-solid state.
4 Ultrasonic monitoring by measurement of propagation speed of ultrasonic waves.
5 Measurement of electrical resistance/magnetic permeability.
6 Measurement of mechanical response by indentation, back extrusion, etc.
7 Measurement of electrical potential difference or uni-axial flow stress that mathematically relates the obtained values to fraction solid.

Please note that since the focus of this thesis is on CA-CCA f_s methodologies, only some of the above mentioned methods are expanded in more detail.

DSC and DTA have been used for the determination of f_s [32]. One of the limitations of these two techniques include the restriction to very small (mg range) test samples that are not fully representative of the cast component's structures. As-cast structures often exhibit macro-segregation of alloying and impurity elements and contain inclusions, gas and shrinkage pores as well as undesirable macroscopic constituents, etc. that affect measured thermal data. These effects are not fully understood and cannot be easily

quantified using DSC/DTA methodologies. DSC and DTA are, however, indispensable for the benchmarking of on-line industrial and laboratory thermal analysis data (i.e. Latent Heat of Fusion) of complex materials tested under 'ideal" conditions using CA-CCA methodologies.

The literature suggests a number of f_s models using equilibrium phase diagram data, which are summarized in Table 6, #1 – 3. These models are based on fundamental solidification data of simple alloy systems. Because of the highly complex nature of industrial alloys, processes and cast components, many questionable and simplified assumptions are made in these models (see comments in Table 6). Often these models yield f_s data for only some solidification events and are not fully representative of calibrated CA-CCA data (i.e. undercooling events). Using simplified models for applied engineering solutions can also often require time consuming iterative approaches (both theoretical and experimental) to account for the actual industrial environment processing conditions. For example, the Scheil equation has quite severe restrictions when applied to multi-component alloys and can be applied only to dendritic solidification [43]. It is critical for the understanding and quantification of industrial alloy phase transformations, processes and cast components properties that all solidification events are taken into account.

According to Saunders et al. [47] and Sołek et al. [48] utilization of thermodynamic modeling sufficiently limits the Scheil-Gulliver assumption and leads to "good results for much of the solidification range." FactSage, Thermo-Calc and JMatPro are three of the most powerful packages that use Scheil-Gulliver isothermal step modeling. The first two tested packages render good Latent Heat (LH) data for the non-equilibrium solidification process [31].

This thesis revealed that the LH calculated using statistical methods, Si_{EQ} methodology, FactSage, and Thermo-Calc renders a comparatively small average error. The Coefficient of Correlation (R^2) with the DSC data is significantly higher for the first two methods (R^2=0.97) vs. approx. 0.90 for the latter two. More in-depth work is needed to compare thermo-physical solidification characteristics assessed by the CA-CCA and modeling methodologies while considering all the parameters describing metallurgical

reactions that are relevant to the industrial environment. The use of the computational software packages is limited by the thermodynamic databases used in the calculations.

Highly competitive industries like transportation require rapid R&D tools for commercialization of proven materials, technologies and cast components. Therefore, further development and commercialization of the novel engineering tools (i.e. AlTAP and UMSA) capable of addressing industrial requirements is of utmost importance. The wide range of scientifically and industrially relevant technical capabilities of the UMSA and AlTAP, developed at the University of Windsor, make them very attractive engineering tools for determining various thermal characteristics including f_s [32, 33, 49].

The DSC method of Partial Areas (Table 6, #5) determines experimentally approximated f_s data, making the assumption that the heat of melting is independent of the temperature.

Methods of modeling non-equilibrium solidification processes of complex industrial alloy systems, shown in Table 6, #7-8, do not have the previously mentioned limitations and are based on experimental AlTAP and UMSA cooling curve data [50].

The literature also presents a quantitative metallography technique for determination of the volume fraction of phases formed prior to rapid quenching from mushy zone temperatures [45]. This technique requires the use of small test samples in order to preserve the structure present at a given temperature of interest. Both small test samples and rapid quenching rates minimize structural transformation(s) during this operation and thus maximize the accuracy of this measurement procedure. This technique is not suitable for on-line measurements. In addition, this technique is very time consuming because it requires high spatial resolution data in the given region of interest. A rapid quenching method presented by J. Wannasin et al. which takes into account the growth layers of the solid phase(s) allows for the actual pre-quenching f_s to be determined [46].

Four prominent f_s prediction models based on the experimental thermal analysis data can be used for f_s determination at any point during the solidification of the test sample or cast component. These are: the Su and Tsai model [34], the Fras et al. Fourier model [51], the Huang source/sink algorithm for modeling phase changes [36] and the W. T. Kierkus and J. H. Sokolowski Newtonian CA-CCA model [52, 53]. Unfortunately, the first three

methods have essential and important limitations. They require that at least one of the following be explicitly known:

a.) Accurate and detailed information regarding thermal properties of an alloy and mould material (as a function of temperature) and detailed knowledge of the heat transfer rate between the cast component and the mould,

b.) Knowledge of the heat transmission coefficient from the casting-mould system to the surroundings and recorded temperature history of the casting,

c.) Knowledge of the thermo-physical properties of the casting-mould-surroundings thermal system.

Due to the fact that the geometrical and thermal complexity of the casting-mold "system" (i.e. castings and mold material change their physical properties with temperature and time) this information is not directly available to the investigator, so in order to perform analysis, these properties must be assumed on an *a priori* basis. While it is possible to correct erroneous assumptions on a trial-and-error basis, the accuracy of these attempts has thus far been questionable. In addition, these analyses have been lengthy and computationally complex, which limits their use in practical industrial situations.

The first two methods require either accurate knowledge of the thermal properties of the cast alloy or the heat transmission coefficient from the casting to its surrounding while the third one uses both the recorded temperature of the casting and physical properties of the mold. However, the CA-CCA methodology developed at the University of Windsor is able to predict the f_s of the cast component section(s) in the semi-solid region by introducing the concept of a single function heat transmission coefficient based on the casting temperature, which is described in the next section.

2.4.4 Baseline

The baseline is a calculation that is very important when performing analyses of cooling curves. It may be defined as the hypothetical first derivative if no metallurgical reactions were to occur during the solidification of a metal [53]. This definition is also called the 'virtual baseline' in certain literature (reserving 'baseline' for only the regions where the thermal curve and baseline coincide) however 'baseline' is common in practice and will

is used in this thesis according to the earlier definition. A baseline may also be isothermal (in experiments where temperature is held constant) or dynamic (where temperature is changed through heating/cooling). Examples of potential baselines are shown in Figure 7. Please note that the curves shown are actually curve-fittings done to temperature/time curves extracted from DSC analysis (and not derivatives). The diagram is still, however, illustrative of the simple and qualitative means to determine the baseline found in the literature.

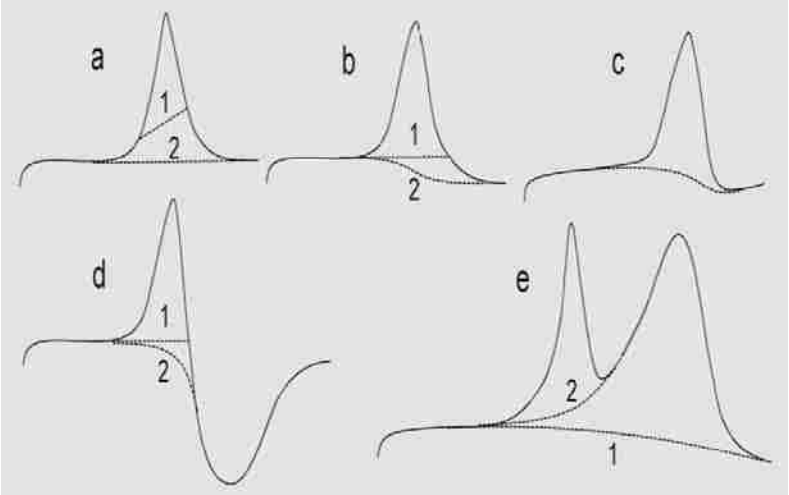

Figure 7 - Qualitative baselines for sample DSC thermal curves (endothermic reaction is upward) [54].

Figure 7 shows various thermal curves as well as baselines.

a) 1 does not follow naturally from the thermal curve. 2 has an almost asymptotic behaviour for both the rising and declining slopes and encompasses the peak well.
b) 1, again, does not quite capture the shape of the curve. 2 in this case is a better match, using either integrals or spline fitting.
c) A good fit, very similar to 2 in curve b).
d) Because of the apparent convolution of an endothermic and exothermic peak, it is hard to distinguish the contributions of each curve. Because of this, 1 may be a better fit for the endothermic peak than 2, which could be simply following the outside of the exothermic peak.

e) 2 is a good baseline for the left peak. This may aid in separation of the peak's LH contribution from the overall thermal curve. 1 is a good baseline for the thermal curve as a whole.

A variety of papers published over the past thirty-five years have presented many different techniques for experimentally determining the baseline equation for solidification processes. As in Figure 7, some of these methods have been based on arbitrarily applied assumptions and are subject to different interpretations. A summary of selected techniques and a comparison of results were presented by Barlow and Stefanescu [52]; Kierkus et al.[53]; E. Fras et al. [51] and Emadi et al. [55]. These authors reviewed three distinct approaches to the DBL calculation:

a) Newtonian analysis;
b) Fourier analysis;
c) Empirical analysis with the assumption of one or three different heat transfer coefficients.

A new baseline model, the Dynamic Baseline (DBL), was developed at the University of Windsor for the AlTAP cooling cycle and later adapted to the UMSA Technology Platform. The DBL concept presented in this study is based on the Newtonian model adopted by Stefanescu et al. [23, 44, 56] and other authors [4] for cooling curve analysis. The different paths taken to finalizing both AlTAP and UMSA DBL procedures is partially presented in [53].

In the past, users of Computer Aided Cooling Curve Analysis (CA-CCA) were able to obtain only limited information from the cooling curve and its first derivative. The primary reason was that the scientifically proven DBL curve was not available for the generation of reliable physical data comparable with other techniques including Differential Scanning Calorimetry (DSC).

The DBL equation calculation procedure presented in this study requires that the lumped thermal capacity system being considered (i.e. the metal/alloy test sample, the cup and the thermocouple) complies with Newtonian cooling model requirements. This means that the temperature within the system must be a function of time only and be spatially uniform, or at least that the temperature gradient in any direction within the

system must be negligible at any instant during the cooling/solidification process. These conditions are most closely satisfied when:

a) A thin-walled metal cup (including steel foil crucible for Al and Mg alloys) is used in conjunction with a low thermal inertia thermocouple in which only the tip is directly exposed to the melt. The shaft of the thermocouple is protected by a small diameter ceramic sheath. The small thermal mass of the cup and thermocouple is negligible in comparison with the test sample mass so the thermocouple can track the true temperature with minimal lag. This configuration limits the interference between the tested material, the cup and the thermocouple. The recorded cooling/heating curve thermal events are controlled by elimination of additional solidification front(s). This approach also allows for the unbiased analysis of the material's thermal data since the cup and thermocouple "heating and cooling" effects are negligible.
b) The cup is well insulated from both, the top and the bottom, for example, using low density ceramics. This secures the one-dimensional heat transfer mode. **Note:** Other carefully designed and verified test cups, thermocouples and experimental setups may also be sufficient for specific tasks. However, additional metallurgical factors may also have a considerable effect on the integrity of the cooling/heating curve analysis and must be considered. For example, an optimized melt sampling procedure will ensure unbiased test sample cleanliness (the type and level of gas and insoluble inclusions must be identical as in the furnace) but during the melting cycle the test sample must be protected in order to prevent oxidation and absorption of hydrogen.
c) The rate of cooling due to loss of energy from the cup to its surroundings should be limited by the Biot modulus (Bi) which is based on the thermal system's "characteristic dimension" and the "overall heat transmission coefficient." The value of Bi should not exceed 0.1.

Biot modulus is defined as:

$$\boldsymbol{Bi = VU / AK_{eff}} \qquad (1)$$

Where:

V - Volume of the cast sample (lumped system);

U - "Overall apparent heat transmission coefficient" between the cast test sample and its surroundings (lumped system) by all possible heat transfer modes (convection, conduction and radiation). ***U*** is a time dependent function;

A - Surface area of the cast test sample (lumped system);

K_{eff} - Thermal conductivity of the alloy.

The characteristic dimension can be defined as the ratio of the system volume to its outside surface area (i.e. the area of the system through which energy is lost to the surroundings). The overall heat transmission coefficient is based on the total thermal resistance between the temperature of the solidifying test sample (T_c) and the temperature of the surroundings (T_s, also sometimes defined as T_∞). The requirement of ***Bi*** < 0.1 will hold for the majority of metals, alloys, metal matrix composites and experimental conditions including physically simulating lost wax and foam processes, sand and semi-permanent casting processes and other casting technologies.

Finally, during the solidification process of the test sample, the "apparent sensible thermal capacitance" of the system should not be temperature dependent. Once again, this is typically the case for most metals, alloys and metal matrix composites. Under the assumptions described above, the energy balance can be written in the form shown in Equation 2.

$$\rho C_p V \frac{d(T_c - T_\infty)}{dt} = -AU(T_c - T_\infty) + \frac{dQ_L}{dt} \qquad (2)$$

Equation 2 can be rewritten as the first derivative of a cooling curve as a function of time (dT_c/dt):

$$\frac{dT_C}{dt} = -(\frac{AU}{\rho C_p V})(T_c - T_\infty) + \frac{1}{\rho C_p V}\frac{dQ_L}{dt} \quad (3)$$

Equation 3 can also be presented in the form of Equation 4:

$$\frac{dT_C}{dt} = \frac{1}{\rho C_p V}\left[\frac{dQ_L}{dt} - AU(T_c - T_\infty) \right] \quad (4)$$

Where:

- C_p - "Sensible apparent specific heat" (lumped system);
- ρC_p - "Apparent sensible thermal capacitance" per unit volume (lumped system) expressed as a product of the alloy density (ρ) and its specific heat;
- T_c - Temperature in the test sample centre;
- T_∞ - Temperature of the system surroundings, assumed to be constant and "known" for the experiment;
- t - Time;
- Q_L - The energy generation rate when sample/casting section changes its state from liquid to solid or vice versa (this quantity, also known as the latent heat, is positive during solidification and negative during the melting process).

The DBL equation is calculated using Equation 3 or Equation 4 as a portion of the first derivative of a cooling curve between liquidus ($T_{c,liq}$) and solidus ($T_{c,sol}$) temperatures assuming absence of any metallurgical reaction(s). This condition is satisfied under the conditions in Equation 5.

$$\mathbf{Q_L = 0}$$
$$\mathbf{T_c \geq T_{c,liq}\ @\ t = t_{c,liq}} \quad (5)$$
$$\mathbf{T_c \leq T_{c,sol}\ @\ t = t_{c,sol}}$$

If the conditions in Equation 5 are taken into consideration, Equation 3 and/or Equation 4 can be reduced to Equation 6, shown below.

$$\frac{dT_{cBL}}{dt} = (-\frac{AU}{\rho C_p V})(T_{CBL} - T_\infty) \quad (6)$$

Where:

$\boldsymbol{T_{cBL}}$ - Temperature of the DBL in the test sample centre.

The above energy balance for the DBL portion can also be written as a rearranged Equation 7 while accounting for the liquid and/or solid single phase formed during cooling of the test sample or cast component section.

$$\frac{1}{T_{cBL} - T_\infty}\frac{d(T_{cBL} - T_\infty)}{dt_{cBL}} = -(\frac{AU}{\rho C_p V}) \quad (7)$$

When solved, Equation 6 and the rewritten Equation 7 will determine the time dependent $\boldsymbol{T_c}$ before the solidification process has started and after it has been completed (as stated in Equation 4). Equation 6 and Equation 7 are representative for the single phase states of the solidification or melting process (i.e. liquid or solid, $\boldsymbol{Q_L} = 0$). On the right side of these Equations, only $\boldsymbol{U}$ (the overall heat transmission coefficient) is a time dependent function. The other variables grouped in the bracket on the right side are virtually constant or can be assumed to be constant without introducing significant error into the results. The right side of Equation 7 can be termed an "effective overall heat transmission coefficient" $\boldsymbol{U^*}$. Therefore, the measured $\boldsymbol{T_c}$, as a function of time, can exclusively define the $\boldsymbol{U(t)}$ for given experimental conditions by fitting a polynomial using the least square method to the left side of Equation 7. $\boldsymbol{T_\infty}$ is assumed to be a constant, 0, and can be eliminated from the equation.

It is commonly believed that the overall "apparent heat transmission coefficient" $\boldsymbol{U}$ cannot obey the same continuous function before and after solidification. However,

several experiments at the University of Windsor using both industrially pure metals (aluminum and tin) and 319.2 and 356 aluminum alloys have shown otherwise. Close inspection of Equation 6 and Equation 7 shows that only $\boldsymbol{U}$ is truly time dependent. In theory, the term $\boldsymbol{\rho C_p}$ also depends on temperature and therefore is a function of time but the variation is so small that it can be treated as a constant. $\boldsymbol{\rho C_p}$ term does not vary more than +/- 0.7% of its average value for aluminum alloys tested in the range of 800 and 400°C. Based on the measured $\boldsymbol{T_c}$, the numerically determined $\boldsymbol{dT_c/dt}$ and the $\boldsymbol{U(T_c)}$ function, $\boldsymbol{dT_{cBL}/dt}$ can be calculated if the right side of Equation 6 and/or Equation 7 is fit as a polynomial in terms of $\boldsymbol{T_c}$ by using the least square method, resulting in Equation 8.

$$\frac{dT_{CBL}}{dt} = \sum_{i=0}^{n} a_i (T_{cBL})^n \qquad (8)$$

In those cases where $\boldsymbol{\rho C_p}$ is slightly temperature dependent, over the analyzed range of temperatures, this dependence is incorporated into the constants of the fitted polynomial ($\boldsymbol{a_i}$).

Because $\boldsymbol{dT_{cBL}/dt}$ is a function of $\boldsymbol{T_c}$ only, the $\boldsymbol{U(T_c)}$ is valid for all parts of the cooling curve in the whole range of $\boldsymbol{T_c}$ measurements. Therefore, the values of $\boldsymbol{dT_c/dt}$ can be determined for all recorded values of $\boldsymbol{T_c}$, which form the DBL Equation 9 shown below.

$$\frac{dT_{cBL}}{dt} = F(T_{cBL}) \qquad (9)$$

Equation 9 is clearly a function of time because $\boldsymbol{T_c}$ is time dependent.

The CA-CCA methodology is able to predict the f_s of the cast component section(s) in the semi-solid region by introducing the concept of a single function heat transmission coefficient based on the casting temperature. In the case of the single phase (liquid or solid) cooling stages of the test sample or cast component, the energy balance equation is presented in Equation 2. Once the unique function of the multimode heat transmission

coefficient **U** is expressed in terms of measured temperature $\boldsymbol{T_c}$ and its derivative $\boldsymbol{dT_c / dt}$ (Equation 9), it is possible to express the $\boldsymbol{f_s}$ for any temperature between equilibrium and non-equilibrium $\boldsymbol{T_{Liq}}$ and $\boldsymbol{T_{Sol}}$. It should be noted that the DBL determination method described in Section 2.1 can also be used to create input for the methods described in [51] and [34].

2.5 Silicon Equivalency

One issue when dealing with multi-component aluminum alloys is the lack of accurate liquidus and solidus temperature information available when dealing with ternary or high-order phase diagrams. This difficulty can be addressed by using the system of 'Silicon Equivalency' or Si_{EQ} which is similar to the carbon equivalency method used for gray iron. In the Si_{EQ} method, the wt.% of alloying elements, other than silicon, are numerically converted to an 'equivalent' silicon value. 'Equivalent' in this case means that x wt.% of some element will have the same effect on the solidus/liquidus temperatures as y wt.% of silicon (where x and y are variables). Silicon was chosen as the base element for this method since it is common in all 3XX alloys. [57]

Si_{EQ} uses information from binary phase diagrams between Al and others elements (denoted ***Xi***). The slopes of the liquidus and solidus lines of Al-Xi phase diagrams can be expressed using second order polynomials. Equation 10 below contains an example polynomial for the liquidus line in the AlSi phase diagram (where 660.452°C is the melting point of pure aluminum).

$$T^{AlSi}_{LIQ} = 660.452 - 6.11 \cdot Si - 0.057 \cdot Si^2 \qquad [^oC] \qquad (10)$$

Using these polynomials as well as the melting temperature of pure aluminum, it is possible to develop relationships between the concentrations of Xi and the silicon equivalents, $\boldsymbol{Si^{Xi}_{EQ}}$ as shown below in Equation 11.

$$Si^{Xi}_{EQ} = a_0^{Xi} + b_0^{Xi} \cdot Xi + c_0^{Xi} \cdot Xi^2 \qquad [wt.\%] \qquad (11)$$

Where:

a_0^{Xi}, b_0^{Xi} and c_0^{Xi} are polynomial coefficients.

Xi is concentration of alloying element in wt.%.

Table 7 shows calculated polynomial coefficients for various common alloying elements.

Table 7 - Polynomial coefficients for binary Al-Xi alloys [58].

Al-Xi Alloy	a_o	b_o	c_o
Al-Cu	0	0.350	-0.027
Al-Mg	0	0.0258	-0.0088
Al-Mn	0	0.8221	-0.0349
Al-Fe	0	0.6495	0.0003
Al-Zn	0	0.1227	-0.0002
Al-Sn	0	0.7849	-0.0313
Al-Bi	0	0.9076	-0.0092
Al-Pb	0	0.859	0.02976
Al-Ca	0	0.0594	0.00685
Al-Sb	0	0.8255	-0.0327
Al-Ni	0	0.5644	-0.0285
Al-Sr	0	0.7854	-0.0157
Al-Ti	0	-0.8159	0.009927
Al-B	0	-0.9977	0.00007506

With the silicon equivalents for all component alloys calculated, the overall silicon equivalency value can be expressed using Equation 12 below.

$$Si_{EQ} = Si + \Sigma Si^{Xi}_{EQ} \quad [wt.\%] \quad (12)$$

This Si_{EQ} value can then be substituted into equations for characteristic temperatures, such as Equation 13 which is applicable for calculating liquidus temperatures up to the eutectic point.

$$T^{Al\text{-}Si\text{-}\Sigma i}_{LIQ} = 660.452 - 6.11 \cdot Si_{EQ} - 0.057 \cdot Si_{EQ}^2 \quad [^oC] \quad (13)$$

Equation 14 is an alternate equation which is applicable for calculating liquidus temperatures in the hypereutectic region.

$$T^{Al\text{-}Si\text{-}\Sigma i}_{LIQ} = 389.79 + 15.855 \cdot Si - 0.0561 \cdot Si^2 + 3.14 \cdot \Sigma Si^{Xi}_{EQ} + 0.057 \cdot \Sigma (Si^{Xi}_{EQ})^2 \qquad [^oC] \qquad (14)$$

2.6 Heat and Solution Treatment

Heat treating generally refers to any heating or cooling operations which are done with the intent of changing mechanical properties, metallurgical structure or the residual stress state of an alloy. For aluminum alloys, this is normally done to increase strength and hardness of precipitation-hardenable alloys. Certain alloys will not gain significant benefits from this process and are 'non-heat-treatable' and may rely instead on cold-working. Annealing, a heating process for decreasing strength and increasing ductility, may be applied to both treatable and non-treatable alloys. Certain binary alloy systems, such as AlSi or AlMn, will show little response in mechanical properties due to precipitation hardening. Systems such as AlCu or AlMgSi will yield higher changes (with strengthening from $CuAl_2$ and Mg_2Si respectively). Solution treatment of alloys involves heating alloys to a temperature just below the solidus point and holding for a certain period of time. This step is performed in order to maximize the amount of solute dissolved in the solid solution [9]. Figure 8 shows an example of the temperature ranges needed for various heat treatment operations for a AlCu binary alloy system [59].

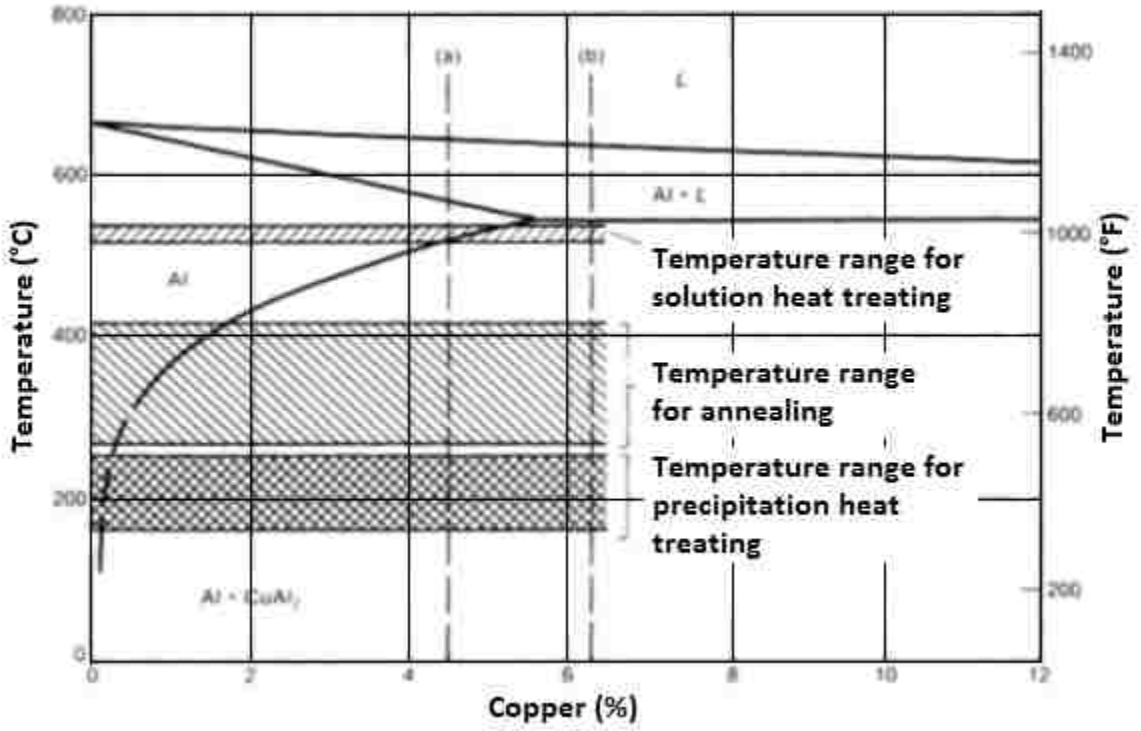

Figure 8 - Portion of a AlCu phase diagram with temperature ranges for heat treatments indicated [59].

A typical heat treatment for the A356.0 alloy cast in a sand mould would be a T6 (solution heat treatment plus aging) regimen; holding at 540°C for 12 hours followed by artificial aging at 155°C for 3-5 hours [59].

Heat treatment of magnesium alloys follows similar principles as those for aluminum. The mechanical properties of most magnesium casting alloys can be improved by heat treatment [59].

2.7 Quenching

After solution treatment, alloys may be quenched in order to keep solutes within the solid solution. As an alloy cools it goes through an intermediate temperature region of solute supersaturation and elevated diffusion rate where solute precipitation can occur. Sufficiently rapid cooling that minimizes the time spent in the intermediate region will preserve alloying elements in the matrix, leading to improvements in various mechanical properties, such as tensile strength, yield strength, ductility and fracture toughness [9].

Quenching can be performed with a variety of quenchants, ranging from air/gaseous cooling for lower rates to water/oil/liquid cooling for faster rates. Within the range of liquid coolants, water tends to provide the fastest rates and oil the slowest, with intermediate values achievable through the use of other substances (e.g. glycol).

Though higher cooling rates are desired for many casting applications, there are limitations for the rates that can be used. These stem not only from the capabilities of the quenchants and the means by which they are applied, but also the physical geometries of parts being quenched. Quenching parts with complex shapes and varying wall thicknesses can lead to internal stresses and distortions. Cooling within the semi-solid region can also cause feeding problems leading to shrinkage pores.

Fuoco et al. evaluated the effects that cooling rates have on the percentage porosity in strontium-modified and unmodified alloy 356. On samples cooled at different rates within the range 0.6°C/s - 6.7°C/s it was shown that the percentage porosity in the modified alloy can decrease from ~1.09 % to 0.13% (~0.36% to 0.06% in the unmodified alloy) [60].

2.7.1 Mechanisms of Quenching

The full exposure of a heated part to a quenchant contains at least three stages of heat transfer, which are shown in Figure 9. The magnitudes of time and cooling rate are similar and both use the same horizontal axis.

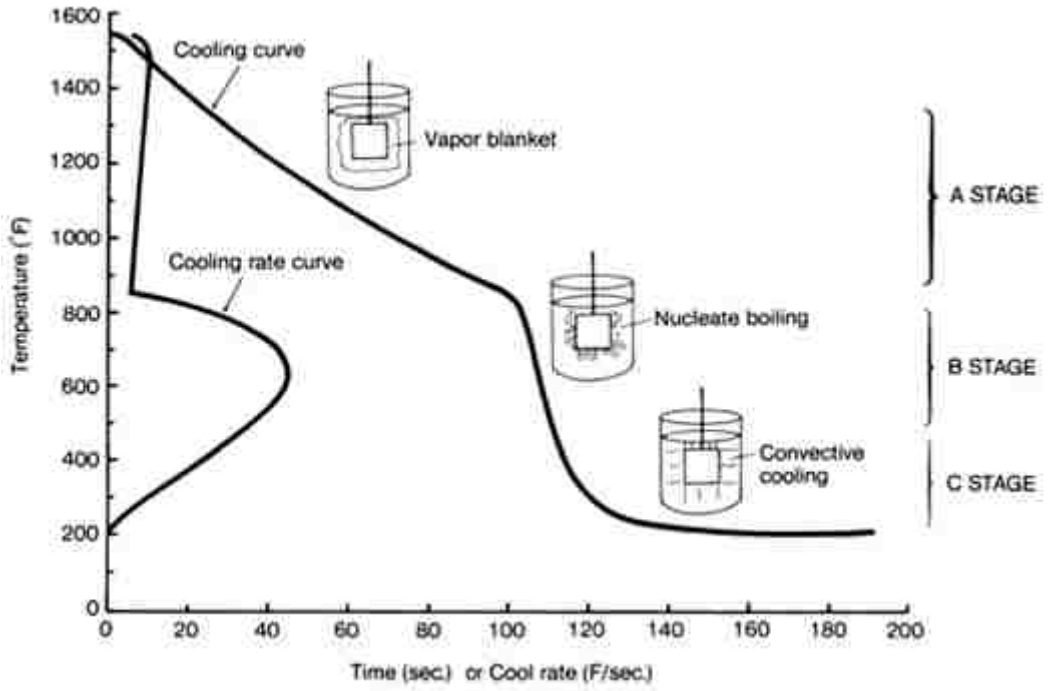

Figure 9 - Three stages of cooling mechanisms and their effect the cooling rate of a quenched material [61].

In Stage A, an unbroken vapor blanket is formed around the metal at first contact with the quenchant. It is formed because the supply of heat from the part surface exceeds the amount needed to produce the maximum vapor per unit area on the part. The blanket acts as an insulator, thus operating at a slow cooling rate, however heat transfer through radiation and conduction still occurs [62]. As the temperature of the part drops it can no longer sustain the vapor blanket and enters Stage B wherein the quenchant comes in direct contact with the part, resulting in violent boiling. This transition point is sometimes referred to as the leidenfrost temperature and is independent of the initial part temperature [61]. This stage has more rapid heat transfer because of the heat of vaporization. The morphology of the vapor bubbles has an effect on the duration and cooling rate during this stage. As the temperature of the part drops below the boiling point of the quenchant, it enters Stage C, a region of much slower cooling. In this stage there are no longer any complex vapor interactions between the part and the quenchant. Because of this, attributes of the quenchant such as temperature, agitation and viscosity are more influential in determining the cooling rate.

The effectiveness of a quenchant, particularly water, depends in large part on the relative velocity of the fluid and the part being quenched. In general, agitation will increase a quenchant's heat-removal capabilities. This is because the agitation breaks down the vapor blanket. The effectiveness of a quench is also dependent on the quenchant temperature and the two factors can interact in a variable way. In tests done on steel bars quenched with water, it was found that water at 32°C was five times as effective at quenching than 55°C with no agitation, three times as effective with flow rates at 15m/min, and twice as effective with flow rates at 30m/min [61].

The temperature of the quenchant is also important. Quenching using cold water can cause unacceptable distortion due to high thermal gradients induced upon cooling. However, hot water quenching can be insufficient to minimize distortion while at the same time maintaining design properties. "Delayed quenching" wherein a hot water quench is followed by a cold water quench is sometimes used. Polymer quenching, such as an aqueous poly (alkylene glycol)-PAG copolymer quenching medium, can be used in order to achieve optimal quenchant properties in cases where temperature variations can achieve desired properties [63].

2.7.2 Effects on Microstructure and Mechanical Properties

The microstructure of multicomponent alloys is normally dependent on the cooling rate. A common representation of the relationship between the cooling rate and transformations within the metal is in the form of a Time Temperature Transformation (TTT) diagram. Figure 10 shows an illustrative example of a TTT diagram for steel with sample cooling paths. The hardness values, given in HRC, are approximate based on 0.55% carbon steel.

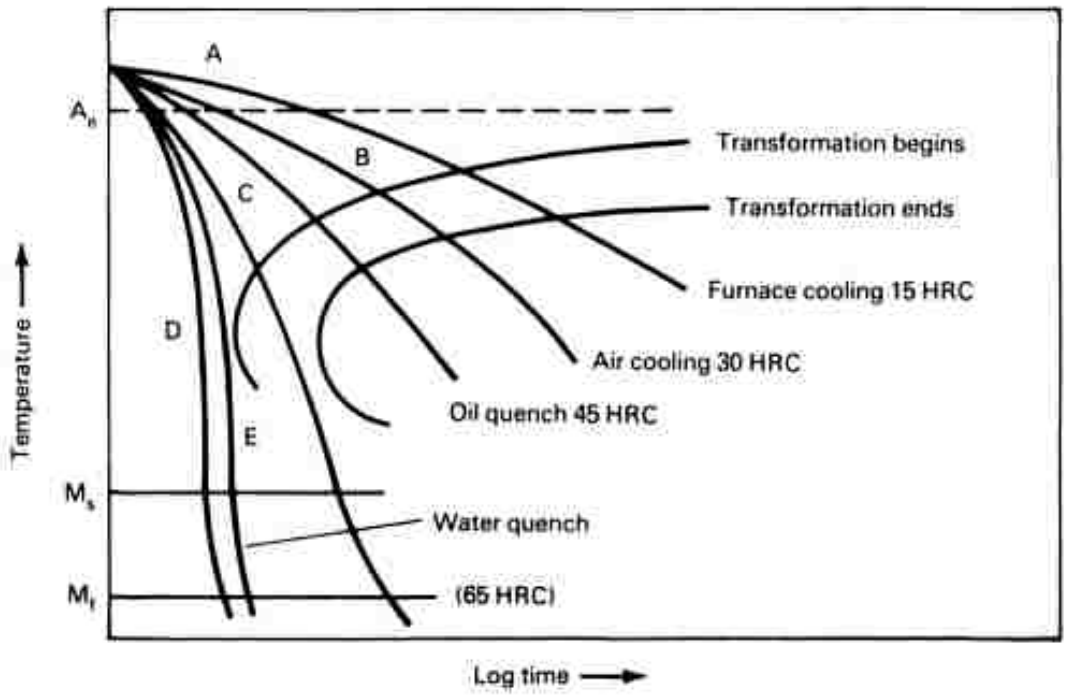

Figure 10 - Example of a steel TTT diagram with sample cooling paths [61].

In Figure 10, the two C-shaped curves as well as the two lines labeled M_s and M_f are bounds for regions of transformation (pearlite/bainite and martensite respectively). Path A begins transformation at high temperatures, producing thick, lamellar pearlite. Path B, begins transformation at lower temperatures and would have thinner pearlite. Path C, initially forms fine pearlite, but spends insufficient time in the upper region and will likely produce martensitic structures. Path D will produce a structure that is fully martensitic. Path E will produce a fully hardened martensitic structure, because it is at a critical cooling value. Were the path any slower, it would enter partial pearlitic transformation and reduce hardening [61]. TTT diagrams for aluminum alloys are also available however most focus on aging times with C-curves representing intermetallic precipitation.

Experiments by Zhang and Zheng on A356 elaborated on the dependence that the alloy's properties have on the cooling rate [64]. The team applied solution treatment (540°C, 14 hours) and various cooling rates, as well as artificial aging in a salt bath (170°C, 6 hours), to a series of samples. Variation in the cooling rates was achieved by

modifying the quenchant (water) temperature. The average cooling rate was measured between 450°C and 200°C, in accordance with previous work done by Livak, who identified this region as the most critical in modifying the strength [65]. The average cooling rates reached were: 250°C/s for 25°C water, 110°C/s for 60°C water, 20°C/s for 95°C water and 0.5°C/s for air cooling. It was shown that as the cooling rates decreases from 250°C/s to 0.5°C/s, there are logarithmic reductions in the UTS and YS of 27 and 33 percent respectively as well as reductions in the ductility.

Further to the previously mentioned work by Livak, it was discovered through experiments done on variants of aluminum alloy 6063 that most benefits to YS likely reaches an optimum at about 50°C/s. Copper appears to reduce the quench sensitivity while chromium increases it [65]. The quench sensitivity of A356 is higher than 6063 and it is believed that this is due to an excess of silicon.

2.7.3 Quench Factor Analysis

Studies into the effects of quenching on alloys have sometimes made use of Quench Factor Analysis (QFA). The goal is to find a single value that quantifies quench severity for a particular alloy based on cooling and Time Temperature Property (TTP) curves [66]. The first part of the process is calculating incremental quench factors, $\boldsymbol{\tau}$, for each time-step of the cooling process using Equation 15 and Equation 16.

$$\tau = \frac{\Delta t}{C_T} \tag{15}$$

Where:

$\boldsymbol{\tau}$ - incremental quench factor

$\Delta \boldsymbol{t}$ - time step used in cooling curve data acquisition

$$C_T = -K_1 K_2 \exp\left[\frac{K_3 K_4^2}{RT(K_4 - T)^2}\right] \exp\left[\frac{K_5}{RT}\right] \tag{16}$$

Where:

- C_T - critical time required to form a constant amount of a new phase or reduce the hardness by a specific amount at a particular temperature (1% transformation).
- K_1 - constant which equals the natural logarithm of the fraction untransformed during quenching (typically 99.5%: (ln (0.995)) = -0.00501.
- K_2 - constant related to the reciprocal of the number of nucleation sites.
- K_3 - constant related to the energy required to form a nucleus.
- K_4 - constant related to the solvus temperature.
- K_5 - constant related to the activation energy for diffusion.
- R - 8.3143 J/K mole.
- T - absolute temperature (K).

The K factors may be obtained through thermodynamic calculation as well as values published in literature however iterative adjustment of these values may be required in order to correlate to mechanical properties [67]. The final cumulative quench factor, Q, is the summation of all the incremental quench factors over the range [T_2, T_1] as shown in Equation 17. This range is the upper and lower limits which are the upper and lower limits of a TTP curve (much like the C-shaped curves from Figure 10).

$$Q = \sum_{T_1}^{T_2} \tau \qquad (17)$$

The quench factor is proportional to the heat removal characteristics of the quenchant and can classify the severity of a quench for a particular alloy. The cooling rate is inversely proportional to the Q value [66]. Although the quench factor is a potentially useful tool for comparison, its use is limited because of the amount of information (the K constants) required in its calculation, something which is not always available.

Chapter 3 Experimental Methods

3.1 Universal Metallurgical Simulator and Analyzer Technology Platform

The Universal Metallurgical Simulator and Analyzer Technology Platform (UMSA) (Canadian Patent No: 2,470,127, US Patent No: 7,354,491) is a thermal analysis platform developed jointly by researchers at the University of Windsor and the Silesian University of Technology in Gliwice, Poland. It is a custom-designed, desktop technology platform for physical simulations of metallurgical processes and advanced thermal analysis of metal casting and heat treatment operations. UMSA is utilized for both development and characterization of new and improved materials, cast components and their technological processes.

Figure 11 - Photograph of the UMSA Technology Platform (power supply and environmental chamber).

3.1.1 Hardware Platform

The UMSA is a complex system of several interlinked components, including:

a) Environmental chamber

The primary component of the UMSA (pictured on the right in Figure 11) is the main stage for experimentation. Samples are placed within the integrated heating/cooling coil and heated using induction. A bell jar (not pictured) placed over the stage provides the capability to alter test environments, including other

gases (argon, nitrogen, etc.) or even a vacuum (via an external pump). Quenching can be performed using either the cooling coil (gases blown on the exterior of the sample) or using a variety of newly developed quenching accessories.

b) Power supply

The UMSA is powered by a 1 kW power supply with options for altering the output amperage and frequency.

c) Data acquisition unit

The data acquisition unit is a 16-bit system capable of logging temperature/time measurements on two channels simultaneously and has a scan rate of up to 100Hz per channel. The components in the unit are as follows:

a. SCXI-1000DC 4-Slot Chassis, DC-Powered.
b. SCXI-1383 Power Supply.
c. SCXI-1125, 8 Channels Programmable Isolated Input Module.
d. SCXI-1328 High-Accuracy Isothermal Terminal Block.
e. SHC68-68-EPM Noise Rejecting Shielded Cable, 2m.

All parts were purchased from National Instruments (NI).

d) Desktop computer

The computer is used for user control as well as data logging and analysis. It is an off-the-shelf Pentium 4 computer running Windows XP Home 32-bit with an added PCI card to interface with the data acquisition unit. The card is an NI PCI-6281 (16 Analog Inputs, 24 Digital I/O, two Analog Outputs) and NIDAQmx driver software is also used.

3.1.2 Software Platform

The software components of the UMSA consist primarily of:

a) Two front-end programs, UMSA-TAI and UMSA-CA, which were designed for use with the UMSA and handle all end-user thermal analysis operations. These programs, described in detail later in this section, were written in C++ by the developers of the hardware system.

b) Back-end drivers and software to interface with the data acquisition system. These are largely standard software provided with the purchase of NI equipment.

UMSA-CA is used for control and data logging during experiments conducted on the UMSA platform. It accepts user input in the form of power settings, temperature settings, heat treatment paths, etc. and regulates the power supply accordingly. If cooling is required (and enabled) it may also release gas coolants via the integrated cooling coil.

UMSA-TAI is post-processing software used to analyze data logged by UMSA-CA. Using the temperature/time data as input, the program is capable of efficiently calculating information of metallurgical importance, including derivatives, baselines and fraction solid curves. The program is well-suited to the visualization and comparison of multiple graphs and also has curve smoothing capabilities (following the Savitzky-Golay algorithm). The data is also easily exportable to any standard spreadsheet program for further analysis.

3.1.3 Rapid Quenching Accessories

Recent developments of the UMSA platform have focused on creating accessories which allow for improved solidification rates within test samples. The default cooling component, the integrated cooling coil, can only cool samples to a limited degree which, depending on coolant and sample geometry, is usually around 10°C/s peak cooling rate for a solid sample. In order to improve on these rates, a move was made to using hollow samples, whose relatively thin walls would allow for faster solidification rates while still being large enough to allow for metallographic and mechanical testing. During melting, the inner walls are held in place by a thin-walled tube which can also be used as a channel for gaseous and liquid quenching media (heretofore referred to as the ‘centre tube’).

This new configuration was subjected to a wide range of trials. While prototype equipment is not the focus of this thesis, some options included using atomized water sprays, ventilation columns with slitted openings, cycling low melting point alloys and others. The best results were found to lie in simply directing a flow of pressurized liquid through the central tube. The liquid used most often for testing is water, used for its low cost as well as low viscosity.

3.2 Materials, Testing and Calibration

3.2.1 Test Sample Chemistry

Data used in this investigation was gathered from experiments conducted on a variety of alloys. These alloys are described below.

Aluminum - 356

Certain properties of A356 have already been outlined in the literature review in Sections 2.1 and 2.1.1. The alloy used for experimentation is nominally the same alloy. The liquidus and solidus temperatures are approximately 615°C and 555°C [1].

Aluminum - Al-20% Si with Strontium Modification (Al20SiSr)

This alloy is used by the Yamaha Motor Co. Ltd. who uses it for the production of linerless, monolithic cylinder blocks [5, 68]. The nominal composition of this alloy as provided by Yamaha in the form of ingots is shown in Table 8 below.

Table 8 - Chemical composition of the Yamaha hypereutectic Al-20wt.% Si alloy.

Al	Si	Cu	Fe	Mg
Balance	20.0	3.0	0.5	0.5
Mn	**Zn**	**Ni**	**P**	**Ti**
0.1	0.1	0.1	0.01	0.001

In order to add strontium to the above composition, pieces of the ingot were remelted with additions of strontium in the form of Al-10% Sr master alloy. The nominal composition desired was about 1000 ppm or 0.1 wt%. This significantly exceeds the levels normally added in industry, which are around 100 ppm.

The approximate liquidus temperature of the modified alloy can be calculated using the Si_{EQ} method, as shown in Table 9. In the Table, the first two rows contain the Si_{EQ} coefficients and the final row contains the individual contributions to Si_{EQ} for a total of 21.37 wt.% Si_{EQ}. The contribution of phosphorous is omitted from this calculation because a) the binary phase diagram for AlP is highly irregular and is not well suited to

the Si_{EQ} algorithm and b) at the present concentrations, phosphorus has a negligible contribution.

Table 9 - Silicon equivalency calculation for the modified hypereutectic alloy.

b	1	0.35	0.6495	0.0258	0.8221	0.1227	0.5644	0.7854	-0.8159	
c	0	-0.027	0.0003	-0.0088	-0.0349	-0.0002	-0.0285	-0.0157	0.009927	
El.	**Si**	**Cu**	**Fe**	**Mg**	**Mn**	**Zn**	**Ni**	**Sr**	**Ti**	**Si_{EQ}**
wt. %	20	3	0.5	0.5	0.1	0.1	0.1	0.1	0.001	21.37
	20	0.807	0.32483	0.0107	0.08186	0.01227	0.05616	0.07838	-0.0008	

Using the Si_{EQ} value determined above, the liquidus temperature is calculated using Equation 14 in Section 2.5:

$$T^{Al\text{-}Si\text{-}\Sigma i}_{LIQ} = 389.79 + 15.855 \cdot (20) - 0.0561 \cdot (20)^2 + 3.14 \cdot (1.37) + 0.057 \cdot (0.773)$$
$$= 688.8°C$$

This value compares well to the value of 691 ± 2.2°C determined by Yamagata et. al for the unmodified hypereutectic alloy [69]. The solidus temperature determined in the same paper was 479 ± 3.3°C.

Magnesium - AM60B

Magnesium samples were provided by Meridian Lightweight Technologies Inc. along with nominal compositions used in production. The nominal composition for AM60B is shown in Table 10 below.

Table 10 - Nominal composition of AM60B alloy.

Mg	Al	Si	Mn	Fe+Cr+Ni
93.16	6.26	0.27	0.38	0.02

Magnesium - AE44

Nominal compositions for rare earth alloys do not always list individual rare earth contributions. This prompted SEM-EDX analysis which resulted in the composition seen in Table 11.

Table 11 - Experimentally determined chemical composition of AE44 alloy.

	Mg	Al	Ce	La	Other RE	Tot. RE
Start	90.14	2.82	2.82	1.21	1.76	5.80
Centre	88.64	2.76	2.86	1.36	2.54	6.75
End	87.97	2.94	2.88	1.44	2.37	6.69

Because solidification introduces a gradient in the constituents, the chemical compositions change slightly with respect to their positions with the sample. The values in Table 11 were determined using a sample solidified with a peak cooling rate of 240°C/s in three different regions: Start (near the inner wall of a hollow sample), Centre and End (near the outer wall).

Magnesium - Pure

Pure magnesium was processed in order to have calibration values for certain calculations. The sample used was made from industrial-grade purity stock.

3.2.2 Sample and Consumables Preparation

Samples used in experiments were machined at the University of Windsor's Technical Support Centre (TSC) in order to meet the dimensions required by the UMSA. The source material was in the form of ingots and/or bar stock provided by various casting facilities along with information regarding chemical composition. In the case of Al-20% Si alloy which required strontium modification, pieces of ingot were remelted in MCPT labs along with additions of master alloy (described in Section 3.2.1 - Test Sample Chemistry) and recast as bar stock. The dimensions for samples used are shown in Table 12 below.

Table 12 - UMSA test sample dimensions.

UMSA Sample (Solid)	18 mm (OD) x 22 mm (height) Weight: ~5.7g (AE44)
UMSA Sample (Hollow)	18 mm (OD) x 10mm (ID) x 26mm (height) Weight: ~12.2g (A356)

Crucibles to contain the UMSA samples are made from thin stainless steel foil of thickness 0.0254mm (0.001”) and end caps in order to minimize thermal mass which would affect thermal traces. Both foil and samples are coated in colloidal graphite paste in order to minimize reactions with the environment. Due to its reactive nature, magnesium samples were processed under an inert, argon atmosphere. The inner tube for hollow UMSA samples is made of Type 304 stainless steel, with a wall thickness of 0.254mm (0.01”).

Figure 12 - End caps and centre tube for UMSA sample isolation.

3.2.3 Experimental Setup (Hardware and Software)

Figure 13 shows the experimental setup used for compressed gas tests on hollow samples. The marked items are as follows:

a) The integrated heating/cooling induction coil.

b) The thermocouple inserted in the wall of the hollow sample, through the end caps.

c) The centre tube through which quenchants flow. The tiny holes visible are outlets.

d) Inlet tube for gaseous quenchants.

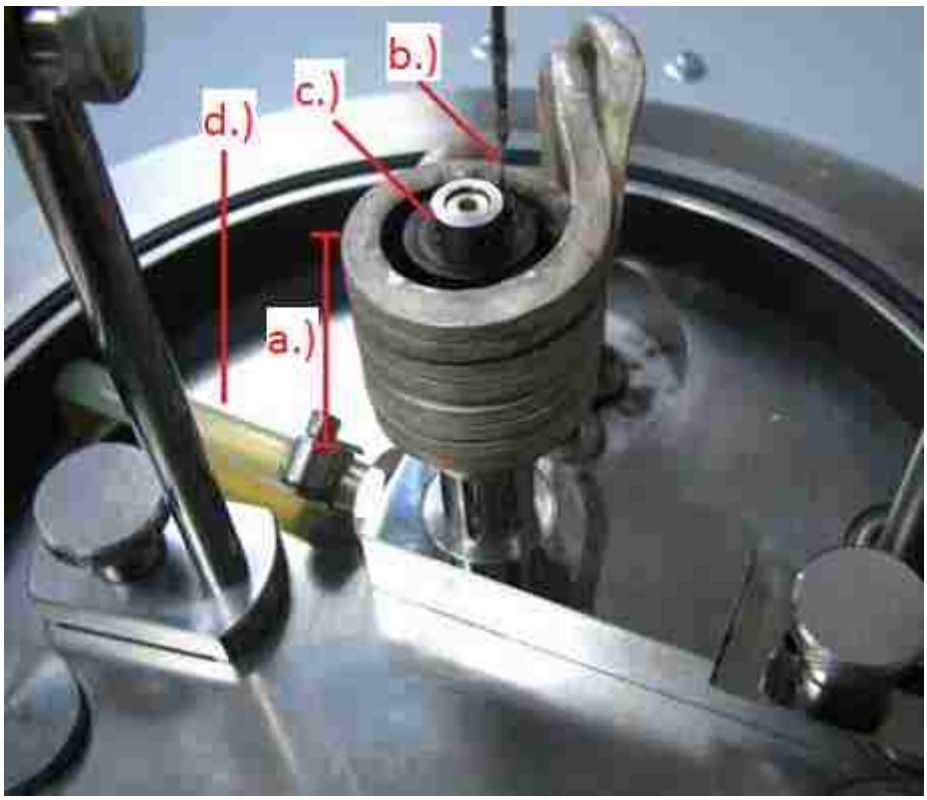

Figure 13 - Experimental setup for a hollow sample using compressed Ar cooling.

Figure 14 shows the experimental setup for a water cooling test. The top of the sample is now an inlet for water which passes through the centre of the sample (using a stainless steel tube as a buffer). The inlet port in the compressed gas setup now serves as an outlet port for exiting water.

Figure 14 - UMSA configuration for rapid liquid quenching.

3.2.4 Metallographic Sample Preparation

Aluminum samples were prepared in-house in the University of Windsor's Engineering Department. Tested samples were cut using a band saw along the longitudinal axis. This not only makes it easier to remove the centre tube, it also allows for viewing of the gradient of microstructure both in the longitudinal and radial directions. Samples were then mounted in blue epoxy. Samples are polished by hand using a progression of sandpaper, from 240 to 2500 grit, and finally on a polishing cloth. Water was used as the lubricant for the grinding stages, 1 micron alumina for polishing and final cleaning with ethyl alcohol (95%).

Magnesium samples are inherently more difficult to process because of the tendency to oxidize in the presence of moisture. These samples were sent to be processed by Dr. Carsten Blawert of GKSS Forschungszentrum Geesthacht GmbH in Germany. The

process involved automatic grinding followed by water-free polishing using OPS colloidal silica. This was followed by a two-stage etching process; a longer treatment in ‘soft’ etchant followed by a shorter dip in ‘standard’ etchant. The ‘standard’ etchant in this case was a mixture of water, acetic acid, ethanol and picric acid. The ‘soft’ etchant was comprised of water, acetic acid, ethanol, picric acid, ethylene glycol and nitric acid.

3.2.5 Light Optical and Scanning Electron Microscopy (LOM/SEM) Analysis

The majority of LOM observations were made using a Leica Q5501W microscope combined with a desktop computer and associated Leica QWin software. The microscope has six objective lenses (1.6x, 5x, 10x, 20x, 50x and 100x) which are in series with a 10x lens, resulting in a maximum of 1000x magnification. The imaging system was calibrated prior to testing to obtain accurate pixel:micron ratios.

3.2.6 Thermocouple Calibration

The thermocouple used for experimentation is a type K, chromel-alumel thermocouple produced by OMEGA with a 304 stainless steel sheath. The model used is KMQSS-020U-6 corresponding to a 6” probe with 0.020” (0.508mm) diameter. The model is ungrounded, due to EMF interference that may be introduced from the induction coil. The thermocouple is rated for -200°C to 1250°C with standard limits of error of 2.2°C or 0.75%. The data acquisition rates used for experiments is at least 100 Hz. There are no strict guidelines for acquisition rate as the requirements vary with probe size, cooling rate and other factors. Tests done on Iconel 600 probes with type-K thermocouples have shown that 5 Hz is sufficient to obtain thermal curves without loss of detail at rates of 120˚C/s [61].

In order to have accurate and reproducible results, it is important to assess the capabilities of the thermocouples. The two main parameters of interest are the accuracy of the temperature readings as well as the response time. The latter is of particular interest because the experiments deal with particularly high cooling rates and it is important to justify that the thermocouples are able to produce an adequate response at these rates. The response time of a thermocouple is defined as a function of a time constant. The time constant of a thermocouple is the time required to reach 63.2% of a step change in

temperature under specified conditions, such as the thermal conductivity of the medium being measured [70]. Five time constants are needed in order to reach the full 100% step change value.

Figure 15 below shows a graph of thermocouple response time in water provided by Omega. The diameter of ungrounded thermocouple used, 0.020", is beyond the lower bound of the data but the response time could be reasonably estimated as being about 0.25s. Other sources indicate values of less than 0.13s [71]. This is significantly better than the time response in air, which the same Omega source shows as being approximately 1.35s.

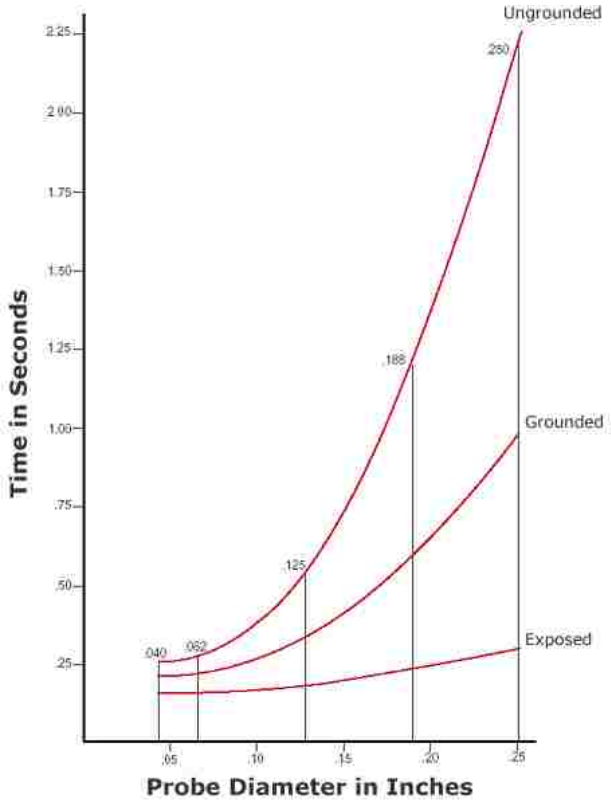

Figure 15 - Metal-sheathed thermocouple probe response time in water [70].

In addition to the thermocouple diameter it is also important to consider the effects of thermal conductivity on the response time of a thermocouple. Some sample thermal conductivities are provided in Table 13. The thermal conductivities of both the thermocouple junction as well as the surrounding medium are important [72]. Marr et al.

have shown that significant response gains can be found by switching to a copper junction [73]. Though the thermal conductivity of the surrounding medium is important (as seen in the differences between air and water data) published data on the response times of thermocouples in molten metals are unfortunately not widely available. Though the response times are expected to be lower, the exact degree of improvement is uncertain.

Table 13 - Thermal conductivities of certain materials [74].

	Thermal Conductivity (k, w/(m·K)) at Specific Temperatures		
Material	**25°C**	**125°C**	**225°C**
Air	0.024		
Aluminum	250	255	250
Copper	401	400	398
Graphite [75]	~130		
Iron	80	68	60
Magnesium	156		
Oil (SAE 50)	0.15		
Quartz (mineral)	3		
Silver	429		
Stainless Steel	16	17	19
Water	0.58		
Water Vapour		0.016	

Much of the literature investigating quenchants describe experiments using specially constructed quench probes. These systems normally consist of three main body elements; a connecting rod, a coupling and a probe tip, which are fused together. The coupling and rod are hollow in order to accommodate a thermocouple which is embedded directly into the probe. A diagram of such a system is shown in Figure 16. These probes are generally heated and then directly inserted into a quenchant. Probes can come in various shapes and have been made with a variety of materials, including alloy and stainless steels, silver, nickel, copper, gold and aluminum. The high thermal conductivity of silver has led to a number of designs, including a Japanese Industrial Standard (JIS) probe. This probe, developed by Tagaya and Tamura, has not gained mass acceptance in Western industry for a number of reasons, including: the cost of silver, surface tarnishing and a thermal

conductivity that is simply too different from steel. All probes in general require a good surface finish for reproducible results [61].

Liscic developed a steel probe using a proprietary surface temperature measurement system. Importantly, it is a thermocouple-based system capable of a response time of 10^{-5} s which is more than sufficient for logging temperature changes at cooling rates on the order of 10^{2}°C/s.

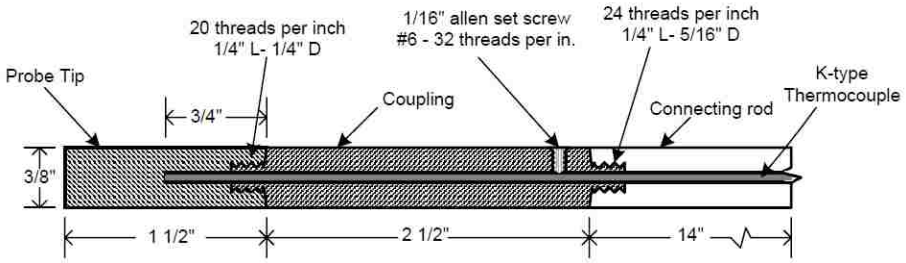

Figure 16 - CHTE probe-coupling-connecting rod assembly [76].

In experiments done by Maniruzzaman et al. [76], AISI 4140 probes (CHTE[4] probes, depicted in Figure 16) were quenched using mineral oils. The experimental setup consisted of a probe held vertically in a furnace and pneumatically pushed into a bath once heated to a specific temperature. Contact between the thermocouple tip and the quench probe is achieved using graphite powder. The peak cooling rate achieved in these experiments was 208°C/s.

The experiments performed in this report share certain characteristics with these quench probe experiments, however differ in the key respect that the samples in this report are being melted. This precludes the possibility of (safely) immersing them in a quenchant and requires a significant change in geometry in order to use liquid quenchants. A diagram of comparisons between a half-cross-section of a hollow UMSA sample and a quench probe is shown in Figure 17. It is quite similar to the CHTE probe, using the same thermocouple and graphite coating, however:

[4] Center for Heat Treating Excellence, Worcester Polytechnic Institute, Worcester, MA, USA.

a) Instead of a quench probe radially cooled from the outside when immersed in a bath, the UMSA cross-section is cooled in one directionally from the interior wall.

b) There is an intermediate layer (dark grey) of steel surrounding the UMSA sample (light grey) whereas the probe is uniform throughout.

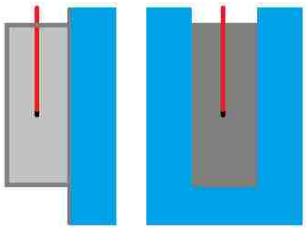

Figure 17 - Approximate comparison of cross-section between UMSA sample (left) and quench probe (right).

The level of cooling provided by the exterior surfaces of the UMSA samples by contact with air can be considered negligible compared to that of the flowing quenchant. Therefore, the temperature changes experienced at the thermocouple can be assumed to come primarily from the effects of the quenchant.

The primary purpose of this section is to justify the use of the thermocouples for rapid cooling applications in this thesis. Based on prior quench probe experiments in the literature which are performed at similar rates (~200°C/s peak) and with materials at significantly lower thermal conductivities, it is reasonable that the thermocouple setup used in this thesis provides sufficiently accurate representation of the temperature changes during solidification.

3.3 Experimental Design

Table 14 provides a summary of the samples and testing conditions used during experimentation. Each sample is processed three times under the same conditions in order to show repeatability. A total of 54 tests were performed.

Table 14 - Matrix of UMSA tests.

Alloy	Sample Code	Process Detail
Al20SiSr	AL1	Natural cooling/No added cooling
Al20SiSr	AL2	Centre tube cooling
Al20SiSr	AL3	Water cooling
Al20SiSr	AL4	Water cooling
Al20SiSr	AL5	Water cooling plus Solution Treatment (Short)
Al20SiSr	AL6	Water cooling plus Solution Treatment (Long)
A356	AL7	Natural cooling/No added cooling
A356	AL8	Centre tube cooling
A356	AL9	Water cooling
AM60B	MG1	Natural cooling/No added cooling
AM60B	MG2	Central tube cooling
AM60B	MG3	Water with glycol cooling
AM60B	MG4	Water cooling
AE44	MG5	Natural cooling/No added cooling (Solid sample)
AE44	MG6	Central tube cooling
AE44	MG7	Water with glycol cooling
AE44	MG8	Water with glycol cooling
Pure Mg	MG9	Natural cooling (Solid sample)

Chapter 4 Results and Discussion

4.1 Overall Summary of Tests Performed

In order to report the thermal data observed it is necessary to define the calculation of the average cooling rate. The range for calculating the average follows a convention set by Yamagata et al. which uses a range between 730°C and 380°C for their hypereutectic alloy. This convention is followed for ease of comparison between the present results and the literature findings [68]. The motivation behind this particular range is because the temperatures correspond to the events during high pressure die casting operations, namely the melt injection temperature (730°C) and the casting removal temperature (380°C). Using the range [730°C, 380°C] would not make much sense when applied to other alloys because these values are relative to individual liquidus and solidus points, which for the hypereutectic alloy are ~[690°C, 480°C]. Instead, the ranges for other alloys are based on the amount of superheat and undercool data used by Yamagata, i.e. [liquidus + 40°C, solidus - 100°C], which would more likely correspond to the real-life die casting ranges used for these alloys. A listing of these average ranges is found in Table 15. The actual calculation used to get the average rate is simply dividing the average range by the length of time it took to get from the upper to lower points.

Table 15 - Temperature ranges for average cooling rate calculation.

Metal/Alloy	Range of Semi-solid Region (°C) [Liquidus, Solidus, Difference]	Range for Average (°C) [Upper, Lower, Difference]
Al20SiSr	[689, 479, 210]	[730, 380, 350]
A356	[615, 555, 60]	[655, 455, 200]
AM60B	[615, 420, 195]	[655, 320, 335]
AE44	[620, 572, 48]	[660, 472, 188]
Pure Mg	[649, 649, 0]	[689, 549, 140]

Note: The listed rates are averages calculated for the final trial for each sample and NOT the average cooling rate from several trials. Data from earlier trials is generally omitted from analysis in order to allay concerns of proper contact between the thermocouple and the sample.

Table 16 is a summary of the tests performed, their processing conditions, as well as their cooling rates. Both peak cooling rates (maximum instantaneous cooling rate) as well as average cooling rates are listed. **Note:** The listed rates are averages calculated for the final trial for each sample and NOT the average cooling rate from several trials. Data from earlier trials is generally omitted from analysis in order to allay concerns of proper contact between the thermocouple and the sample.

Table 16 - Summary of cooling rates of UMSA tests.

Alloy	Sample Code	Peak Rate (°C/s)	Average Rate (°C/s)
Al20SiSr	AL1	5.7	1.2
Al20SiSr	AL2	13.1	4.1
Al20SiSr	AL3	263.9	79.0
Al20SiSr	AL4	360.4	37.6
Al20SiSr	AL5	340.9	32.1
Al20SiSr	AL6	N/A[5]	N/A
A356	AL7	5.8	1.1
A356	AL8	16.0	4.2
A356	AL9	127.1	22.5
AM60B	MG1	4.7	1.9
AM60B	MG2	17.7	9.7
AM60B	MG3	126.6	71.4
AM60B	MG4	283.4	146.3
AE44	MG5	3.5	0.9
AE44	MG6	21.8	10.3
AE44	MG7	192.5	58.8
AE44	MG8	521.2	156.7
Pure Mg	MG9	3.0	0.9

The cooling rates of samples cooled slowly are generally in a tight range. Natural cooling will solidify a hollow sample at a peak rate about 4-5°C/s (3-4°C/s for solid) and an average rate of 1-2°C/s. Centre tube cooling will cool an aluminum sample at a peak rate of 13-16°C/s (4°C/s average) and magnesium samples at 18-22°C/s (10°C/s average). The rates for water/glycol flow do not appear to have a consistent relationship between peak rate and average rate. In the case of the hypereutectic alloy, there is a clear

[5] The solution treatment performed on this sample was designed to interrupt the cooling process so a cooling rate is not applicable for this test.

discrepancy in for the relationships between peak rate and average rate for AL3, AL4 and AL5. However this is due largely because the alloys exhibits an unusually large amount of undercooling which is likely due to the presence of strontium. For the remaining alloys, which do not display significant undercooling, it may simply be that the methods of calculating peak (selecting the highest instantaneous rate throughout the entire trial) and average (calculating based on alloy-specific ranges) do not lend themselves well to comparison at very high rates.

Different trials of the same sample will generally have similar thermal curves, which give the appearance of the curves appearing in pairs (see Figure 41 for a good example of this). Though samples are processed several times (normally three) in order to verify repeatability of the thermal curves, only the final thermal curve can be considered representative of the final, analyzed microstructure. Many graphs will still show the earlier thermal curves for comparison and the trial number is indicated in the legends. For example, AL1-2 would denote trial 2 of sample AL1 (air cooling).

Figure 18 below shows a diagram of an UMSA sample after mounting and polishing. It appears as two samples however it is a hollow sample cut in half with the two walls showing.

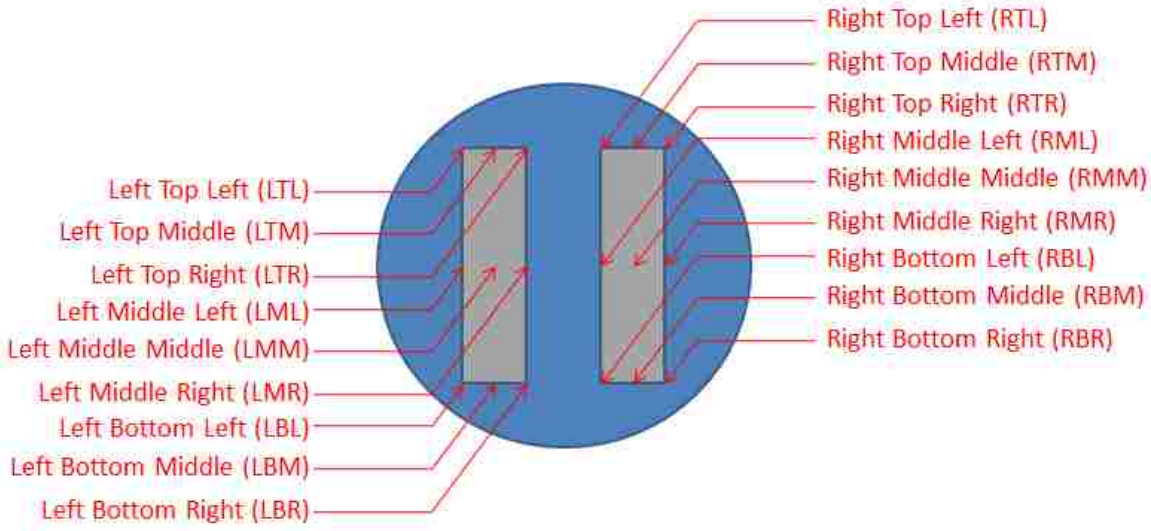

Figure 18 - Points of interest on a mounted hollow sample and location codes.

4.2 Characterization of Al20SiSr at Low Cooling Rates

4.2.1 Cooling Curves

Figure 19 shows derivatives of thermal curves from three trials performed on the same hypereutectic sample with no added cooling. The traces match quite well, with identical peak placement as well as great similarity between the paths outside of the semi-solid region.

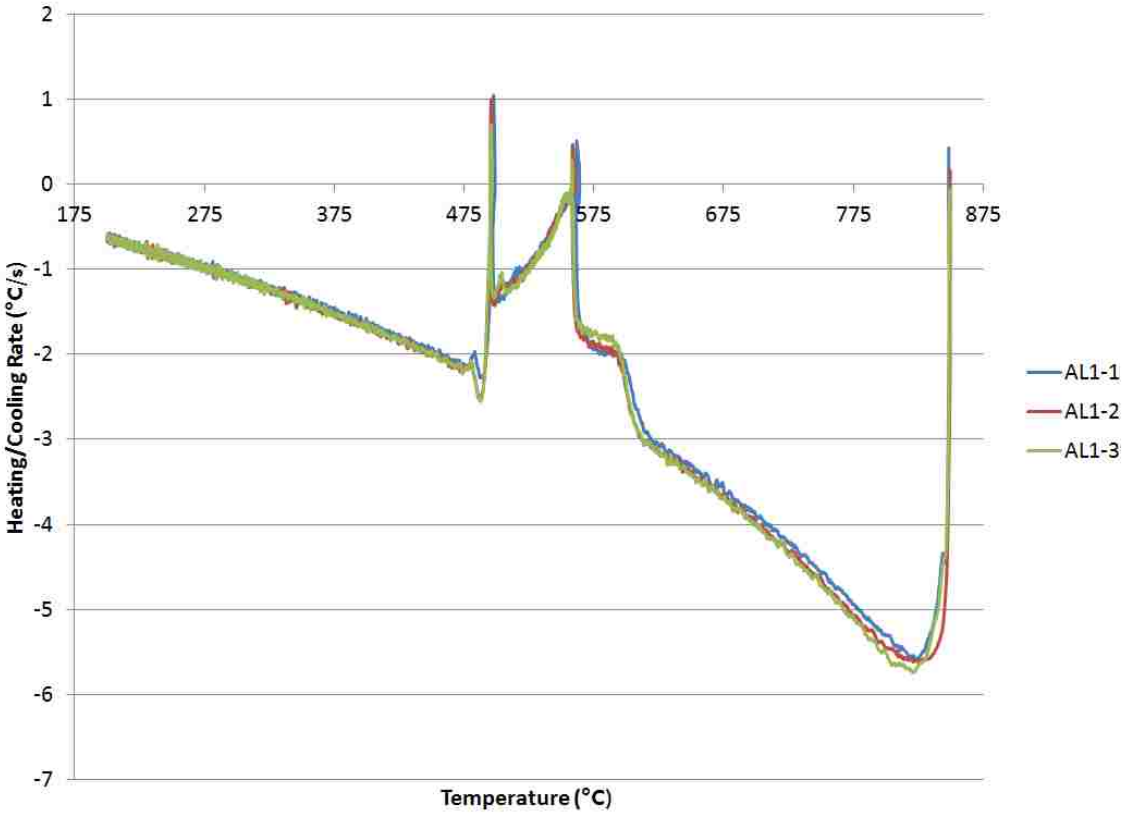

Figure 19 - dT/dt/T of Al20SiSr sample with no added cooling (AL1).

Figure 20 shows results of similar testing performed with compressed Ar cooling. Peak placement matches quite well with the non-cooling case. However, several gradual shifts in the morphology of the curves can already be seen. The small plateau (approx. 595-570˚C) in the no-cooling case (corresponding to primary silicon) has been absorbed into the nearby peak as the cooling rate increases. The baseline path, while relatively concave-down in the no-cooling case, has flattened out in the solid region and shifted to

concave-up in the liquid region. These are typical shifts in curve morphology as the cooling rate increases. One of the challenges in developing baselines for higher cooling rates is to understand the progression of these shifts and how they affect the positions of key metallurgical events. The addition of Sr causes an alloy solidification process more akin to a hypoeutectic alloy.

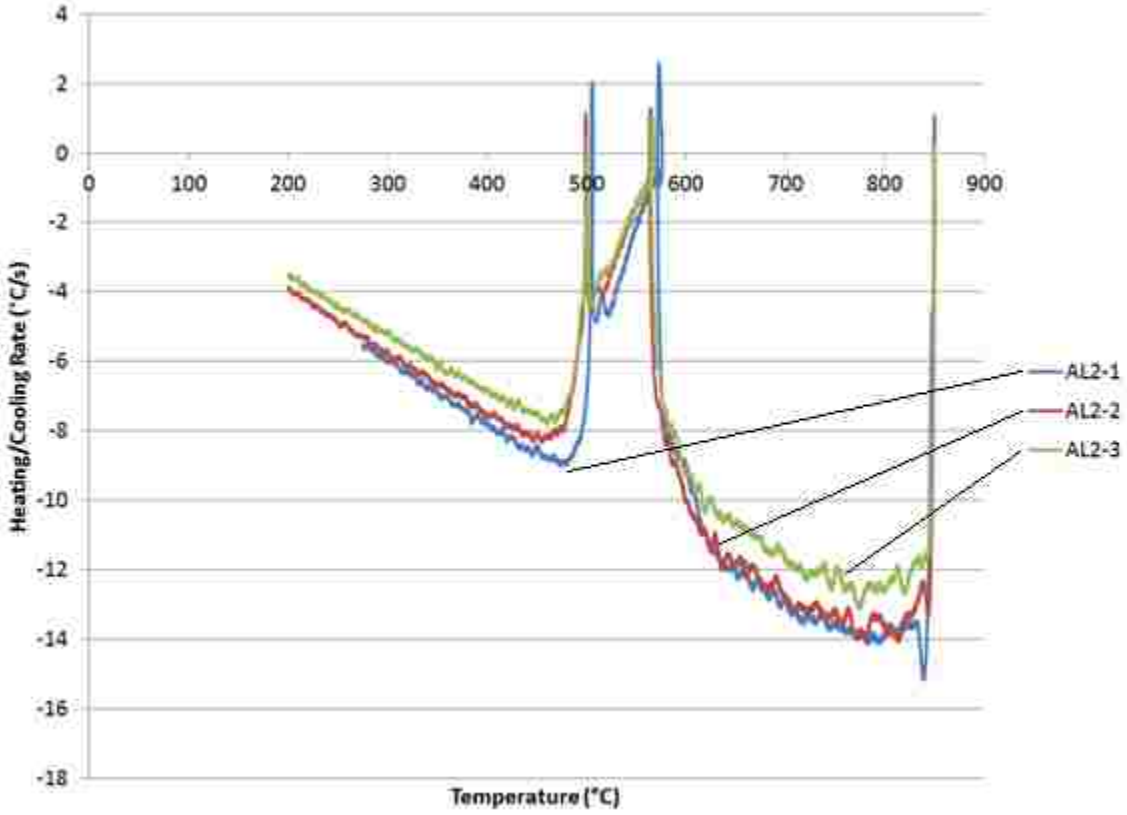

Figure 20 - dT/dt/T of Al20SiSr sample cooled with compressed Ar (AL2).

4.2.2 LOM Observations

Figure 21 shows the final microstructure of the Al20SiSr sample which had no additional quenching added. The structure appears to be dominated by fairly large grains as well as large, irregularly-shaped and blocky intermetallics near the edges. There is also a significant amount of porosity present which is expected for a slowly-cooled sample.

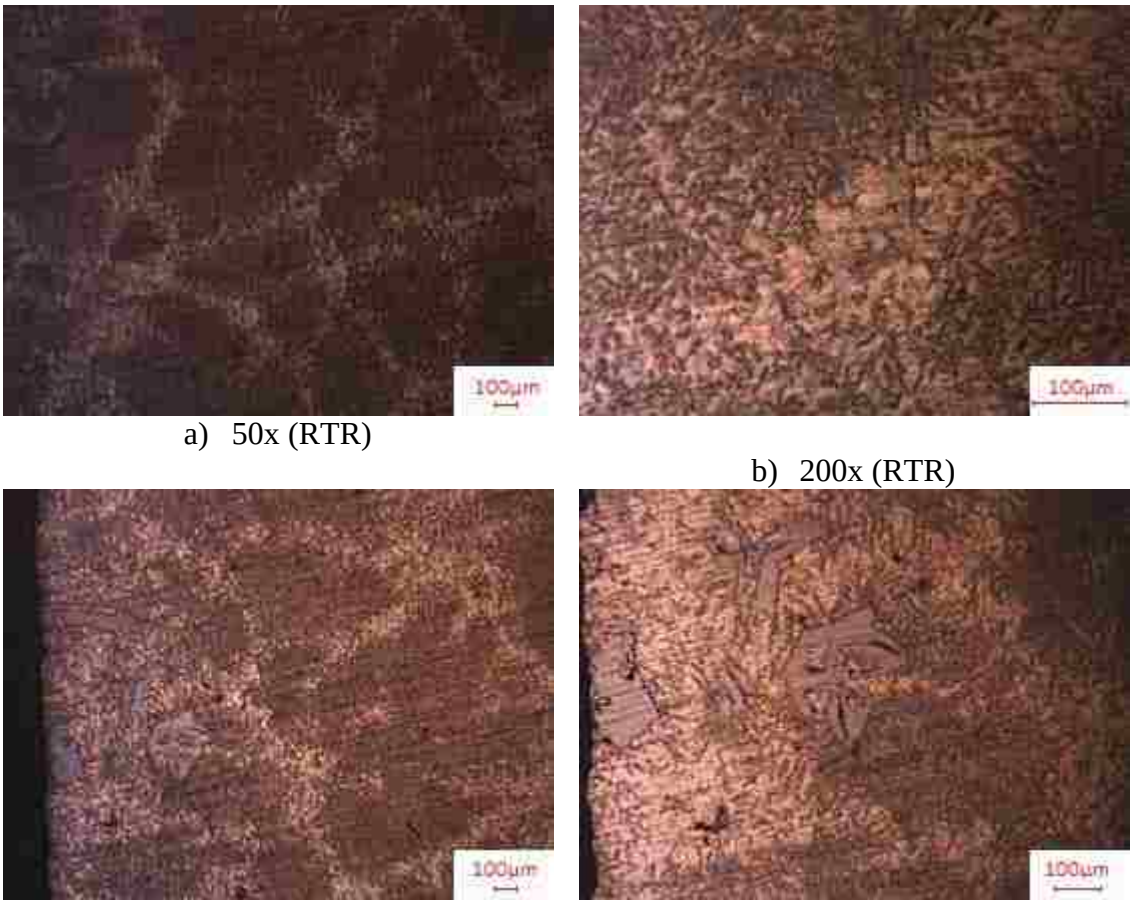

a) 50x (RTR)

b) 200x (RTR)

c) 50x (RML)

d) 100x (RML)

Figure 21 - Micrographs of Al20SiSr cooled at 5.7°C/s peak (1.2°C/s avg.) (AL1).

Figure 22 shows micrographs of the final microstructure for the AL2 sample. In general, there were relatively large dendrites extending across significant portions of the sample width. Large intermetallics and silicon crystals can be seen, however these are fairly irregularly shaped.

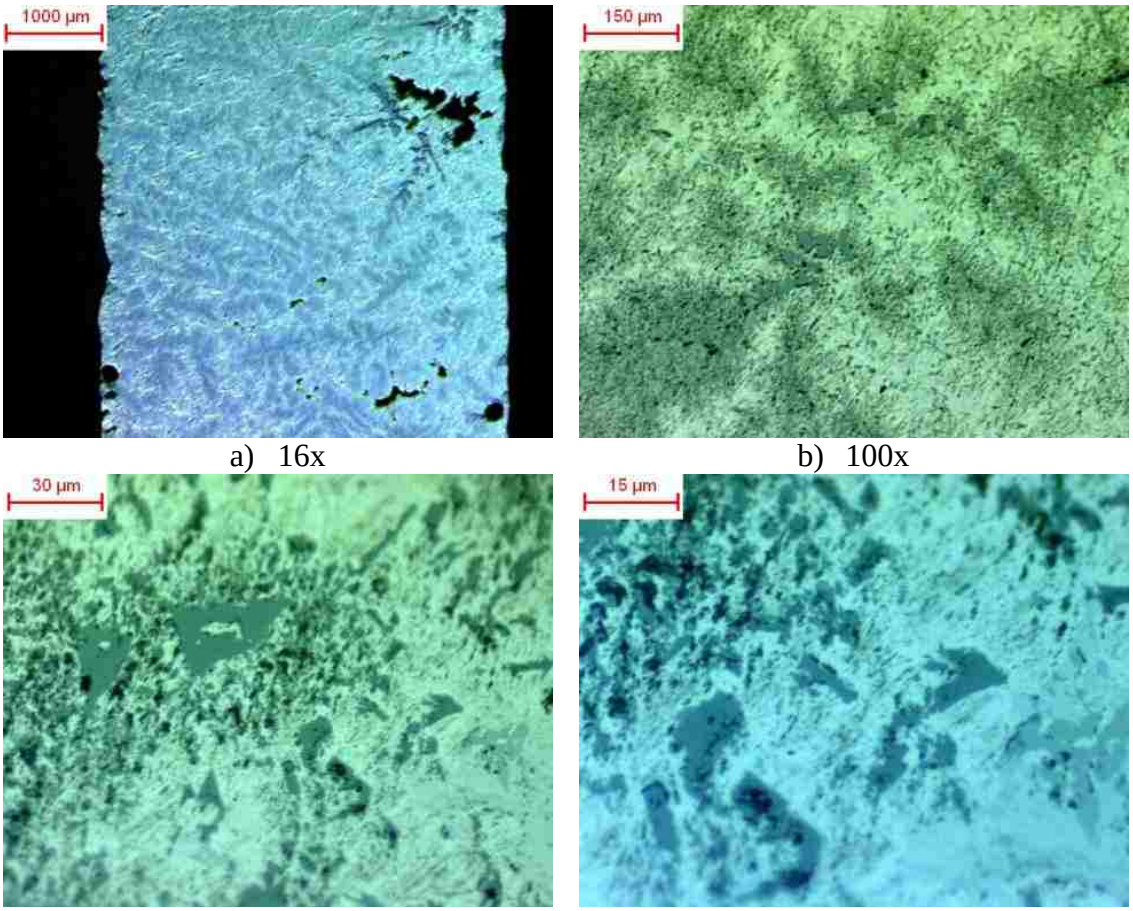

a) 16x b) 100x

c) 500x d) 1000x

Figure 22 - Micrographs of Al20SiSr cooled at 13.1°C/s peak (4.1°C/s avg.) in the RMM region (AL2).

The literature presents micrographs for the unmodified alloy cooled at a similar rate to the compressed Ar, as shown in Figure 23. This figure would be most comparable to Figure 22 b). There is considerable difference in the silicon modification level. The ED of primary silicon is approximately 89.7 ± 17.3 µm and the size of the SDAS approximately 22.1 ± 5.9 µm. Comparing the two pictures, modified and unmodified, it appears that Sr is quite influential in preventing the formation of primary Si crystals.

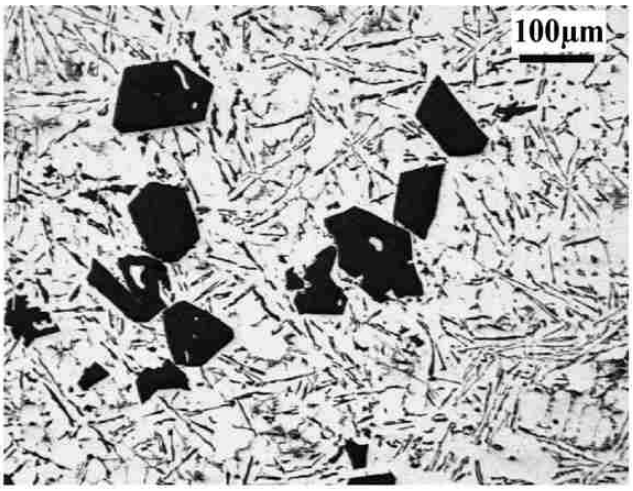

Figure 23 - Unmodified hypereutectic sample cooled at 4.9°C/s avg. [68].

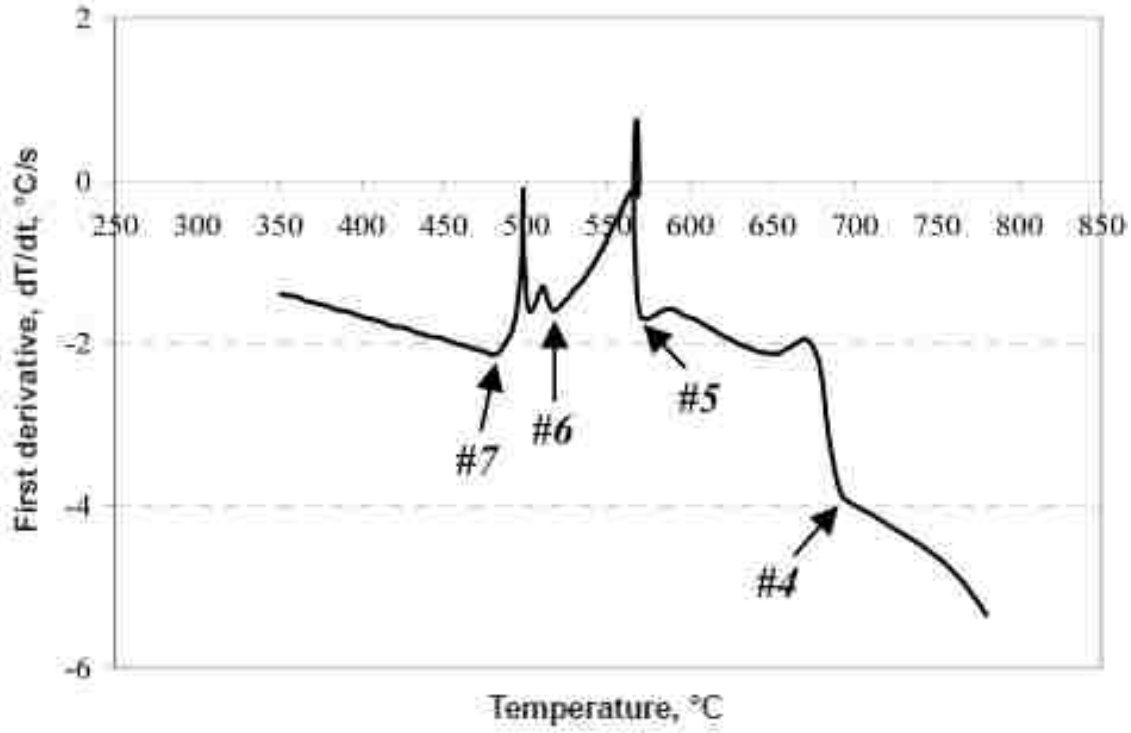

Figure 24 - dT/dt/T of unmodified hypereutectic alloy cooled at 1.3°C/s (avg.) [77].

Figure 24 shows the derivative of a cooling curve generated by Kasprzak et al. on the same unmodified hypereutectic alloy [77]. The sample was allowed to cool naturally at an average rate of 1.3°C/s. The labeled points are: #4 - Nucleation of the primary

Si/Liquidus, #5 - Nucleation of the AlSi eutectic, #6 - Nucleation of the Cu-based phases and #7- Solidus. Its shape is very similar to the curve in the Al20SiSr natural cooling test (1.21˚C/s) differing mostly in the length of the plateau between #4 and #5.

4.3 Characterization of Al20SiSr at High Cooling Rates

4.3.1 Cooling Curves

Figure 25 and Figure 26 show derivatives of cooling curves versus time for two samples, both rapidly cooled using water.

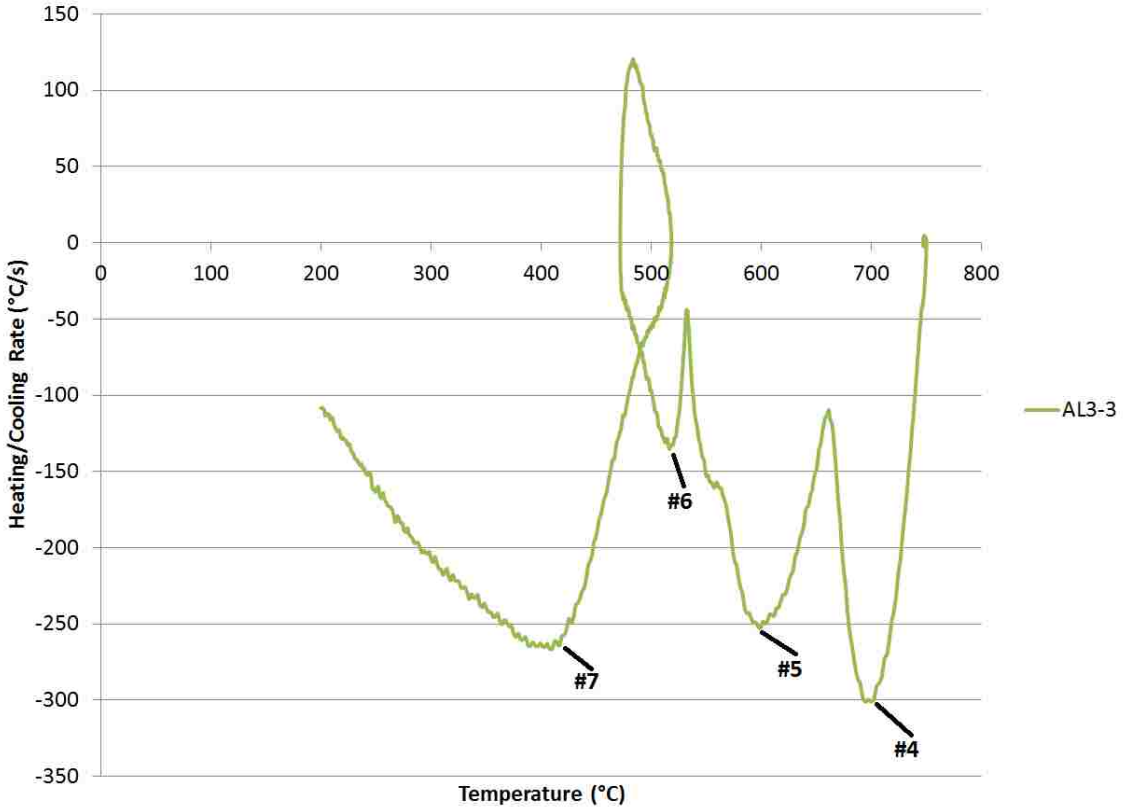

Figure 25 - dT/dt/T of Al20SiSr samples cooled with water (AL3).

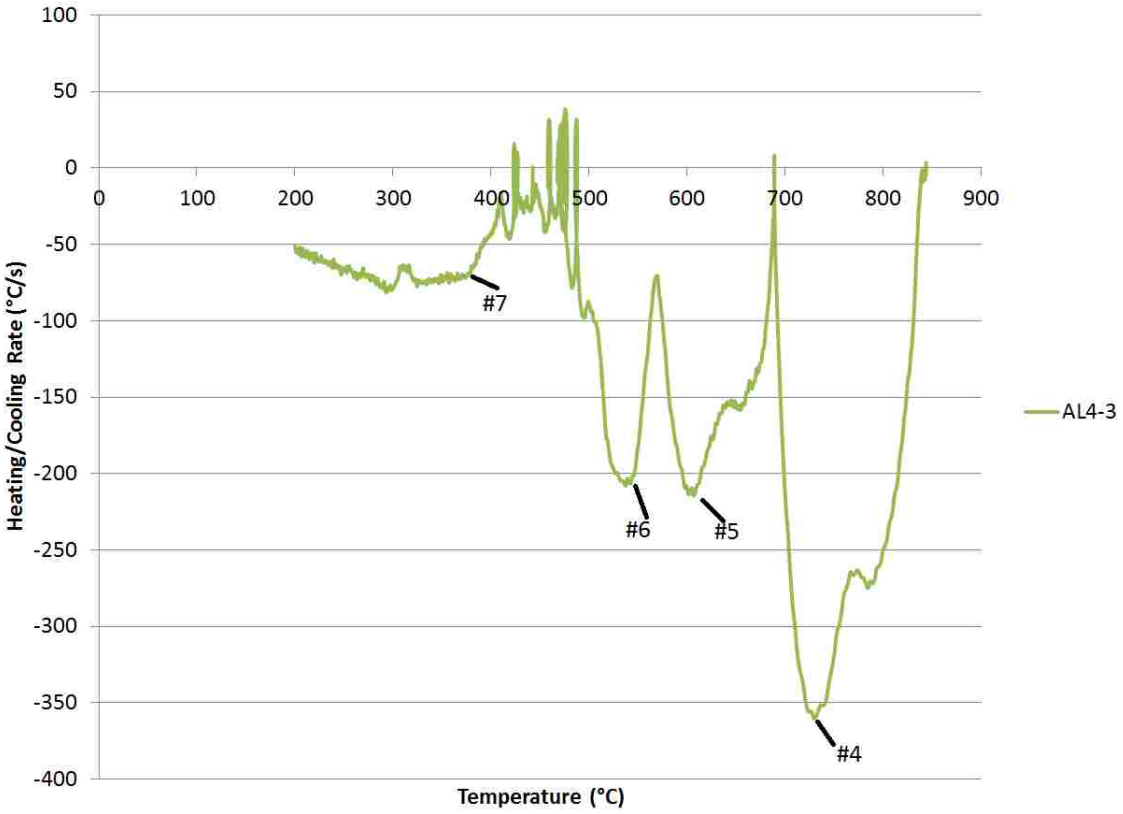

Figure 26 - dT/dt/T of Al20SiSr samples cooled with water (AL4).

The above thermal curve derivatives were the most difficult to account for in the study. For no clear reason, the traces are very irregular, especially when compared to the high-quality rapid solidification data in later sections. The metallurgical events in these traces are all visible and have some internal consistency between runs on the same sample. Even between the two samples, there are some similarities (e.g. large endothermic events at ~550°C and ~690°C) however these tests cannot be used for any accurate measurement. Because a similar hypereutectic sample was used previously on the UMSA, it is believed that the influence of Sr may have some detrimental effect on signal quality, however future work would have to be done to confirm this. Sr may also be responsible for the very significant amount of undercooling present in both graphs (with recalescence causing positive heating rates to be registered for brief periods).

Figure 27 shows a cooling curve derivative from the unmodified alloy. The sample was cooled at approx. 15°C/s (average) with the use of forced He (better heat transfer

than Ar). The increased rate changed the shape of the curve considerably and is not quite comparable to the nearest cooling rate in the present research (AL2 - 4.5°C/s average). It is, however, quite similar to AL3 and AL4. Points #4, #5 and #6 can be seen as peaks at approximately the same temperatures in AL3 and AL4. #7 is also present, though at a lower temperature because of significant undercooling, perhaps due to the Sr influence.

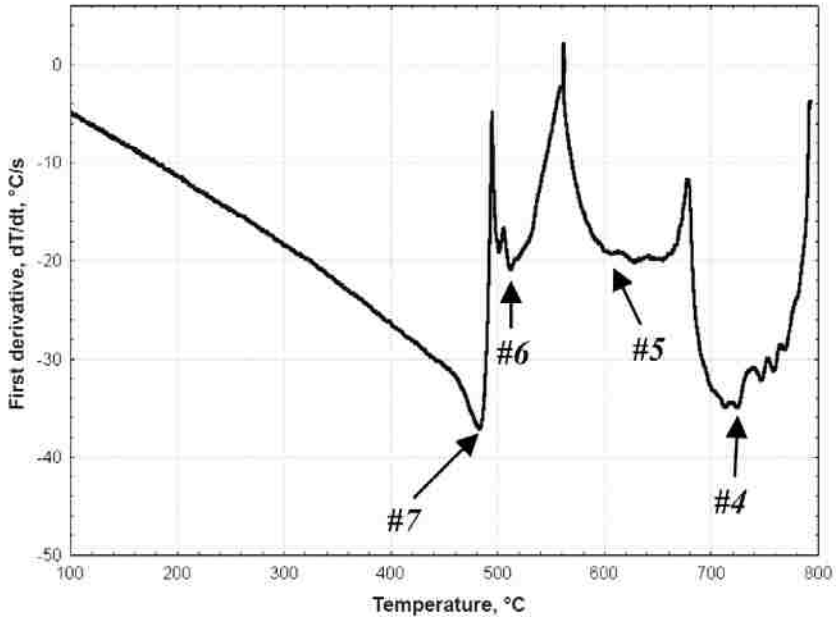

Figure 27 - dT/dt/T of unmodified hypereutectic alloy cooled at 15°C/s (avg.) [77].

The cooling curve data from Yamaha [68] for its full range of cooling rates is shown in Figure 28. It is difficult to determine the quality of the thermal data for the rapidly-cooled samples (d and e) based on this data.

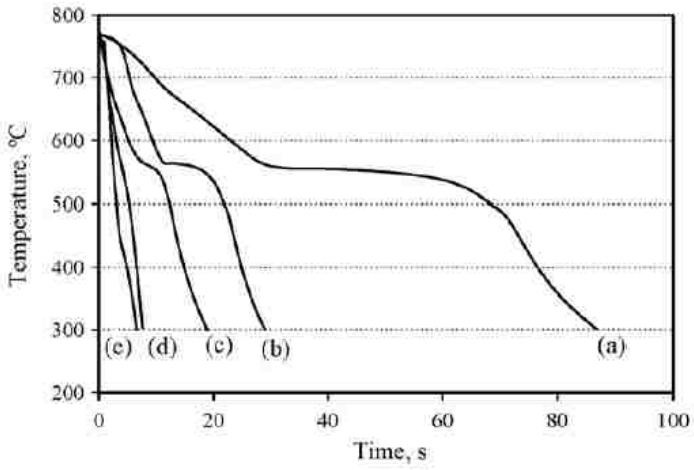

Figure 28 - Cooling curves recorded during Yamaha experiments. The CR for each curve is (a) 4.9, (b) 14.7, (c) 23.9, (d) 52.7 and (e) 82.9°C/s avg. [68].

The comparable cooling curves for the Al20SiSr tests are shown in Figure 29. **Note:** a log scale is used in order to better view all of the curves.

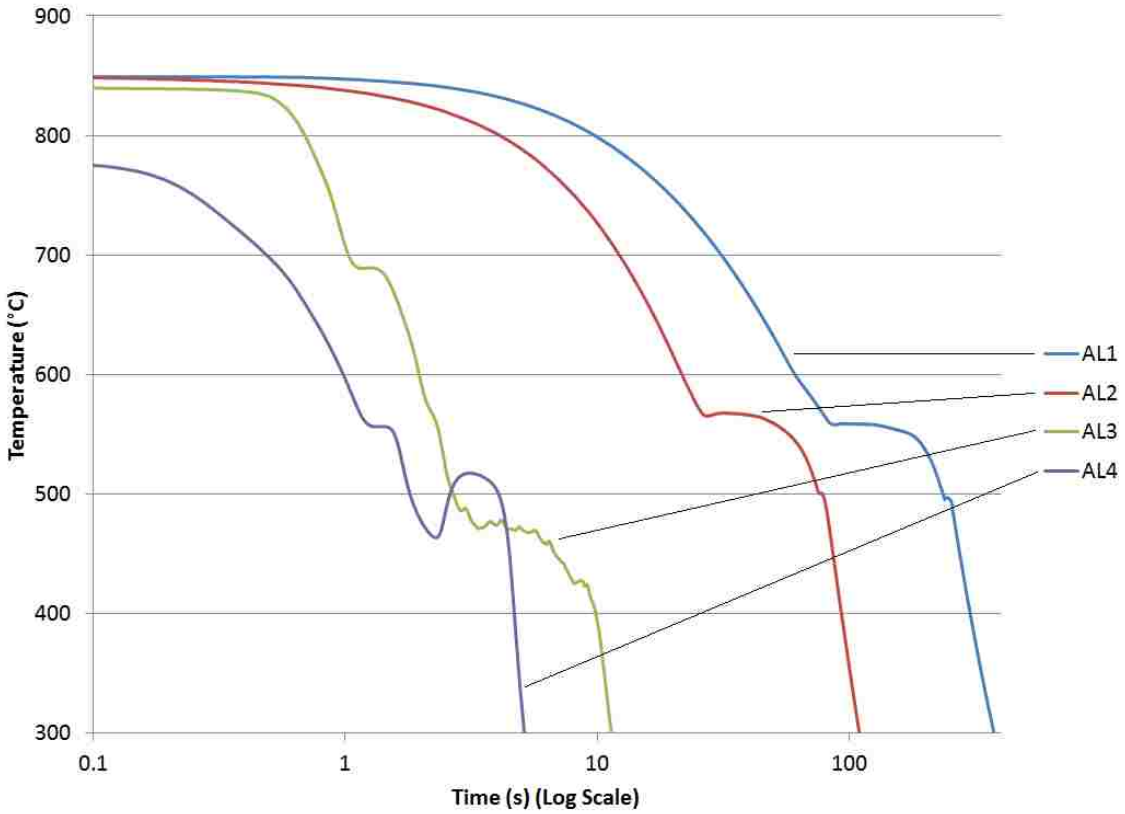

Figure 29 - Cooling curves for Al20SiSr tests (AL1-AL4).

4.3.2 LOM Observations

Figure 30 and Figure 31 show micrographs from the two rapidly-cooled Al20SiSr samples. Although the thermal data is less than ideal, the effects of rapid solidification as well as Sr modification are clear in the microstructure.

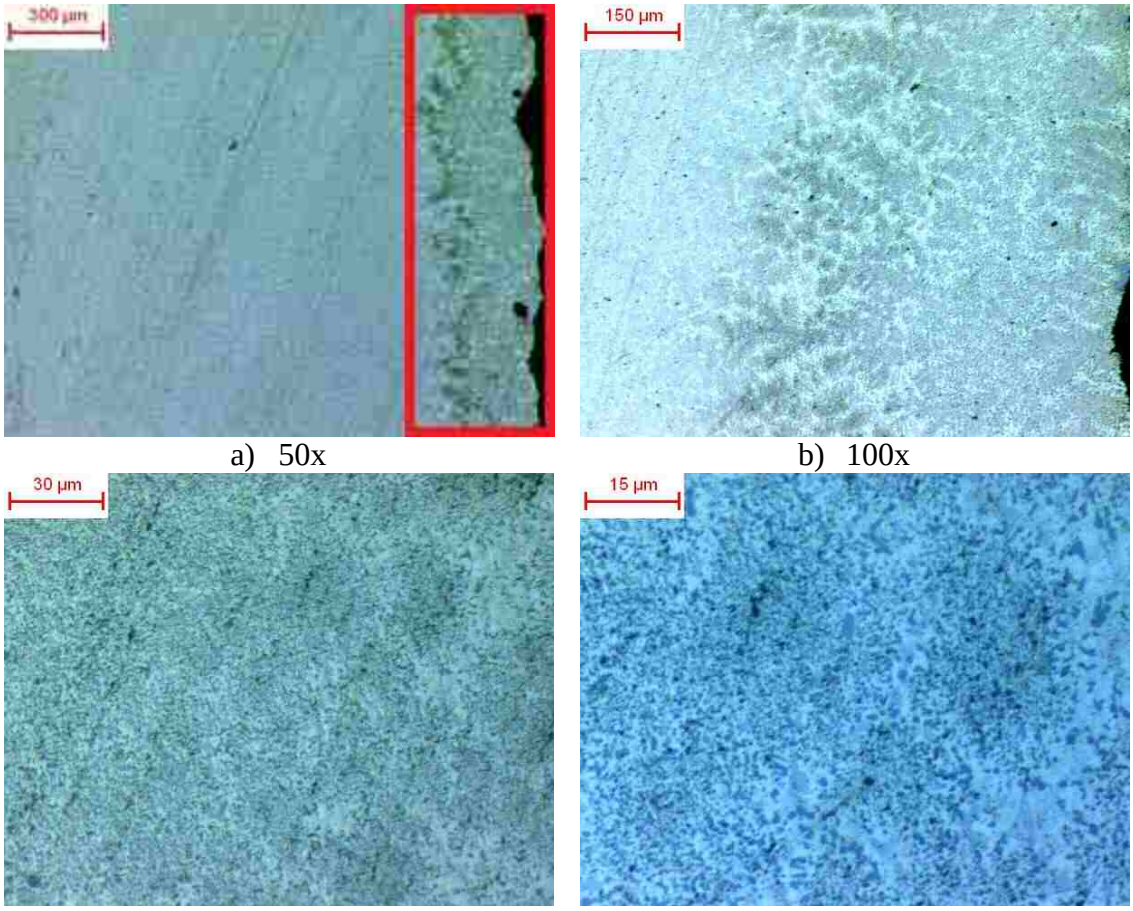

a) 50x b) 100x

c) 500x d) 1000x

Figure 30 - Micrographs of Al20SiSr cooled at 264°C/s peak (79.0°C/s avg.) in the LMR region (AL3).

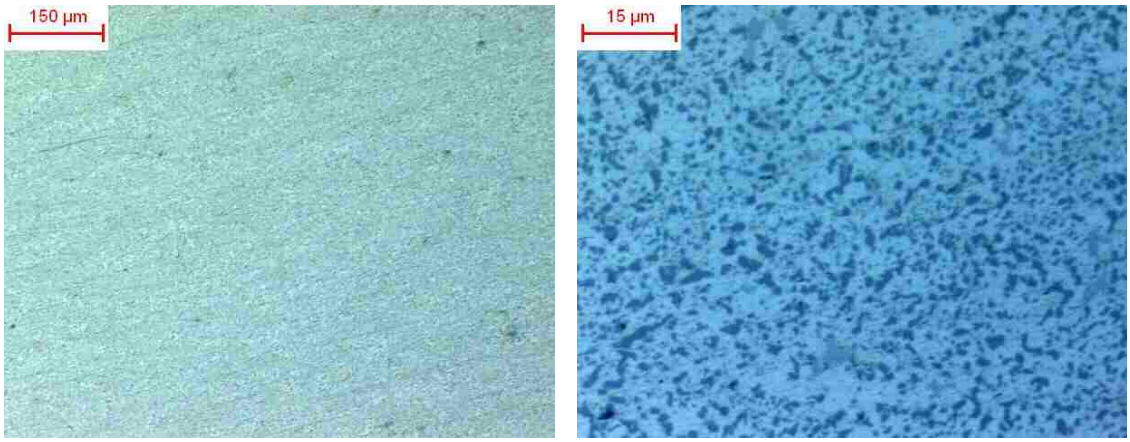

a.) 100x b.) 1000x

Figure 31 - Micrographs of Al20SiSr cooled at 360°C/s peak (37.6°C/s avg.) in the RMM region (AL4).

On both samples, there is a dendritic skin present on the edges, highlighted in Figure 30a) and is approximately 300µm wide. The bulk of the sample appears to be made up of a flat featureless region, as in Figure 30a) and Figure 31b), which is revealed as an extremely fine structure at the highest magnifications. These roughly micron-sized, equiaxed crystals are an ideal structure and likely have excellent mechanical properties. Figure 32 shows a comparison with the unmodified alloy which at first glance looks similar, but would be a better match for either Figure 30b) or Figure 31a) based on the scale and cooling rates. Likely owing to the Sr influence, the crystals taken at 1000x magnification are most similar to the unmodified sample, suggesting almost an order of magnitude improvement in silicon size.

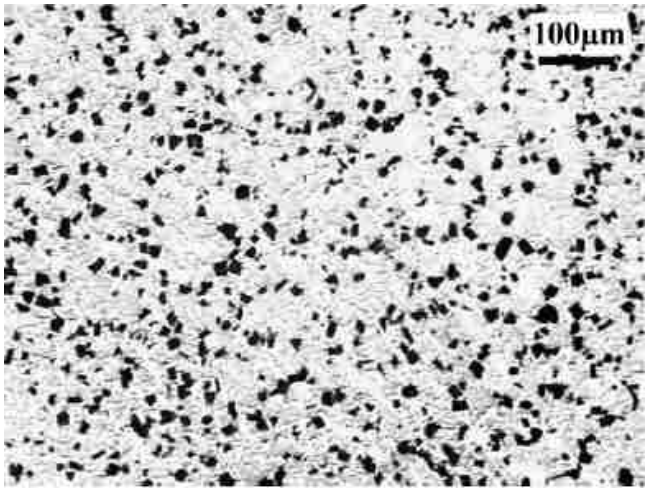

Figure 32 - Unmodified hypereutectic sample cooled at 82.9°C/s avg. [68].

4.4 Characterization of Al20SiSr with Solution Treatment

4.4.1 Cooling Curves

Figure 33 shows a comparison between the thermal curves of two solution treated Al20SiSr samples. AL5 was held at the solution temperature (510°C) for approximately 120 seconds while AL6 was held for approximately 90 minutes (note the discontinuity in the graph). The motivation for choosing the temperature was its use in the Kasprzak paper [5] while the length of time was chosen simply to have a comparison between very short and very long treatment times. The discrepancy between the two graphs, roughly between 450s and 550s, is due to the UMSA being triggered to hold the solution temperature after a particular time threshold has been reached instead of temperature threshold. Because of a difference in the shutoff times of the cooling mechanism, AL5 was allowed to reach a much lower temperature before solution treating, however it is not believed that the temperature drop significantly affects the microstructural results. At the end of both holding periods at the solution temperature, the sample is allowed to cool naturally to room temperature.

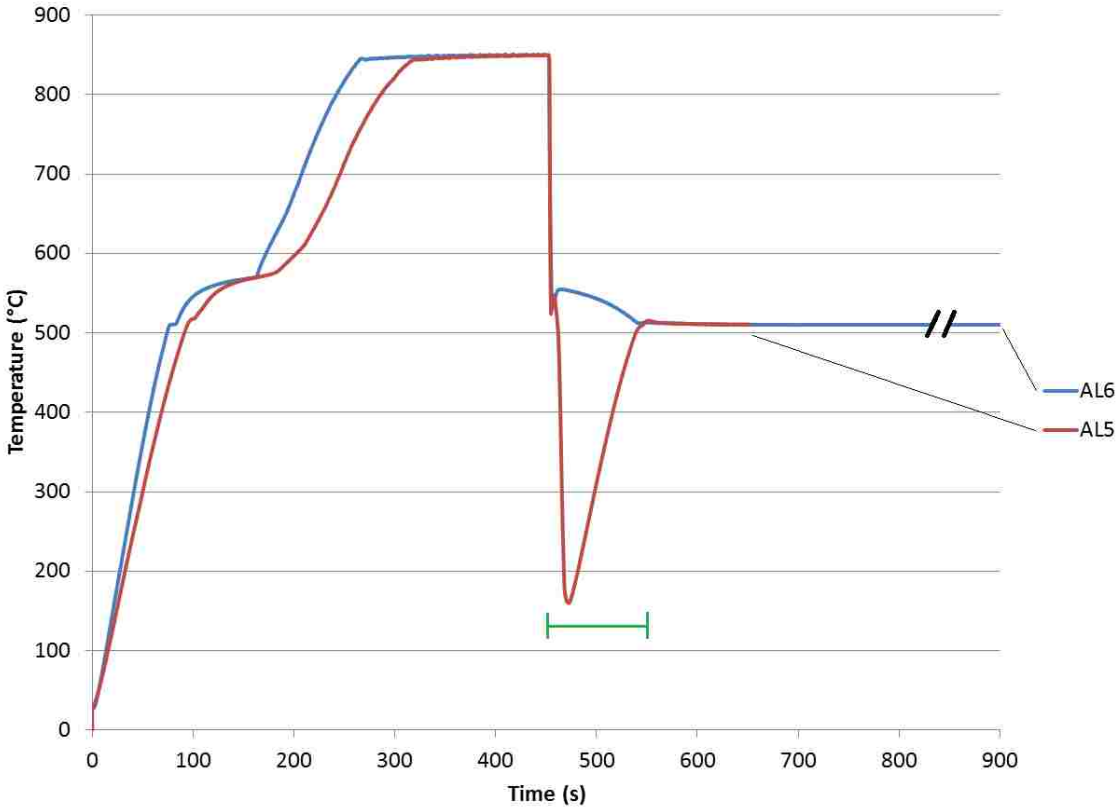

Figure 33 - Thermal curve comparison between two solution treatments on Al20SiSr.

4.4.2 LOM Observations

Figure 34 shows micrographs taken from the sample with short solution treatment. Overall the structure is fairly refined with small silicon crystals, as seen in c). However several fairly long dendrites appear, even at the lowest magnification.

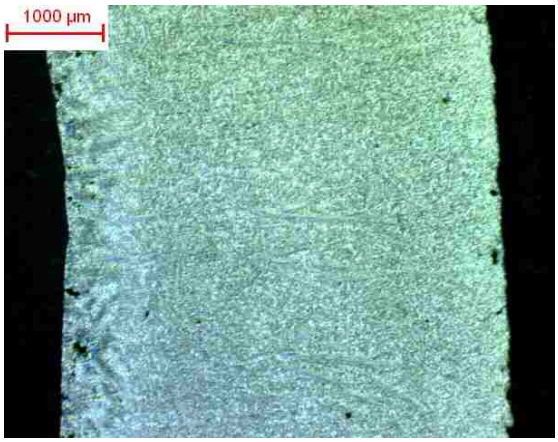

a) 16x (LMM)

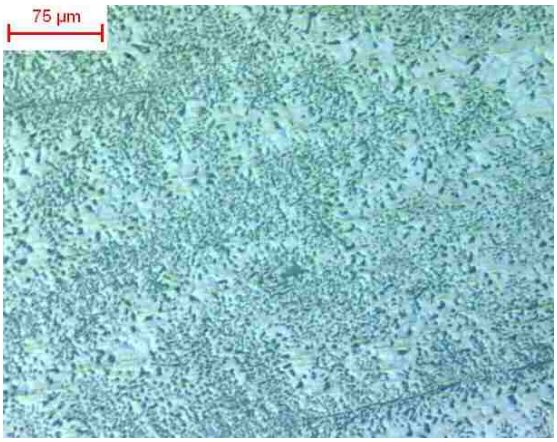

b) 200x (LMM)

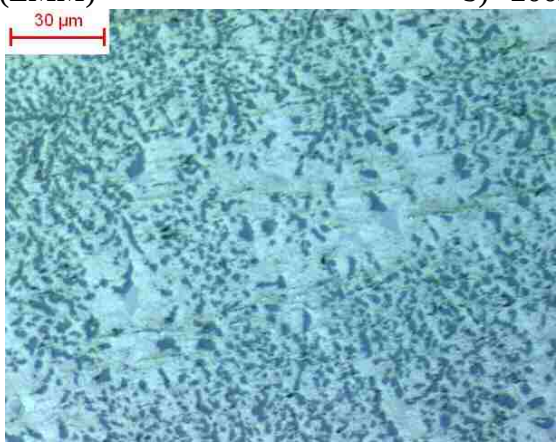

c) 500x (LMM)

Figure 34 - Micrographs of Al20SiSr with short solution treatment (AL5).

Figure 35 shows micrographs from the sample with long solution treatment. The structure is quite poor with large silicon crystals as well as significant porosity problems. The long treatment time has allowed for too much diffusion of hydrogen which has in turn led to large porosity. The results seem to indicate that future treatments should focus on extremely short treatment (although temperature adjustments may still be advisable).

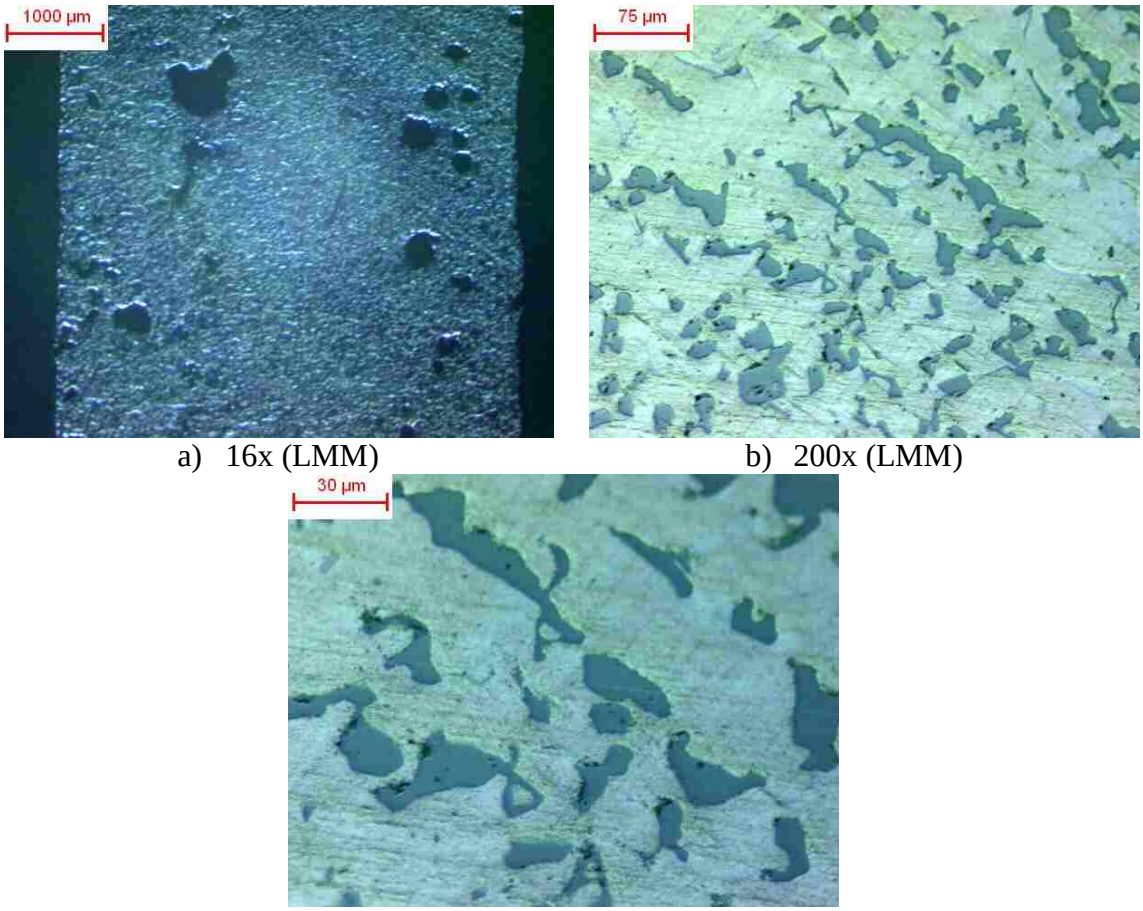

a) 16x (LMM) b) 200x (LMM)

c) 500x (LMM)

Figure 35 - Micrographs of Al20SiSr with short solution treatment (AL6).

4.5 Characterization of A356 at Low Cooling Rates

4.5.1 Cooling Curves

Figure 36 shows the cooling curve derivatives of two different A356 samples cooled at different rates. The trials for both samples have an excellent internal consistency, with all three major peaks being coincident. There is however a noticeable, yet relatively stable shift, between the peak data for the two different samples. For air, the peaks occur at approximately 599°C, 557°C and 538°C and for compressed Ar at 624°C, 580°C and 557°C, for differences of 25°C, 23°C and 19°C respectively.

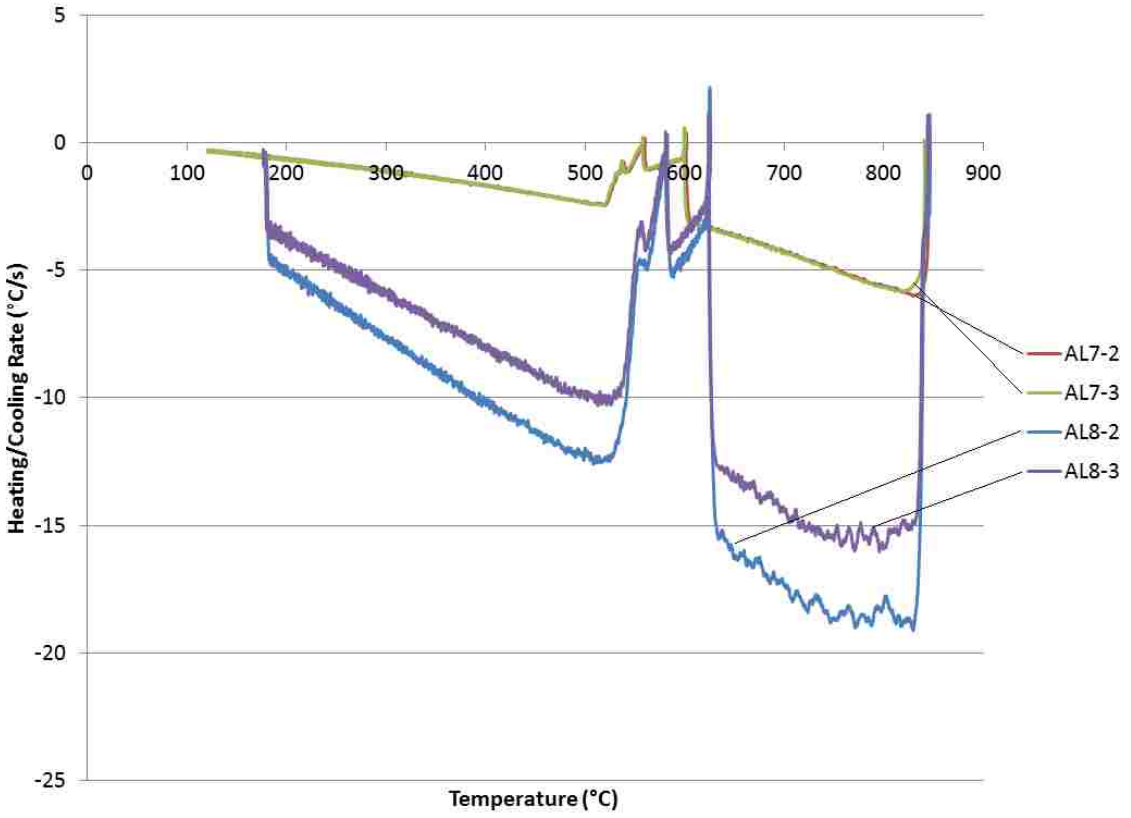

Figure 36 - dT/dt/T of A356 samples cooled with no added cooling (AL7) and compressed Ar cooling (AL8).

4.5.2 LOM Observations

Figure 37 shows micrographs from the air-cooled sample. As expected, the structure features large intermetallics and dendrites and is rather reminiscent of the structure in the literature, Figure 3a).

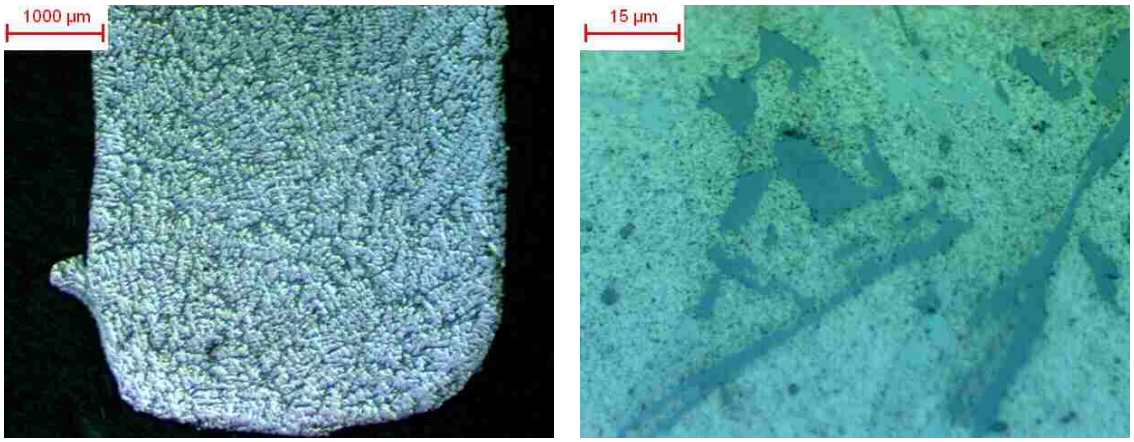

a) 16x (LBM) b) 1000x (LTL)

Figure 37 - Micrographs of A356 cooled at 5.8°C/s peak (1.1°C/s avg.) (AL7).

Figure 38 below shows micrographs from the compressed argon cooled sample. It sees a noticeable decrease in the size of intermetallics, however it remains fairly similar to the air-cooled sample.

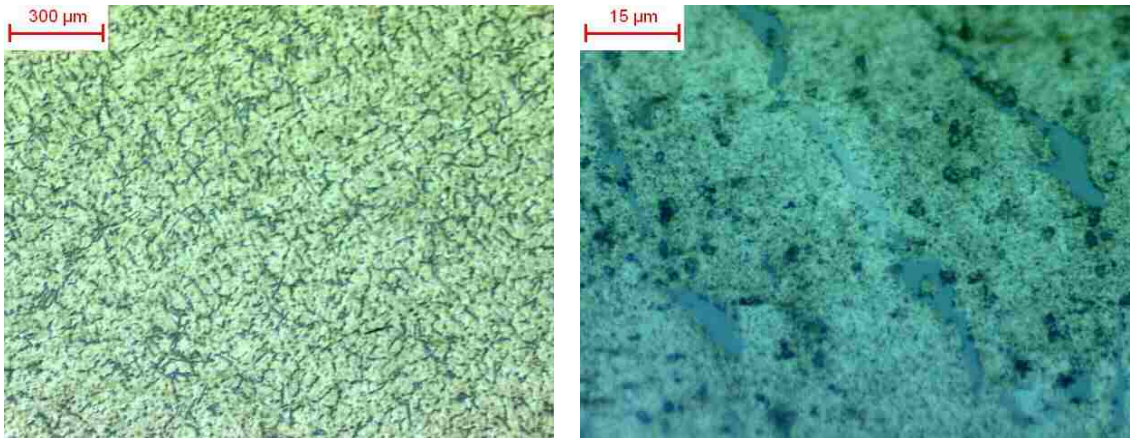

a) 50x (LMM) b) 1000x (LBM)

Figure 38 - Micrographs of A356 cooled at 16°C/s peak (4.2°C/s avg.) (AL8).

4.6 Characterization of A356 at High Cooling Rates

4.6.1 Cooling Curves

Figure 39 shows the cooling curve derivatives from two trials of the same rapidly cooled A356 sample. It is significantly less noisy than the comparable rapidly-cooled Al20SiSr data. This may be due to having a smaller concentration of alloying elements, whose

complex interactions would create additional peaks. However, the clear distinction between liquid, semi-solid and solid regions is lost. Clear peaks are seen at 575˚C and 615˚C (similar to two of the compressed Ar peaks) as well as a smaller event at 720˚C (perhaps a heat transfer rate change due to dissolution of the vapour blanket). In contrast with other rapid cooling thermal data, these curves also have very high cooling rates in the solid region.

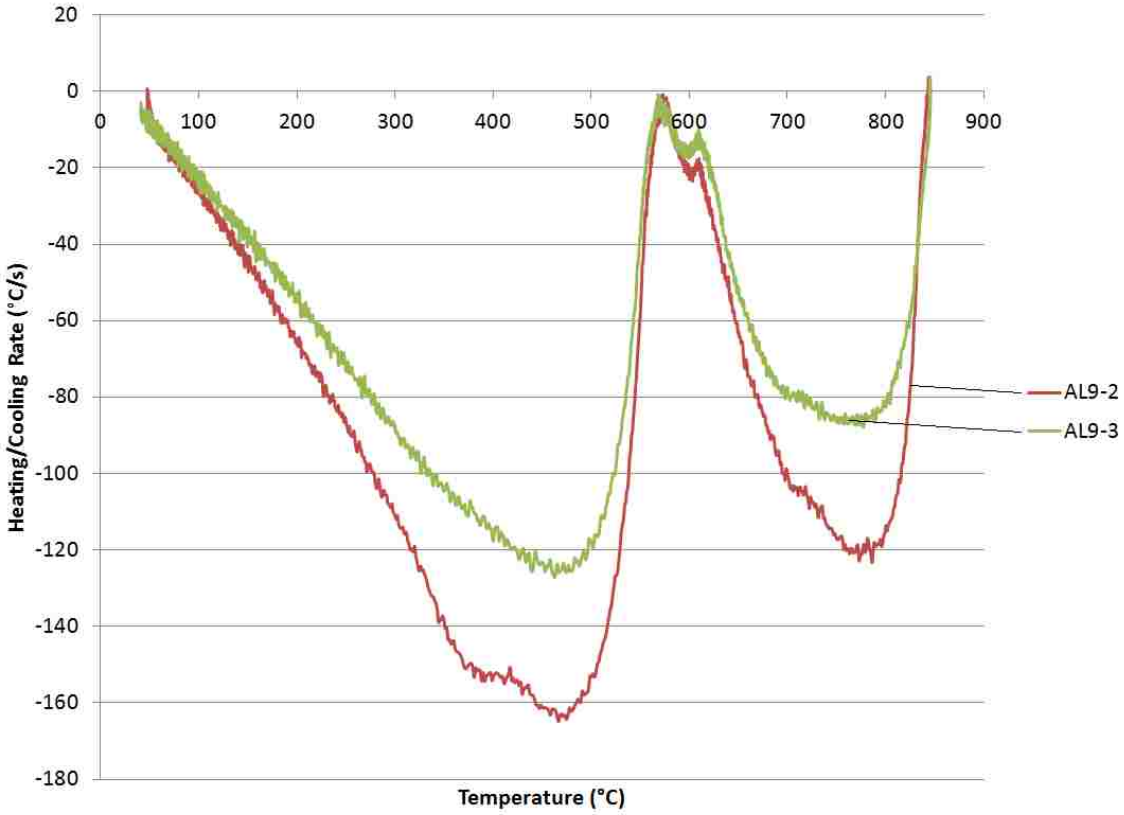

Figure 39 - dT/dt/T of A356 samples cooled with water (AL9).

4.6.2 LOM Observations

Figure 40 shows micrographs from the water-cooled A356 sample. The intermetallics are significantly smaller and more needle-like.

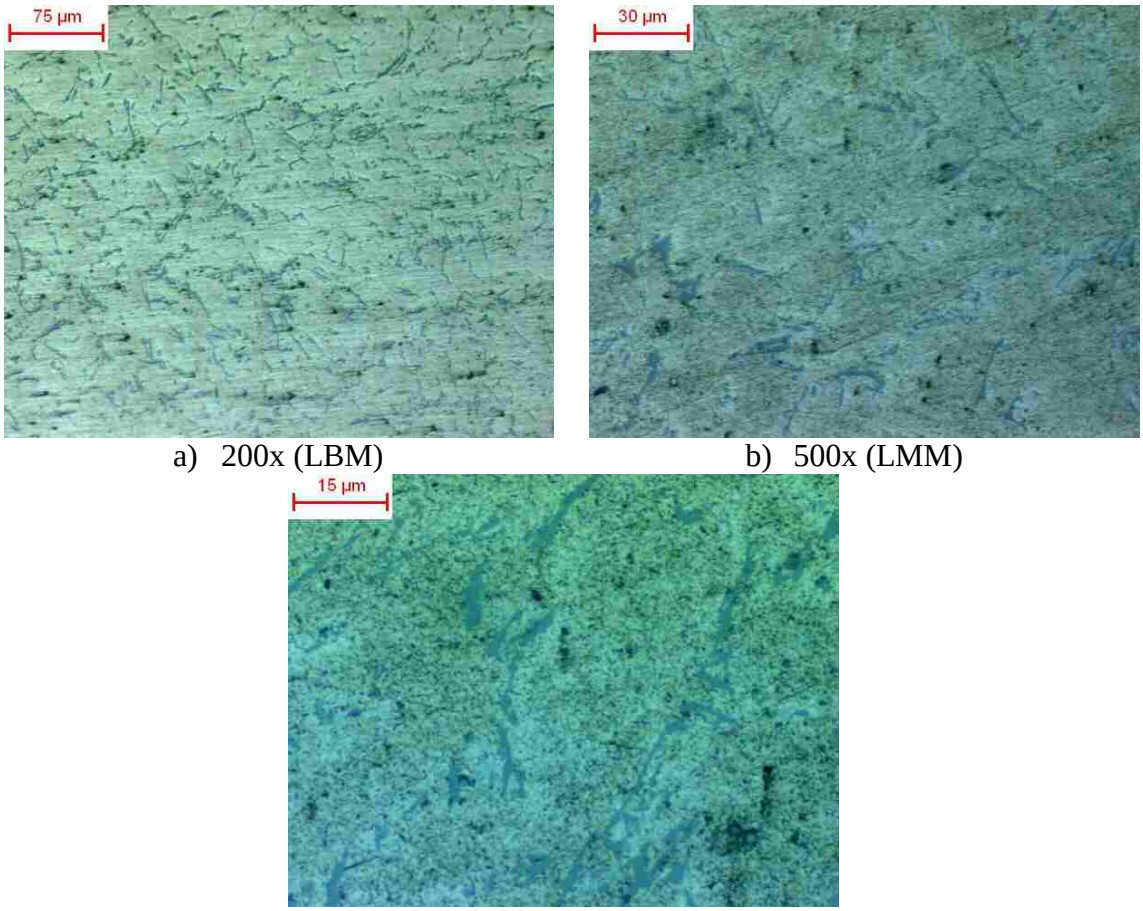

a) 200x (LBM) b) 500x (LMM)

c) 1000x (LMM)

Figure 40 - Micrographs of A356 cooled at 127°C/s peak (22.5°C/s avg.) (AL9).

4.7 Characterization of AM60B[6]

4.7.1 Cooling Curve Analysis

Figure 41 presents the derivatives of the cooling curves gathered for most AM60B experiments. The thermal data shown is of excellent quality and because of the range of cooling rates shown, trends can be seen in the shifting of the peaks with respect to cooling rates. The largest endothermic peak (located from 608-620˚C in MG1) appears to generally drift to lower temperatures in response to the cooling rate. The smaller endothermic peak (located from 424-434˚C in MG1) is located just before the solidus

[6] This section incorporates material that is the result of joint research.

temperature and stays generally constant with respect to cooling rate, however becomes increasingly less pronounced.

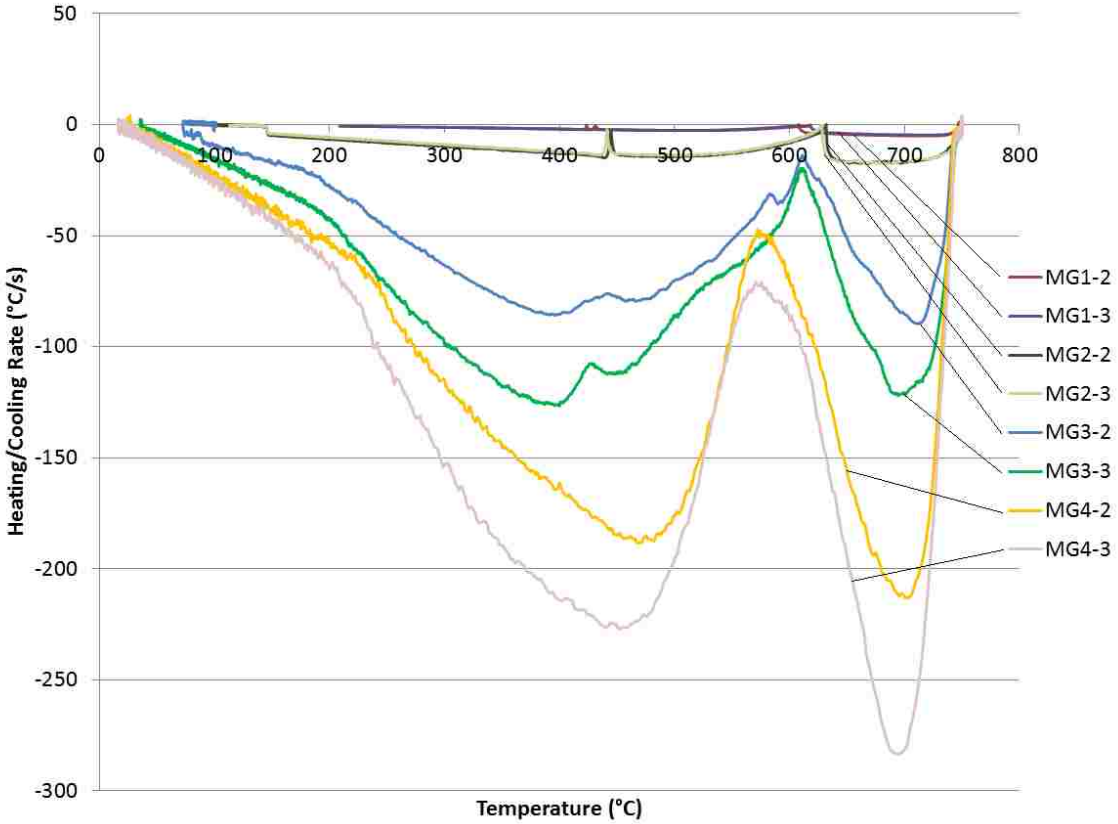

Figure 41 - dT/dt/T of slowly and rapidly cooled AM60B (MG1 - MG4).

The wide range in cooling rates seen in Figure 41 is a result of the different quenching methods used to solidify the sample. The cooling rates and cooling methods for the thermal curves shown are provided in Table 17.

Table 17 - Summary of cooling methods and cooling rates for AM60B experiments.

		Peak Cooling Rate (°C/s)	
Sample	**Cooling Method**	**Trial 2**	**Trial 3**
MG1	Natural cooling	5.0	4.7
MG2	Compressed argon	17.5	17.6
MG3	Water with 25% glycol	89.6	129.6
MG4	Water	213.2	283.4

Figure 42 shows a closeup of the slowly cooled samples (MG1 and MG2). There is a small shift to higher temperature for the compressed Ar cooled sample, which later reverses as cooling rates increase, however all the peaks are coincident within a fairly small range.

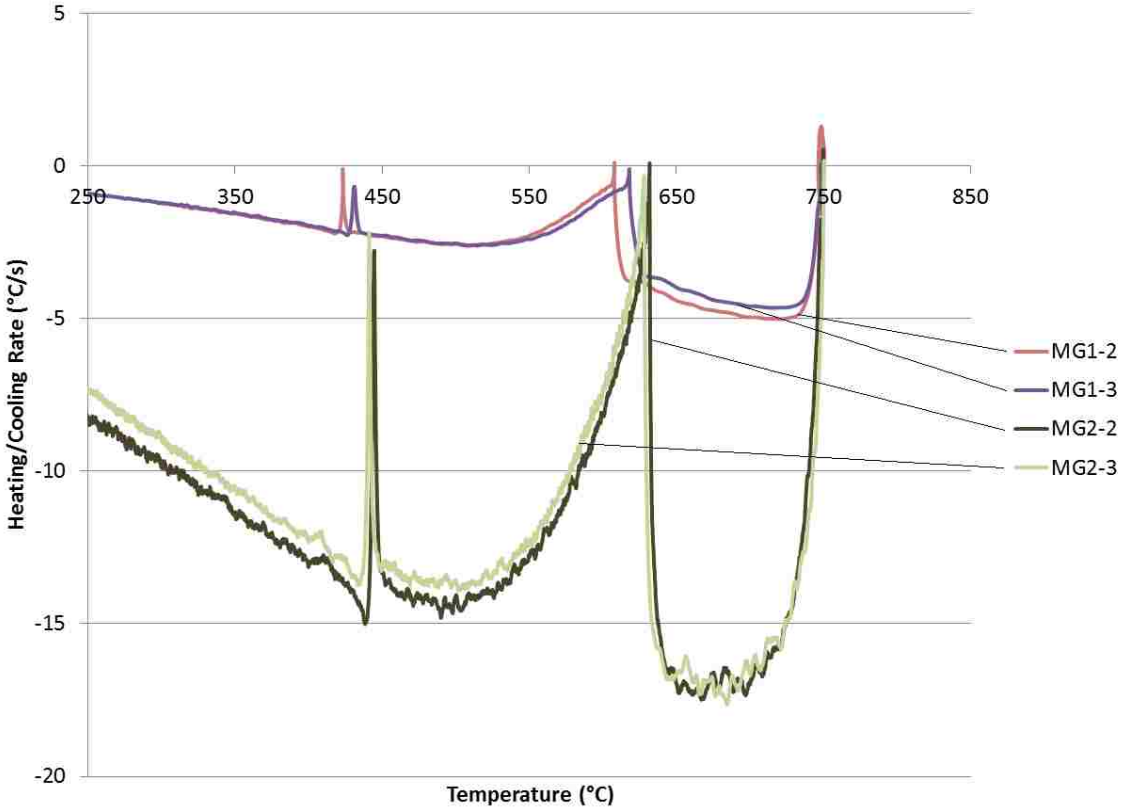

Figure 42 - dT/dt/T of slowly cooled AM60B (MG1 – MG2).

4.7.2 LOM Observations

Figure 43 shows a comparison between microstructures of AM60B samples from the lowest to highest cooling rates. Past 20+ °C/s, the grain structure (equiaxed) and direction (radially outward) are not noticeably affected by the cooling rate. At more rapid rates, grain size decreases and there is a slight size gradient in the cooling direction with grains growing later in the solidification process.

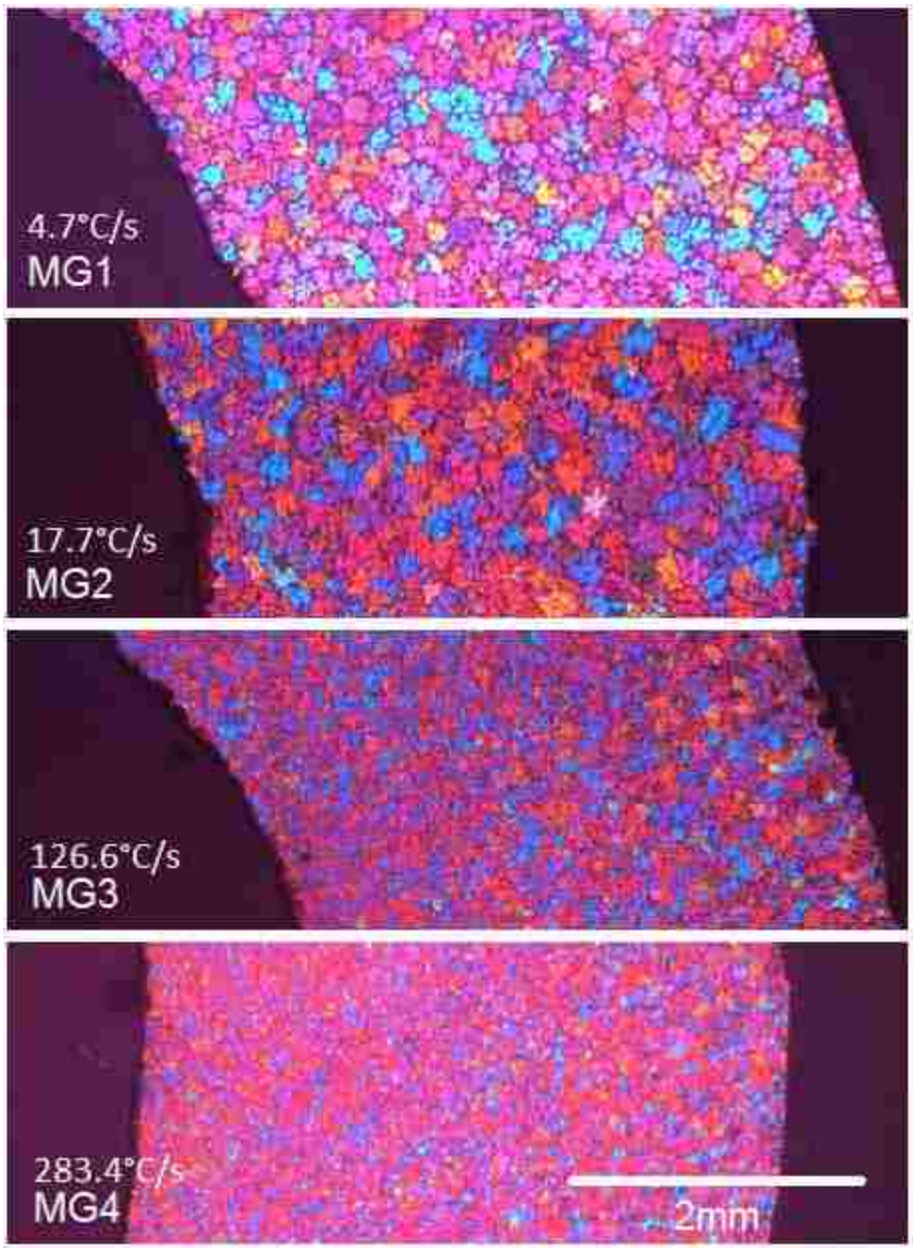

Figure 43 - Comparison of AM60B microstructure at different cooling rates (MG1 - MG4). 16x magnification.

Figure 44 shows a closer comparison of the grains in the 280°C/s sample. As there is little change in grain morphology with respect to cooling rate, the grain structure remains relatively constant across the wall of the sample. Images were taken from a polished and etched section accentuating the grain boundaries and intermetallics which are found both inside and between αMg grains. 'Start' refers to the region near the inner wall of the

sample (where cooling starts) while Centre and End refer to the middle region and outer wall respectively.

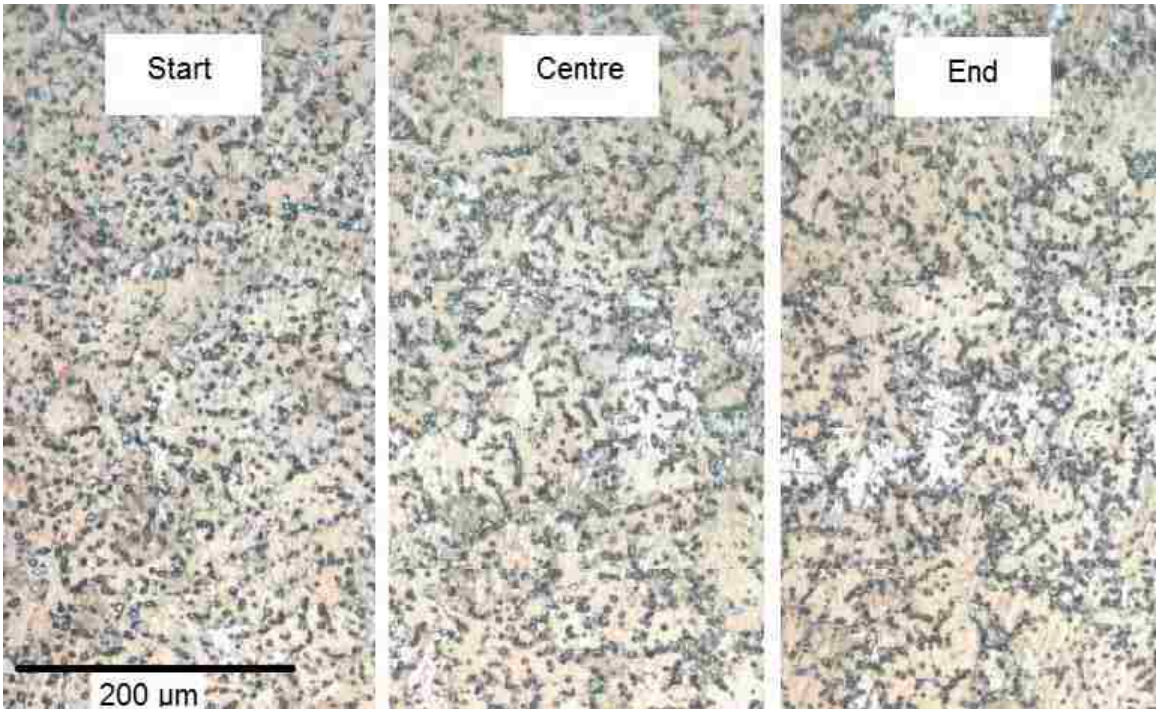

Figure 44 - AM60B - Comparison of grain size and morphology in Start, Centre and End regions for a sample solidified at 280°C/s peak. 200x magnification.

Figure 45 shows a closer comparison of grain structure between the slowest and fastest cooling rates. Enhanced tendency for dendritic growth is shown at higher solidification rates. Grains nucleate at solid particles and grow outward in all directions regardless of the direction of heat extraction.

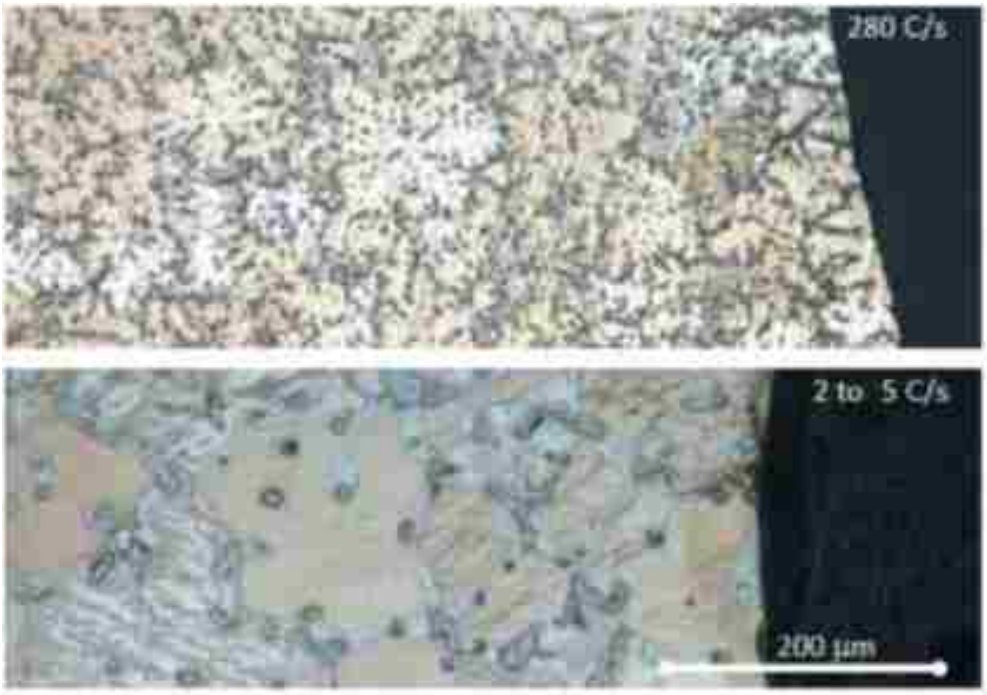

Figure 45 - Comparison of grain morphology in the start region between samples solidified at 280°C/s and at 2°C/s to 5°C/s. 200x magnification.

4.8 Characterization of AE44[7]

4.8.1 Cooling Curves

Figure 46 and Figure 47 show thermal curves from both AE44 as well as pure magnesium. The pure magnesium was tested primarily for calibration purposes and not a focus of the research. The melting point of pure magnesium is 650°C. Ideally, pure magnesium would show up as a single, straight peak, however because the metal used was only industrial grade purity there is some noticeable width to the peak.

[7] This section incorporates material that is the result of joint research.

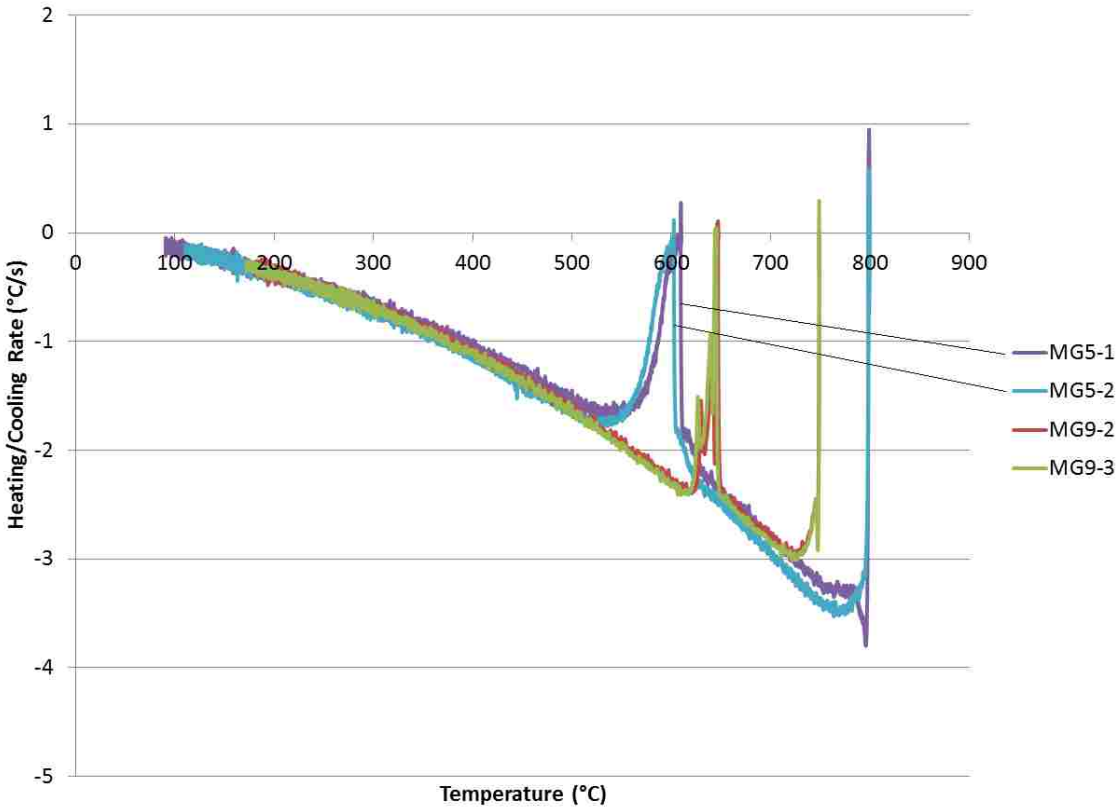

Figure 46 - dT/dt/T of slowly cooled AE44 and pure Mg (MG5, MG9).

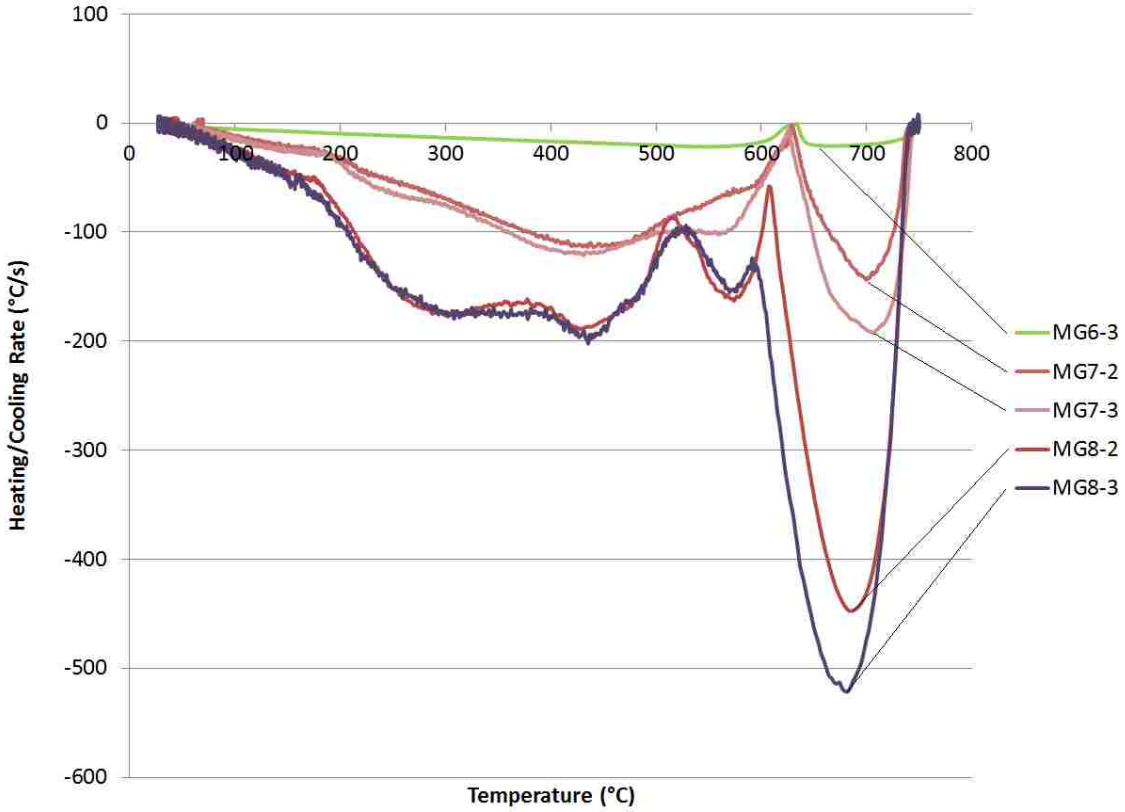

Figure 47 - dT/dt/T of slowly and rapidly cooled AE44 (MG6-MG8).

4.8.2 LOM Observations

Figure 48 shows a comparison of grain structure between two AE44 samples cooled at different rates. At 500°C/s, the grains grow radially almost right across the 3 mm wall of the sample. At 22°C/s, the radial, outward grain growth pattern is replaced by extremely large equiaxed grains. In both cases, there appears to be another set of grains that nucleated on the outer surface and grew inward. Hence it appears that there is preferential heterogeneous nucleation at the boron nitride coated foil container and very ineffective nucleation in the liquid on the solidifying intermetallics.

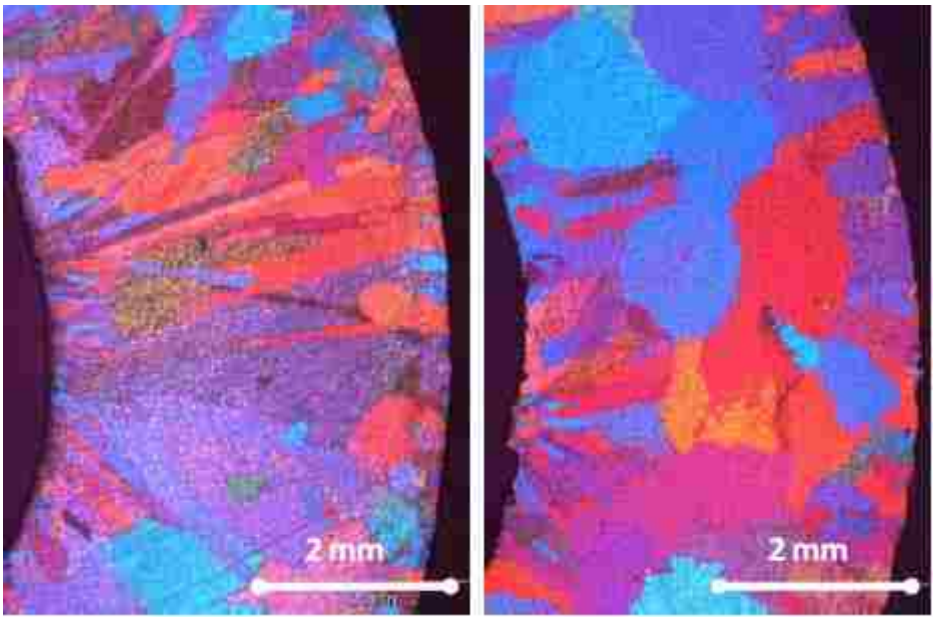

Figure 48 - AE44 - Comparison of grain morphology in samples solidified at 500°C/s (left) and 22°C/s (right). 16x magnification.

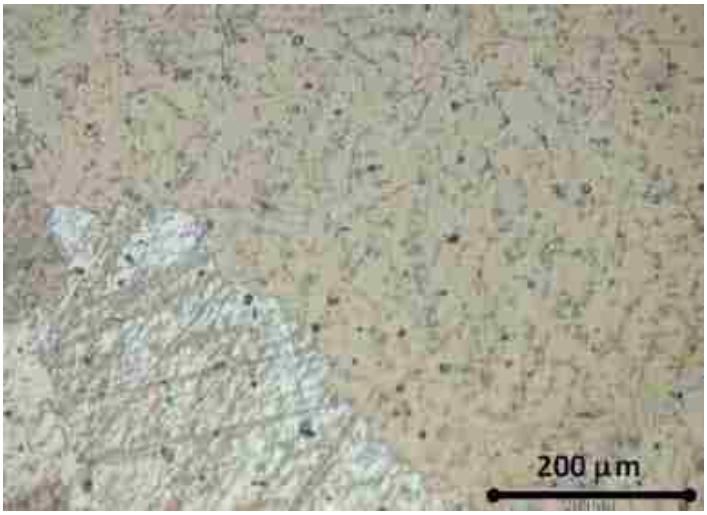

Figure 49 - Micrograph of AE44 sample cooled with compressed Ar at 22°C/s (MG6). 200x magnification.

Figure 49 shows that cooling at intermediate rates produces a very tortuous grain boundary between large αMg grains. The grains are full of small intermetallics. This structure implies that the intermetallics precipitated first in the liquid and then αMg matrix grew among them without nucleating new αMg grains.

Figure 50 below shows the microstructure of the most rapidly cooled AE44 sample. It reveals that grains are actually large αMg dendrite colonies with dendrite trunks growing in a predominantly radial direction. The nucleation and inward growth of coarse dendrites extends up to ~300μm from the outer surface.

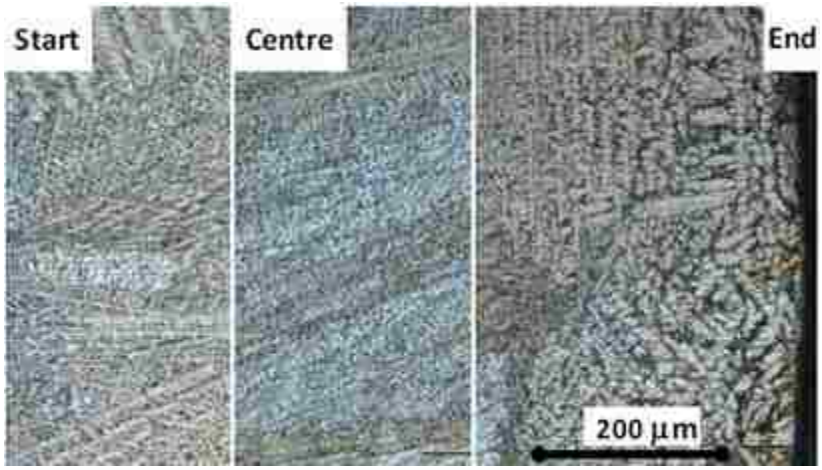

Figure 50 - Grain structure of AE44 cooled at 500°C/s (MG8). 200x magnification.

4.9 Baseline Development for Rapidly Cooled Magnesium Alloys[8]

The cooling curve is derived from the time-temperature record of the sample being cycled through repeated melting and solidification cycles. The slope of a linear fit with several adjacent data points to smooth and differentiate the temperature data with respect to time. The cooling rate becomes less negative as the sample temperature drops, reducing the temperature difference between the sample and the coolant. The area of the peaks superposed on this sloped baseline represents the enthalpy of solidification of the various solid phases crystalizing out of the melt. To calculate the peak areas one must first calculate the portion of the baseline in the semi-solid region.

[8] This section incorporates material that is the result of joint research.

4.9.1 Baseline Determination

For the magnesium parent metal, the heat capacities of liquid and solid are different, which results in a shift in the baseline between the fully solid and fully liquid regions. At any temperature:

$$B_s/B_l = c_{pl}/c_{ps} \quad (18)$$

where B_s and B_l are baselines determined in liquid and solid respectively, and c_{pl} and c_{ps} are heat capacities of the liquid and solid. Further, in the semi-solid region the baseline value for the semi-solid mixture, B, can be calculated from the respective weight fractions of liquid and solid, f_l and f_s as follows:

$$1/B = (1-f_s)/B_l + f_s/B_s \quad (19)$$

Fraction solid at any time is estimated from the fraction of the total thermal solidification peak area that was integrated to that time. Since the peak area depends on the baseline, an iterative solution is required. The procedure is found to converge to a solution after a few iterations. The problem is simplified by ignoring the contribution of alloying elements to the baseline value. Figure 51 shows an example of the cooling curve as a function of temperature with the calculated baseline that accounts for the liquid and solid contributions in the semi-solid region. At the solidus (end of solidification) temperature the position of the B_l is calculated from the measured B_s value. This point is linearly interpolated to the measured B_l curve at the liquidus (start of solidification) temperature. The B_s curve between the liquidus and the solidus is then calculated from the B_l interpolated values according to Equation 18. The baseline B for the semi-solid mix is then calculated from B_s and B_l by iterative solution of Equation 19.

4.9.2 Enthalpy Calibration

The area of the baseline subtracted peak plotted against solidification time is proportional to the enthalpy of formation of the solid phase. The proportionality factor was determined by measuring the peak area for commercially pure Mg which has a latent heat of

solidification of 8.48 KJ/mole reported for pure Mg by the National Institute of Standards and Technology (NIST) at the melting point. The calibration is complicated by two facts. First, the measured area of the solidification peak depends on the cooling rate. The area, increases as the cooling rate goes more negative. Second, the enthalpy of solidification decreases as solidification temperature decreases. This decrease is significant for alloys with a wide solidification temperature range. The calibration measurements in commercially pure Mg spanned a range of 2°C/s to 20°C/s for a baseline value in during actual solidification. Linear interpolation fit to this data was used to calculate the conversion factor from the area measured in degrees centigrade to energy measured in joules:

$$C2J = \Delta H_m(T)/AP(dT/dt) \qquad (20)$$

Here $\Delta H_m(T)$ is the latent heat of solidification of Mg at temperature T and AP(dT/dt) is the measured area of the dT/dt peak with baseline subtracted and integrated with respect to time, at a specific baseline cooling rate. Individual C2J calibration factors were calculated for each data point and applied to the baseline subtracted dT/dt peak profile data before area integration. This was done to account for variation of the calibration factor with both temperature and the baseline cooling rate during the solidification event. Figure 51, Figure 52 and Figure 53 show examples of the cooling curve baseline subtraction and calibration results for alloy AM60B.

In Figure 51, the liquid baseline is extrapolated linearly to a point located at the solidus temperature and a value given by Equation 18. The solid baseline is extrapolated to the liquidus temperature based on Equation 18 and the interpolated value of the liquid baseline. Semi-solid mix baseline is calculated from the solid and liquid baselines according to Equation 19.

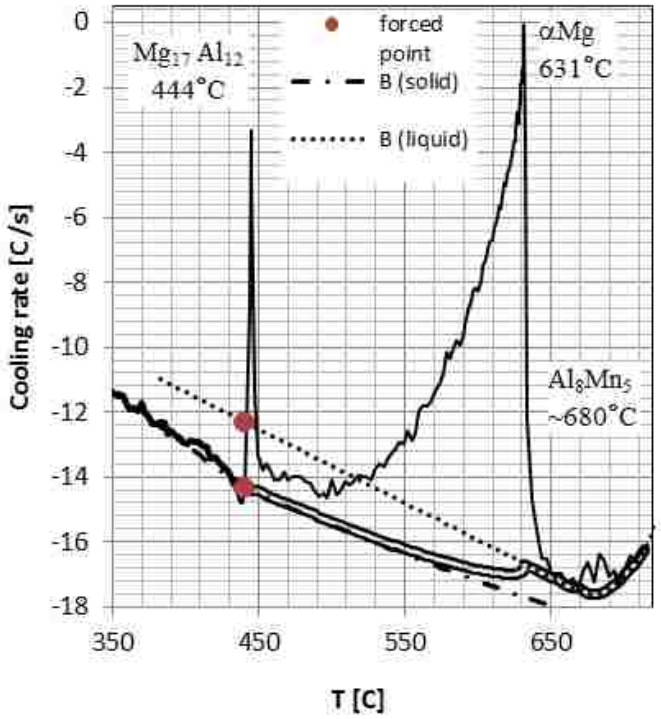

Figure 51 - AM60B cooling curve with calculated baseline.

The correlation between the cooling curve peaks, the phases observed in the microstructure and their identification is based on the phase quantity and location in the structure and the literature results on phase thermochemical and crystallographic properties and the alloy equilibrium phase diagram [78]. Integration of the individual peak areas yields experimental values for enthalpy of formation.

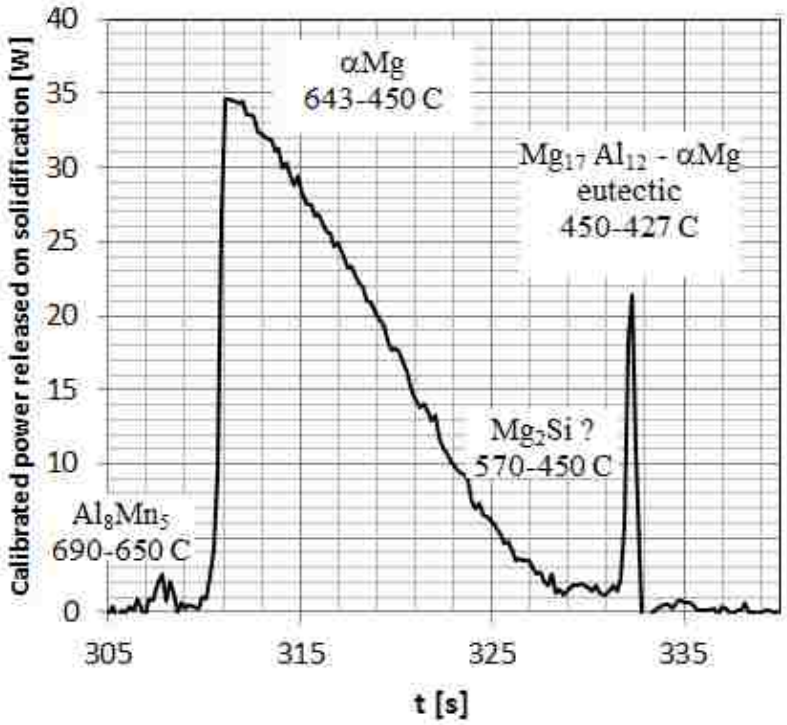

Figure 52 - Calibrated values of the power released during solidification of a 5.7g AM60B sample at 18°C/s to 14°C/s.

4.9.3 Phase Formation

The phase distribution information calculated from the microstructural and micro-chemical observations is combined with the evolution of fraction solid of each individual phase during the solidification event to generate a plot demonstrating the formation of the constituent solid phases and consumption of the melt as a function of the temperature. An example of such a plot for AM60B solidified at 18°C/s to 14°C/s is shown in Figure 53.

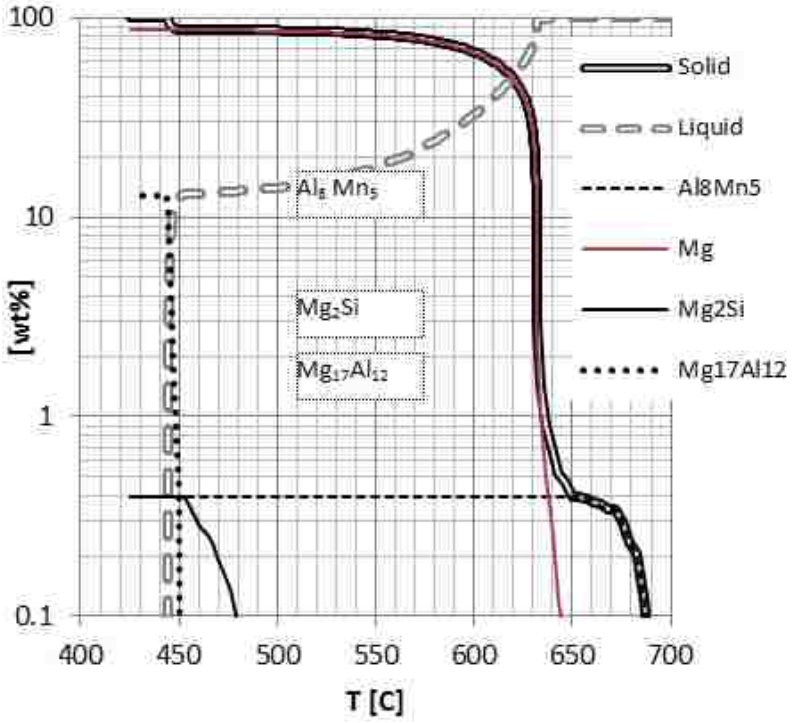

Figure 53 - AM60B phase evolution during solidification at 18°C/s to 14°C/s.

The solid forms as 0.3% of Al_8Mn_5 between 687°C and 650°C; 85% as αMg between 643°C and 450°C and finally as 12% of $Mg_{17}Al_{12}$-αMg eutectic between 450°C and 428°C.

Table 18 - Enthalpy of formation of phases from AM60B solidifying at 18°C/s.

	Alloy latent heat	**αMg**	**$Mg_{17}Al_{12}$-αMg eutectic**	**Al_8Mn_5**	**Mg_2Si**
ΔH_f [J/g]	**-289**	**-317**	**-79**	**-535**	**-605**
T_{start} [°C]	697	647	452	697	491
T_{max} [°C]	632	632	445	683	482
T_{end} [°C]	441	452	441	654	452

Table 18 summarizes the key cooling curve information from solidification of AM60B at 18°C/s. The information for this Table was generated through the integration of peaks in Figure 10 associated with individual phases. As expected the latent heat of solidification of the alloy is lower than that for pure Mg. Forming αMg in this alloy

yields -317 J/g as compared with -348 J/g for formation of the same phase from pure Mg melt. Formation of the eutectic yields relatively little heat, whereas the formation of Al_8Mn_5 and Mg_2Si are highly exothermic.

4.9.4 Solidification Path: Evolution of Melt Composition

Information illustrated in Figure 53 combined with the composition of the individual phases allow for the calculation of the residual liquid composition during the solidification event. Knowledge of such solidification path is key to understanding the phase formation during solidification. The solidification path is plotted as concentration of the individual alloying elements as a function of temperature in Figure 54.

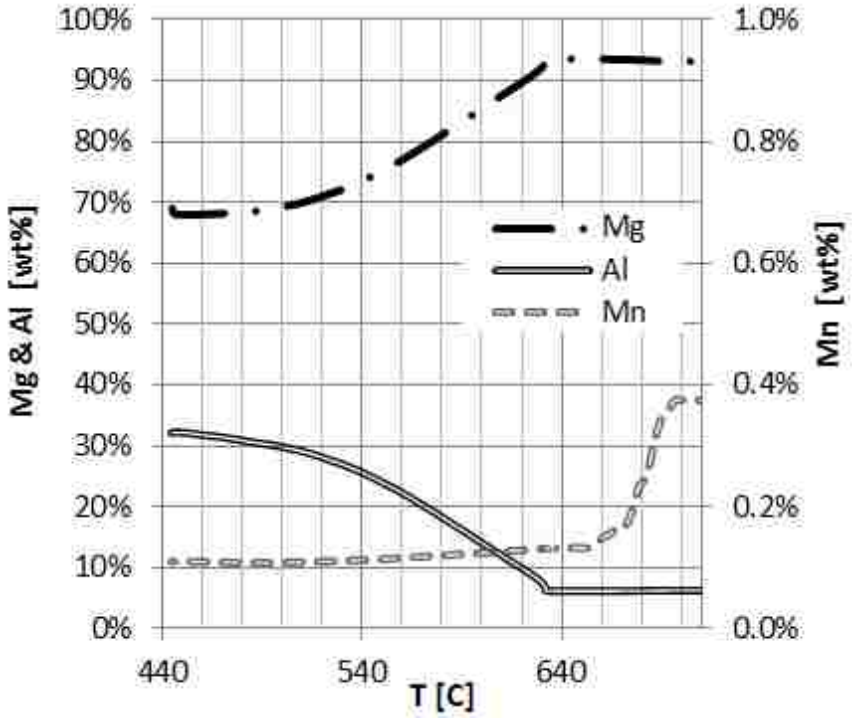

Figure 54 - AM60B composition variation during solidification at 18°C/s to 14°C/s.

At very rapid cooling rates interpretation of the cooling curves becomes more difficult. Total solidification time reduces to a few seconds. During that time there is the initial transient of introducing the coolant to the molten sample and setting up a stable boundary layer and heat transfer coefficient between the coolant and the sample. When

liquid coolant is used, it is common to observe vapor or air bubbles exiting the cooling tube. This suggests that an insulating gas film may form on the hot cooling tube surface and impede the cooling process. This can lead to irreproducible, apparent thermal peaks that have nothing to do with the enthalpy of alloy solidification. In this thesis, the reported cooling curve data was limited to ~25°C/s, which is a rate that was consistently reached using compressed gas coolant. This eliminates the possibility of insulating vapor film formation on the cooling tube surface.

Further, there is an implicit assumption in the analysis that the sample is isothermal. This is valid at slow cooling rates because of very high thermal conductivity of the metal sample. However, as cooling rates reach hundreds of degrees per second, the heat flux required to achieve such a rate also requires a temperature gradient in the sample. The effect of the gradient causes the apparent exotherm to start at a higher temperature than recorded by the centrally located thermocouple and continues to a lower temperature after solidification is complete at the thermocouple location. This effect is reproducible and was calibrated out for enthalpy measurements by performing the calibration measurements on pure Mg over the cooling rate range spanning the rates of interest for gas cooling. Extrapolation of these calibration values to more rapid liquid coolant rates was not successful. The temperature gradient in the sample spreads the exotherm over a range of temperatures. This can cause small and overlapping exotherms to be smeared out and lost in the baseline noise.

4.9.5 Corresponding AE44 Results

The AE44 cooling curves were quite different from those of the AM60B. The AE44 solidification range was very narrow and was characterized by a single exothermic peak in spite of microstructural and micro-chemical observations which identified three phases in the alloy microstructure. Figure 55, Figure 56 and Figure 57 show the corresponding graphs for the AE44 data.

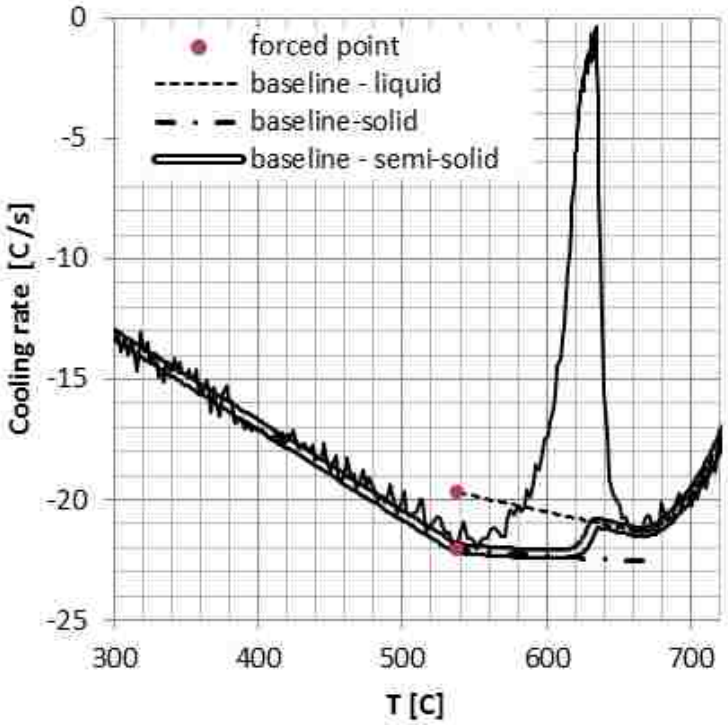

Figure 55 - Cooling curve of AE44 solidified at 22°C/s.

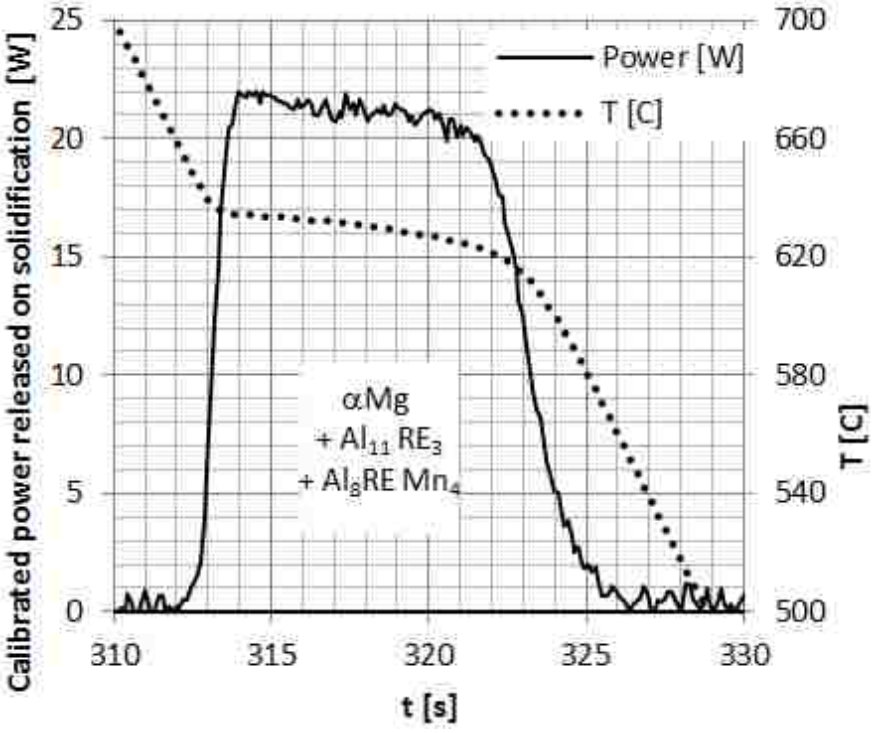

Figure 56 - Calibrated values of the power released during solidification of 5.7g AE44 sample at 22°C/s.

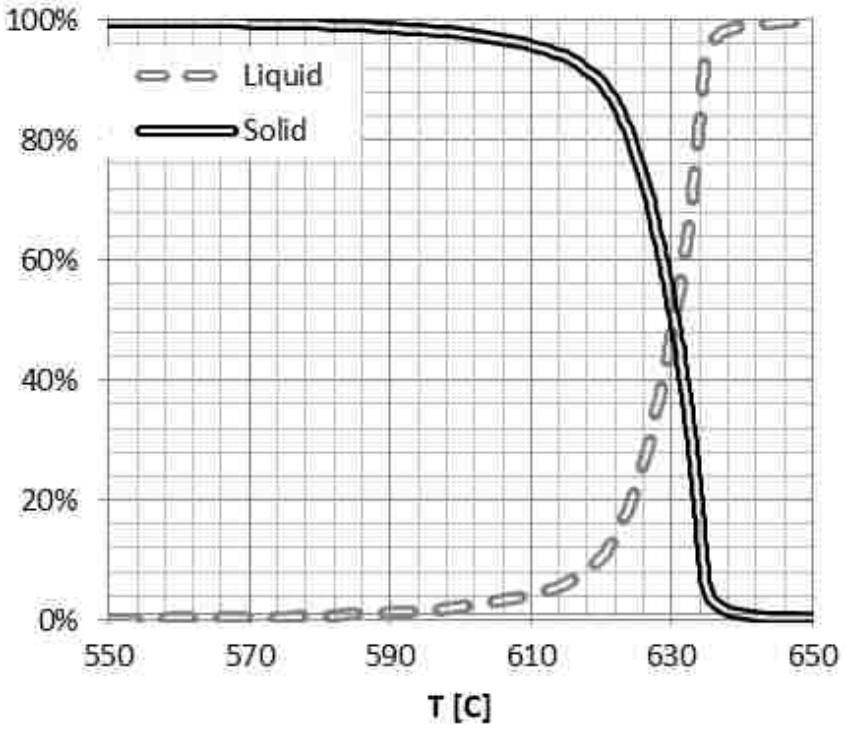

Figure 57 - AE44 solid formation and residual liquid during solidification at 22°C/s.

Attribution of energy to individual phases is not feasible based on this data. Latent heat of solidification of the AE44 alloy is the area under the power curve. It is -348J/g which is equal to pure Mg. This is significantly more exothermic than AM60B, implying that formation of the $Al_{11}RE_3$ intermetallics is highly exothermic. Concurrent work into analysis of the AE44 alloy for a future paper should reveal more detailed phase analysis.

Chapter 5 Summary and Conclusions

The UMSA Technology Platform has been modified to allow for advanced rapid cooling experiments. These modifications allow for experiments with instantaneous cooling rates of hundreds of degrees per second and tracking during the liquid, semi-solid and solid regions. Samples tested using the modified system have yielded impressive microstructures. Though further refinements to the system need to be implemented to obtain consistent and quality thermal data at the highest rates (there are limits to heat transfer control), excellent data has been obtained for samples cooled with compressed gas at intermediate cooling rates.

Combining the thermal data with microstructural and micro-chemical results yields a wealth of information on the phases formed, sequence of events, the enthalpies of formation of component phases and evolution of residual melt composition during solidification. Reliable and reproducible cooling curves for magnesium alloys cooled at intermediate rates (compressed Ar cooling) have sufficient detail to resolve the component phase contribution. The same resolution has not yet been applied to the highest rates, due to the aforementioned limitations (as well as gradual changes in the type and quantity of phases formed) however future work will focus on improving control of the highest cooling rates so that reliable, quantifiable results can be obtained.

The key results of this research are:

- A modified UMSA platform, which has demonstrably reached instantaneous cooling rates of 520°C/s. These rates are rarely seen in literature for macro-sized test samples for quenching tests through the entire semisolid region. This platform will be used in the future to build upon the presented results.
- An extremely refined silicon structure in hypereutectic silicon. High levels of strontium modification as well as high cooling rates are both novel processing conditions in this field. The combination of the two has produced a microstructure whose bulk is nearly devoid of primary or eutectic silicon, leaving only very small, globular silicon particles. This is an extremely desirable microstructure and, for certain part geometries, the process may be adapted to cast automotive components

such as cylinder liners. Future tests must however show that the microstructure can be sustained under the rigours of normal use conditions.

- A new method of calculating a semisolid baseline for non-equilibrium cooling. Most fraction solid data available in the literature is available only for very slow cooling. Combining the thermal data from elevated cooling rates with microchemical data from SEM/EDS analysis has allowed for the formulation of a baseline that is extensible to peak cooling rates of 20°C/s and produces accurate and repeatable fraction solid data. This information would be useful for casting control for parts cooled at elevated rates as well as casting simulations. Though at present the technique has only been applied to Mg-based alloys, subsequent investigations have shown that it can also be applied to Al-based alloys. Future work can extend the same techniques to even higher rates or other alloys.

Chapter 6 Recommendations for Future Work

The research presented shows results from a combination of new technologies, new alloys and new computational techniques, all of which deserve to be investigated and developed further. Future work may look at some of the following areas.

Developing an optimized solution treatment for Al20SiSr

The Al20SiSr tests have shown good progress in reducing silicon particle size with a combination of Sr and rapid cooling from above the liquidus. It would be useful to optimize the featherlike dendritic structure using a solution treatment. This would fragment dendrites and spheroidize particles producing a highly refined form of silicon that is unlike either the primary or eutectic crystal morphology.

Developing more controlled quenching techniques

Thermal data from air and compressed Ar cooling yielded clear and consistent data. Rapid cooling (water and/or glycol) thermal data has more variability because of a variable heat transfer coefficient, h, due to the water vapour blanket formation. A super-critical fluid cooling system would get rid of the vapour blanket formation and stabilize the dT/dt/T baseline trace [79].

Table 19 - Liquid-vapour critical temperature and pressure of possible quenchant alternatives [80].

Substance	Critical temperature	Critical pressure (absolute)
Helium	-267.96 °C (5.19 K)	2.24 atm (227 kPa)
Argon	-122.4 °C (150.8 K)	48.1 atm (4,870 kPa)
Nitrogen	-146.9 °C (126.3 K)	33.5 atm (3,390 kPa)
CO_2	31.04 °C (304.19 K)	72.8 atm (7,380 kPa)
Water	373.946 °C (647.096 K)	217.7 atm (22,060 kPa)

Water would be too difficult to pressurize to 218 atm. However, pressurizing helium to 2.24 atm may be possible and, with its high thermal conductivity, could be used with the same thin, stainless steel tubes which are currently used in heat

extraction. Implementing this would require a rigid closed-loop pressurized system with a circulation pump, a fluid-to-water heat exchanger and a vacuum pump to evacuate the sample tube before filling it with He (to prevent He contamination) [79].

Developing, applying and publishing results of new baseline methodologies

The baseline methodology applied to the magnesium alloys in this study is easily extensible to other alloys, such as the Al20SiSr and A356 alloys. Data already exists for comparable compressed Ar cooling rates. With additional calibration tests as well as SEM work, this data could easily be the focus of another paper.

Another study could integrate thermochemical data in the literature with the thermal analysis results and microchemical analytical results from SEM-EDS analysis to extract the activity, 'a', and activity coefficient data for the components of the solidifying liquid and the phases that are forming during the process. "Dynamic" phase diagrams could be constructed by plotting the phase and liquid compositions on the temperature-composition axes and extracting the shape of the liquidus curves/surfaces from the f_s information. One could also calculate the entropy contributions and the free energy (G-X) diagrams for the individual phases, and from these extract the activity and activity coefficient data, as well as other additional thermodynamic parameters. The chemical activities are key for prediction of material corrosion resistance and thermal phase stability during subsequent service [79, 81].

Development of wear-resistant and durable hypereutectic AlSi alloys and technology

The work on the hypereutectic alloy should be continued and may lead to patentable intellectual property. Though the quenching techniques may be difficult to implement in many castings, they may find great use in castings of certain geometries, such as cylinder liners.

References

1. *Properties and Selection: Nonferrous Alloys and Special-Purpose Materials*. ASM Handbook. Vol. 2. 1990, ASM International.
2. Murray, J. L. and A. J. McAlister, *The Al-Si (Aluminum-Silicon) Casting System.* Bulletin of Alloy Phase Diagrams, 1984. **5**(1): p. 74-84.
3. Kierkus, W. T., M. B. Djurdjevic, and J. H. Sokolowski, *Analysis of the Solidification Path of the 3XX Family of Aluminum Alloys*. 2002, Industrial Research Chair in Light Metals Casting Technology.
4. Bäckerud, L., G. Chai, and J. Tamminen, *Foundry Alloys*. Solidification Characteristics of Aluminum Alloys. Vol. 2. 1990, Stockholm: AFS/Skanaluminium.
5. Kasprzak, W., J. Sokolowski, H. Yamagata, M. Aniolek, and H. Kurita, *Energy Efficient Heat Treatment for Linerless Hypereutectic Al-Si Engine Blocks Made Using Vacuum HPDC Process.* Journal of Materials Engineering and Performance, 2010: p. 1-13.
6. Hatch, J. E., ed. *Aluminum: Properties and Physical Metallurgy*. 1984, ASM International. 424.
7. Li, W., S. Cui, J. Han, and C. Xu, *Effect of Silicon on the Casting Properties of Al-5.0% Cu Alloy.* Rare Metals, 2006. **25**(6, Supplement 2): p. 133-135.
8. Moustafa, M. A., F. H. Samuel, H. W. Doty, and S. Valtierra, *Effect of Mg and Cu Additions on the Microstructural Characteristics and Tensile Properties of Sr-Modified Al-Si Eutectics Alloys.* International Journal of Cast Metals Research, 2002. **14**: p. 235-253.
9. Mackenzie, D. S. and G. E. Totten, *Handbook of Aluminum: Vol. 1: Physical Metallurgy and Processes*. Vol. 1. 2003: CRC Press. 1310.
10. Maniara, R., L. A. Dobrzański, M. Krupiński, and J. H. Sokołowski, *The effect of copper concentration on the microstructure of Al-Si-Cu alloys.* Archives of Foundry Engineering, 2007. **7**(2): p. 119-124.
11. Lee, P. D. and J. D. Hunt, *Hydrogen porosity in directional solidified aluminium-copper alloys:in situ observation.* Acta Materialia, 1997. **45**(10): p. 4155-4169.
12. Zhang, Z., X. Bian, and X. Liu, *Effect of Strontium Addition on Hydrogen Content and Porosity Shape of Al-Si Alloys.* International Journal of Cast Metals Research, 2001. **14**: p. 31-35.
13. Savas, Ö. and R. Kayikci, *Application of Taguchi's methods to investigate some factors affecting microporosity formation in A360 aluminium alloy casting.* Materials & Design, 2007. **28**(7): p. 2224-2228.
14. Key to Metals AG. *Modification and Refinement of Aluminum-Silicon Alloys*. [cited 2012 April 11, 2012]; Available from: http://www.keytometals.com/page.aspx?ID=CheckArticle&site=ktn&NM=85.
15. Byczynski, G. E. and D. A. Cusinato, *The Effects of Strontium and Grain Refiner Additions on the Fatigue and Tensile Properties of Industrial Al-Si-Cu-Mg Alloy Castings Produced Using the Ford Motor Company - Cosworth Precision Sand Process.* International Journal of Cast Metals Research, 2002. **14**: p. 315-324.

16. Emadi, D., L. V. Whiting, V. Y. Gertsman, M. Sahoo, R. MacKay, and G. E. Byczynski, *Effect of Tin on the Mechanical Properties of Aluminum 319 Alloy.* AFS Transactions, 2006. **114**: p. 263-272.
17. Kiełbus, A., *Microstructure of AE44 magnesium alloy before and after hot-chamber die casting.* Journal of Achievements in Materials and Manufacturing Engineering, 2007. **20**(1-2): p. 459-462.
18. Rzychoń, T., A. Kiełbus, J. Cwajna, and J. Mizera, *Microstructural stability and creep properties of die casting Mg–4Al–4RE magnesium alloy.* Materials Characterization, 2009. **60**(10): p. 1107-1113.
19. Weiler, J. P., J. T. Wood, R. J. Klassen, R. Berkmortel, and G. Wang, *Variability of skin thickness in an AM60B magnesium alloy die-casting.* Materials Science and Engineering: A, 2006. **419**(1–2): p. 297-305.
20. Huang, W., B. Hou, Y. Pang, and Z. Zhou, *Fretting wear behavior of AZ91D and AM60B magnesium alloys.* Wear, 2006. **260**(11–12): p. 1173-1178.
21. Jarfors, A. E. W., K. U. Kainer, M.-J. Tan, and J. Yong, *Recent Developments in the Manufacturing of Components from Aluminium-, Magnesium- and Titanium-Based Alloys.* COSMOS, 2009. **5**(1): p. 23-58.
22. Sokolowski, J. H., *Novel Opportunities for Disruptive Analysis, R & D and QC of Alloys, Melts, Cast Components and Heat Treatment Processes based on Physical Simulations*. 2009.
23. Upadhya, K. G., D. M. Stefanescu, K. Lieu, and D. P. Yeager, *Computer-Aided Cooling Curve Analysis: Principles and Applications in Metal Casting.* AFS Transactions, 1989. **97**: p. 61-66.
24. Ananthanarayanan, L., F. H. Samuel, and J. Gruzleski, *The Thermal Analysis Studies on the Effect of Cooling Rate on the Microstructure of the 319 Aluminum Alloy.* AFS Transactions, 1992. **141**(383-391).
25. Arnberg, L., L. Bäckerud, and G. Chai, *Solidification Characteristics of Aluminum Alloys, Volume 3: Dendrite Coherency*. Vol. 3. 1996, Des Plaines, Illinois, USA: American Foundrymen's Society, Inc.
26. Chai, G., *Dendrite Coherency During Equiaxed Solidification in Aluminum Alloys*, in *Department of Structual Chemistry*. 1994, Stockholm University: Stockholm.
27. Chen, Y. F., S. H. Jong, and W. S. Hwang, *Effects of Cooling Rate on Latent Heat Released Mode of Near Pure Aluminium and Aluminium-Silicon Alloys.* Materials Science and Technology, 1996. **12**(7): p. 539-544.
28. Figueredo, A. M., Y. Sumartha, and M. C. Flemings, *Measurement and calculation of solid fraction in quenched semi-solid melts of rheocast aluminum alloy A357*, in *Light Metals 1998*, B. Welch, Editor. 1998, The Minerals, Metals and Materials Society. p. 1103-1106.
29. Gowri, S., *Comparison of thermal analysis parameters of 356 and 359 alloys.* AFS Transactions, 1994. **102**: p. 503-508.
30. Kang, H. G., H. Miyahara, and K. Ogi. *Influence of cooling rate and additions of Sr and Ti-B on solidification structures of AC4B type alloy*. in *Asian Foundry Congress*. 1995. Kyongju, Korea: The Korean Foundrymen's Society.

31. Tamminen, J., *Thermal analysis for investigation of solidification mechanisms in metals and alloys*, in *Department of Structural Chemistry* 1988, University of Stockholm: Stockholm.
32. MacKay, R., M. Djurdjevic, and J. H. Sokolowski, *Effect of Cooling Rate on Fraction Solid of Metallurgical Reactions in 319 Alloy.* AFS Transactions, 2000. **25**: p. 521-529.
33. MacKay, R., M. Djurdjevic, J. H. Sokolowski, and W. Evans, *Using the Method of a In-situ Thermal Analysis Array in a Cast Section to Assess Riser Feeding Efficiency*, in *131st TMS Annual Meeting*. 2002: Seattle, Washington, USA.
34. Chen, J. H. and H. L. Tasi, *Comparison of different modes of latent heat release for modeling casting solidification.* AFS Transactions, 1990. **133**: p. 539-546.
35. Flemings, M., *Solidification processing.* Metallurgical and Materials Transactions B, 1974. **5**(10): p. 2121-2134.
36. Huang, H., V. K. Suri, J. L. Hill, and J. T. Berry, *Heat Source/Sink Algorithm for Modeling Phase Changes During Solidification in Castings and Water Evaporation in Green Sand Molds.* AFS Transactions, 1991. **54**: p. 685-689.
37. Jeng, S. and S. Chai, *Determination of the Solidification Characteristics of the A356.2 Aluminum Alloy.* Materials Science Forum, 1996. **217-222**: p. 283-288.
38. Kanetkar, C. S. and D. M. Stefanescu, *Macro-micro modeling of solidification of hypoeutectic and eutectic Al-Si alloys.* AFS Transactions, 1988. **60**: p. 591-598.
39. Kiuchi, M. and S. Sugiyama, *A New Method to Detect Solid Fractions of Mushy/Semi-Solid Metals and Alloys.* CIRP Annals - Manufacturing Technology, 1994. **43**(1): p. 271-274.
40. Kurz, W. and D. J. Fisher, *Fundamentals of Solidification*. 1986: Trans Tech Publications.
41. Ohta, S. and K. Asai, *The Behavior of Temperature Decreasing and Fraction Solid Increasing in Solid-Liquid Coexisting Zone in Solidification Process of Aluminum Alloy Weld Metal.* Transactions of the Japan Welding Society, 1993. **24**(2): p. 131-139.
42. Rappaz, M., *Modelling of microstructure formation in solidification processes.* International Materials Reviews, 1989. **34**(1): p. 93-124.
43. Saunders, N., *Phase Diagram Calculations for Commercial Al-Alloys.* Materials Science Forum, 1996. **217-222**: p. 667-672.
44. Stefanescu, D., G. Upadhya, and D. Bandyopadhyay, *Heat transfer-solidification kinetics modeling of solidification of castings.* Metallurgical and Materials Transactions A, 1990. **21**(3): p. 997-1005.
45. Tzimas, E. and A. Zavaliangos, *Evaluation of volume fraction of solid in alloys formed by semisolid processing.* Journal of Materials Science, 2000. **35**(21): p. 5319-5330.
46. Wannasin, J., R. Canyook, R. Burapa, L. Sikong, and M. C. Flemings, *Evaluation of solid fraction in a rheocast aluminum die casting alloy by a rapid quenching method.* Scripta Materialia, 2008. **59**(10): p. 1091-1094.
47. Saunders, N., Z. Guo, A. P. Miodownik, and J.-P. Schillé. *Modelling the Material Properties and Behaviour of Ni- and NiFe-Based Superalloys*. in *Sixth International Symposium on Superalloys 718, 625, 706 and Derivatives*. 2005. Pittsburgh, PA: TMS.

48. Sołek, K. P., R. M. Kuziak, and M. Karbowniczek, *The application of thermodynamic calculations for the semi-solid processing design.* Archives of Metallurgy and Materials, 2006. **52**(1): p. 85-32.
49. Mackay, R. and J. Sokolowski, *Experimental Observations of Dendrite Coarsening and Al-Si Eutectic Growth in Progressively Quenched Structures of Al-Si-Cu Casting Alloys.* International Journal of Metalcasting, 2008. **Spring 2008**: p. 57-80.
50. Djurdjevic, M. B., W. T. Kierkus, G. E. Byczynski, T. J. Stockwell, and J. H. Sokolowski, *Modeling of Fraction Solid For The 319 Aluminum Alloy.* AFS Transactions, 1999. **14**: p. 173-179.
51. Fras, E., W. Kapturkiewicz, A. Burbielko, and H. F. Lopez, *A new concept in thermal analysis of castings.* AFS Transactions, 1993. **101**: p. 505-511.
52. Barlow, J. O. and D. M. Stefanescu, *Computer-Aided Cooling Curve Analysis Revisited.* AFS Transactions, 1997. **105**: p. 349-354.
53. Kierkus, W. T. and J. H. Sokolowski, *Recent Advances in Cooling Curve Analysis: A New Method of Determining the 'Base Line' Equation.* AFS Transactions, 1999. **66**: p. 161-167.
54. Riesen, R., *Choosing the Right Baseline.* UserCom, 2007. **25**.
55. Emadi, D., L. Whiting, M. Djurdjevic, W. T. Kierkus, and J. H. Sokolowski, *Comparison of newtonian and fourier thermal analysis techniques for calculation of latent heat and solid fraction of aluminum alloys.* Metalurgija, 2004: p. 91-106.
56. Stefanescu, D. M., *Solidification of Flake, Compacted, Vernicular and Spheroidal Graphite Cast Irons as Revealed by Thermal Analysis and Directional Solidification Experiments.* Material Research Society Symposium Proceedings, 1985. **34**.
57. Robles-Hernandez, F. C., M. B. Djurdjevic, W. T. Kierkus, and J. H. Sokolowski, *Calculation of the liquidus temperature for hypo and hypereutectic aluminum silicon alloys.* Materials Science and Engineering A, 2005. **396**(1-2): p. 271-276.
58. Djurdjevic, M. B., A. Mitrasinovic, J. H. Sokolowski, and G. Byczynski, *Development Of The Silicon Equivalent (SiEQ) Algorithm And Its Application For Calculation Of The Characteristic Temperatures Of Solidification Multi-Component 3XX Series Of Aluminum Alloys.*
59. ASM International, ed. *ASM Handbook, Volume 4, Heat Treating*. ed. H. Committee. 1991.
60. Fuoco, R., H. Goldenstein, and J. E. Gruzleski, *Evaluation of Effect of Modification-Induced Eutectic Undercooling on Microporosity Formation in 356 Al Alloy.* AFS Transactions, 1994. **102**: p. 297-306.
61. Bates, C. E., G. E. Totten, and N. A. Clinton, *Handbook of Quenchants and Quenching Technology*. 1993, Materials Park, OH: ASM International.
62. Fontecchio, M., *Quench Probe and Quench Factor Analysis of Aluminum Alloys*, in *Materials Science and Engineering*. 2002, Worcester Polytechnic Institute: Worcester, MA. p. 102.
63. Totten, G. E. and D. S. Mackenzie, *Aluminum Quenching Technology: A Review.* Materials Science Forum, 2000. **331-337**: p. 589-594.

64. Zhang, D. and L. Zheng, *The quench sensitivity of cast Al-7 wt pct Si-0.4 wt pct Mg alloy*. Metallurgical and Materials Transactions A, 1996. **27**(12): p. 3983-3991.
65. Livak, R. J., *The Effects of Copper and Chromium on the Aging Response of Dilute Al-Mg-Si Alloys*. Metallurgical Transactions A., Physical Metallurgy and Materials Science, 1982. **13**(7): p. 1318-1321.
66. Fontecchio, M., M. Maniruzzaman, and R. D. S. Jr., *Quench Factor Analysis and Heat Transfer Coefficient Calculations for 6061 Aluminum Alloy Probes Quenched in Distilled Water*, in *Mechanical Engineering Department*, Worcester Polytechnic Institute (WPI): Worcester, MA.
67. Rong, Y., R. D. Sisson Jr., J. E. Morral, and H. D. Brody, *An Energy Saving Model for the Heat Treatment of Castings*. 2006, Worcester Polytechnic Institute: Worcester, MA.
68. Yamagata, H., W. Kasprzak, M. Aniolek, H. Kurita, and J. H. Sokolowski, *The effect of average cooling rates on the microstructure of the Al-20% Si high pressure die casting alloy used for monolithic cylinder blocks*. Journal of Materials Processing Technology, 2008. **203**(1-3): p. 333-341.
69. Yamagata, H., H. Kurita, M. Aniolek, W. Kasprzak, and J. H. Sokolowski, *Thermal and metallographic characteristics of the Al-20% Si high-pressure die-casting alloy for monolithic cylinder blocks*. Journal of Materials Processing Technology, 2008. **199**(1-3): p. 84-90.
70. Omega. *Introduction to Thermocouples*. [cited 2012 March 3]; Available from: http://www.omega.com/prodinfo/ThermocoupleSensor.html.
71. RDC Control. *Thermocouples*. [cited 2012 May 16]; Available from: http://www.rdccontrol.com/en/thermocouple/thermocouple-junctions-and-response-time.html.
72. Rudnev, V., *Handbook of Induction Heating*. 2003: Marcel Dekker.
73. Marr, M. A., J. S. Wallace, S. Chandra, L. Pershin, and J. Mostaghimi, *A fast response thermocouple for internal combustion engine surface temperature measurements*. Experimental Thermal and Fluid Science, 2010. **34**(2): p. 183-189.
74. The Engineering ToolBox. *Thermal Conductivity of some common Materials and Gases*. [cited 2012 March 4]; Available from: http://www.engineeringtoolbox.com/thermal-conductivity-d_429.html.
75. Noranzyk, A., *Thermal Conductivity Measurements of Graphite Samples*. 2009, Colorado School of Mines: Golden, CO.
76. Maniruzzaman, M., J. C. Chaves, C. McGee, S. Ma, and R. D. S. Jr., *CHTE Quench Probe System – A New Quenchant Characterization System*, in *International Conference on Frontiers of Design and Manufacturing*. 2002: Dalian, China.
77. Kasprzak, W., M. Sahoo, J. Sokolowski, H. Yamagata, and H. Kurita, *The Effect of the Melt Temperature and the Cooling Rate on the Microstructure of the Al-20% Si Alloy Used for Monolithic Engine Blocks*. International Journal of Metalcasting, 2009. **Summer 2009**.
78. Mirković, D. and R. Schmid-Fetzer, *Solidification Curves for Commercial Mg Alloys Determined from Differential Scanning Calorimetry with Improved Heat-*

Transfer Modeling. Metallurgical and Materials Transactions A, 2007. **38**(10): p. 2575-2592.
79. Gesing, A. J., *Personal Communication*, P. Marchwica, Editor. 2012: Windsor.
80. Wikipedia. *Critical point (thermodynamics)*. 2012 [cited 2012 April 4]; Available from: http://en.wikipedia.org/wiki/Critical_point_%28thermodynamics%29.
81. Gesing, A. J., J. H. Sokolowski, C. Blawert, and N. Reade, *Solidification Behavior of Recyclable Mg Alloys - AZ91D and AZC1231 (Seminar)*. 2012.

Vita Auctoris

NAME	Paul C. Marchwica
PLACE OF BIRTH	Hamilton, Ontario
YEAR OF BIRTH	1986
EDUCATION	Hon. Vincent Massey Secondary School, Windsor, Ontario 2000-2004
	University of Waterloo, Waterloo, Ontario 2004-2009, BASc Systems Design Engineering
	University of Windsor, Windsor, Ontario 2010-2012, MASc Mechanical Engineering